POLITECNICO DI TORINO

Master's Degree in Aerospace Engineering

Politecnico di Torino

TU Delft

Evaluation of Navigation Solutions from GNSS Receivers for Orbital Positioning and Prediction

Supervisors

Prof. Fabrizio STESINA

Prof. Stefano SPERETTA

Rens VAN DER ZWAARD

Candidate

Monica Antonella CORTIGIANO

s315910

A.A. 2025/26

Acknowledgements

A sincere thanks goes to my supervisors, who guided me throughout the development of this work. I would like to thank Professor Fabrizio Stesina for trusting me and giving me the opportunity to carry out this research in Delft, and for his constant support and interest throughout its development.
I would also like to thank Stefano Speretta and Rens van der Zwaard, who one have been involved in the development and progress of this thesis from day one, with the same curiosity and enthusiasm as I had. I had the privilege of learning a lot through our constant exchange of ideas, a valuable source of inspiration that I will carry with me in my future.
Throughout my academic life, I have been lucky enough to meet mentors who inspired me not only in the subject but also in developing a passion for the work and teaching. I am truly grateful to have had you as my supervisors for this final step of my academic journey.

Abstract

In recent years, space activity has increased at an unique rate, leading to a rapidly growing number of satellites orbiting around the Earth, particularly in Low Earth Orbit (LEO). This growth has significantly increased orbital congestion and the related risk of collisions and space debris generation. In the last few years, more satellites have been launched than in the previous six decades of space exploration. To address this issue, new guidelines are being discussed: European Space Agency (ESA) has proposed standards and initiatives, such as the "Zero Debris" approach, aimed at reducing the creation of new debris in Earth orbits by 2030 [1]. As a result, maintaining space safety and space access has become a critical challenge for current and future missions. This crowded orbital environment calls for advanced positioning and prediction capabilities. Reliable knowledge of the satellite's state and its future evolution is essential not only for reducing space debris formation, but also for autonomous navigation, formation flying, collision avoidance, and overall mission success.
Within this context, the advent of CubeSats in the early 21st century has increased access to space by offering a cost-effective, fast, and reliable alternative to conventional large satellites. The use of Commercial Off-The-Shelf (COTS) components and the standardization of the subsystems have made this possible. This has widen the scenario for space missions enabling more frequent launches, hands-on science experiments for both students. However, the rapid growth in the number of CubeSats has contributed to the already problematic orbital congestion. In addition to this, Precise Orbit Determination (POD) becomes particularly challenging in the context of CubeSats, which are limited by their small size, mass, available on-board resources and often lack of any propulsion system. One approach is to calculate the position directly using Global Navigation Satellite System (GNSS) signals. Therefore, to achieve reliable POD on small platforms, the integration of low-cost GNSS receivers and antennas has to be adapted and studied to the constraints of CubeSats.

This thesis aims to study, compute and assess the reliability and feasibility of Orbit Determination (OD) and Orbit Prediction (OP) based on GNSS measurements. The objective is to demonstrate it is possible to use a GNSS system to retrieve measurements, upon which OD and OP can be performed. The study evaluates single- and dual-frequency GNSS receivers to determine the impact of measurement precision on the accuracy of OD and OP. By comparing the performance of each receiver configuration, the study identifies the setup that minimises error and improves the reliability of space operations. From the Determined and Propagated states , Orbital Ephemeris Messages (OEM)s can be directly generated. These orbital data products are compared against conventional radar-generated and GNSS-based Two Line Elements (TLE)s. This comparison provides a comprehensive analysis of GNSS-based Orbit Determination and Prediction as a reliable alternative to standard space operations methods and orbital data formats.

This research is particularly significant in the context of the Delfi-Twin mission, which aims to launch two identical picosatellites in 2027, to demonstrate autonomous formation flying and collision avoidance solely using differential drag.

Table of Contents

List of Figures

List of Tables

Acronyms

BIH Bureau International de l'Heure.

COTS Commercial Off-The-Shelf.

ECEF Earth Centered Earth Fixed.

ECI Earth Centered Inertial.

ESA European Space Agency.

GDOP Geometrical Diluition of Precision.

GLONASS Global Navigation Satellite System.

GNSS Global Navigation Satellite System.

GPS Global Positioning System.

LEO Low Earth Orbit.

LLA Latitude, Longitude, Altitude.

LNA Low Noise Amplifier.

NMEA National Marine Electronics Association.

OD Orbit Determination.

OEM Orbital Ephemeris Messages.

OP Orbit Prediction.

POD Precise Orbit Determination.

PQ PocketQubes.

PVT Position, Velocity, and Time.

RF Radio Frequency.

RMSE Root Mean Square Error.

RSW Radial, Along Track, Cross Track.

RTK Real Time Kinematics.

SBF Septentrio Binary Format.

SDR Software Defined Radio.

SGP-4 Simplified General Perturbations 4.

TEC Total Electron Content.

TEME True Equator Mean Equinox.

TLE Two Line Elements.

TUDAT Technical University of Delft Astrodynamics Toolbox.

USRP Universal Software Radio Peripheral.

WGS84 World Geodetic System 1984.

Chapter 1

Introduction

1.1 Thesis Proposal

This thesis studies, computes and assesses the reliability and feasibility of navigation solutions derived from GNSS receiver measurements. The objective is to demonstrate that GNSS data can be used to perform in-orbit determination and subsequent trajectory prediction, in particular validating GNSS-based Orbit Determination as an alternative to traditional methods in the context of small satellites. The OEMs generated from the GNSS-based orbit solutions, indeed, are compared with conventional TLEs to evaluate their performance and suitability as possible orbital data products.
This chapter begins with an overview of CubeSats and an introduction to the Delfi-TwinSat mission. It also discusses Orbit Determination methods, defines the research objectives and describes the adopted workflows. A brief summary of the subsequent chapters is also included.

1.2 Cubesats: Overview and applications

Initially proposed in 1999 by California Polytechnic State University and Stanford University, CubeSats have gradually changed the perception of satellite missions and access to space by promoting a new modular approach to satellite design and integration.
CubeSats are a class of nanosatellites that use a standard size and form factor [2]. The standard CubeSat unit has a volume of 1 dm^3 and a weight of up to

3 kg. Single units can be combined to form bigger artifacts, such as 2U, 3U, 6U and so forth. CubeSats must follow the standards defined by the CubeSat Design Specification [3].
The idea behind the development of CubeSats was educational, giving students hands-on experience of working on a space project. Due to this motivation, it was mandatory that development, launching, and operation costs were kept to the lowest possible, which led to project standardization. To achieve this, the use of COTS components was mandatory. Although this has several advantages in terms of development time, cost, and overall project complexity, it also poses significant technical challenges.
Their advantages have led CubeSats to be used in an increasing number of missions, covering technology demonstration, scientific experiments, Earth observation, and commercial operations. Today, CubeSats are a competitive solution for space applications as they offer an optimal trade-off between time, cost, mission lifetime and ease of replacement [4]. These advantages have attracted the attention of the wider space sector, extending the use of CubeSats in private companies and government institutions worldwide, increasing the amount of nanosatellites in LEO[5].
Following this innovative concept, PocketQubes (PQ) were developed 10 years later. These platforms are based on a cubic-shaped form of 50x50x50 mm per unit (1P), therefore with each side one-half smaller than a 1U CubeSat.

1.3 Space Debris Mitigation

The growing number of nanosatellites, along with other satellites, is making LEO increasingly congested, posing a significant threat to the Earth and the future of space exploration. Indeed, since the beginning of space exploration, the amount of space debris has consistently exceeded the number of operational satellites.
Space debris is defined as all artificial objects including fragments and elements thereof, in Earth orbit or re-entering the atmosphere, that are non-functional [6]. Collisions between these objects have already occurred and continue to cause serious threat, generating debris fragments. Consequently, there is an increasing demand for techniques that can accurately calculate and predict the position of satellites in orbit.
CubeSats, in particular, typically lack of propulsion systems and are therefore non-manoeuvrable, making them a potential source of orbital debris. Moreover,

their small size presents challenges for POD, increasing the need for effective collision avoidance strategies.
To address these challenges, accurate and reliable OD becomes essential, both for CubeSats and PQ. Therefore, POD plays a key role in satellite tracking and control.

1.4 The Delfi Program

In the context of CubeSat application, the Delfi Space Programme is a university project based at TU Delft that focuses on the design and development of nanosatellites. Founded in 2004, its main mission objective is to provide students optimal preparation for careers in space industry, improving their technical preparation and team skills. It also aims to test and demonstrate the feasibility of space technologies, and to improve the small satellites bus platforms targeted for novel future applications. These objectives have been pursued in past and ongoing missions developed by the Delfi Programme.

1.4.1 Delfi-TwinSats

The Delfi-TwinSats project is a major ongoing initiative at TU Delft involving two satellites based on the Delfi-PQ design. The two satellites will be launched in docked configuration to limit the formation dispersion in rideshare launches. The purpose of the project is to demonstrate autonomous formation flying and collision avoidance using solely differential drag.
Each picosatellite will be equipped with a GNSS receiver for in-space POD, and deployable appendages to control drag and increase the available solar panels. Moreover, g round radar, optical and laser tracking of the satellites will be carried out for verification and validation. Notably, the TwinSats lack of traditional propulsion systems. Instead, orbital manoeuvres are planned through aerodynamic drag modulation, achieved by deploying the appendages. In order to achieve these objectives, it is essential to accurately determine the position, both to reduce uncertainty and to predict the future picosatellite's state, as well as to enable efficient orbital manoeuvres. The purpose of this thesis is focused on performing on-board OD and OP using a commercial GNSS receiver.

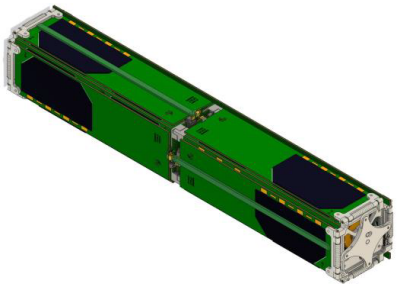

Figure 1.1: Delfi-Twin mission - Stowed configuration

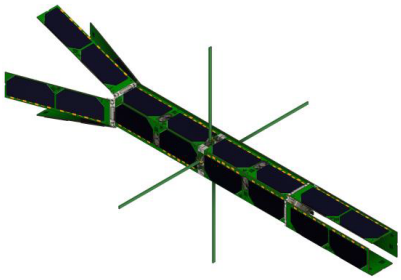

Figure 1.2: Delfi-Twin mission - Before and after the antenna and drag control appendages are deployed

1.5 Orbit Determination Methods

Orbit Determination is a key issue in astrodynamics and space mission design. It is the process of estimating the orbit of a spacecraft based on observations. It involves estimating the position, velocity and orbital parameters of an orbiting object over time.
Accurate OD is crucial for a wide range of space applications: autonomous navigation, collision avoidance and orbit prediction are those of our interest. Observation data can be obtained from a variety of sources, including ground-based sensors, on-board sensors and space-based observations.

1.5.1 Ground-Based Sensors

Ground-Based Sensors are fixed on the Earth's surface. It is not possible to have enough ground-based detection sensors to achieve full spatial coverage around the Earth. This limitation is primarily due to the high costs associated with manufacturing, installation and maintenance of such systems. Furthermore, geographical and climatic constraints can make deployment in certain regions difficult.
Nonetheless, ground-based sensors continue to play a significant role in both terrestrial and space applications. In fact, ground-based tracking is still one of the main ways of determining the orbit and position of satellites after launch, particularly in the case of CubeSats, mainly because of their limited on-board navigation capabilities [7].
Among ground based techniques, range and range-rate (Doppler), angular position, and laser ranging for satellites can be mentioned. However, the Two-

Line Element (TLE) set is the most widely used technique. For the purposes of this thesis, it is useful to examine the TLE format in detail.

Two-Line Elements is a standardised format used to describe the orbit of a satellite. They consist of a set of data that encodes a list of the orbital elements of an Earth-orbiting object at a given epoch. TLE data are the most extensive publicly available catalog of space objects and are published by the US Strategic Command (USSTRATCOM) on the Space Track website [8]. They are widely used for various space related applications due to their extensive coverage and accessibility. TLEs include the mean states determined by fitting observations to the dynamics provided by Simplified General Perturbations 4 (SGP-4), and they can only be used in conjunction with SGP-4.
TLE data are usually generated based on observations collected from ground-based tracking stations, radar systems, or other tracking methods. Due to their wide coverage and accessibility, TLEs are widely used in various space-related applications, including CubeSat OD and tracking.
Despite their usefulness, it is crucial to recognize that TLE data have significant inaccuracies not explicitly quantified in their datasets [7]. Indeed, the TLE data does not include any uncertainty or covariance measures. TLE accuracy varies depending on the orbit type and mission conditions. For CubeSats in LEO, the position accuracy of TLE-derived states has been reported to be around 1 km initially, with errors growing approximately 1–2 km per day. This level of accuracy is insufficient for POD or close-proximity operations [9].
Despite these limitations, TLE remain a valuable resource for initial OD and general tracking of satellites, especially when more precise tracking data are unavailable.

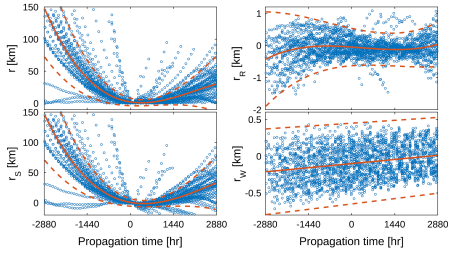

Figure 1.3: Robust regression of the position errors and (3σ) uncertainty bounds decomposed in the RSW frame [10]

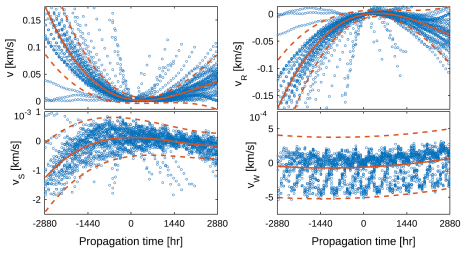

Figure 1.4: Robust regression of the velocity errors and (3σ) uncertainty bounds decomposed in the RSW frame [10]

1.5.2 On-board Sensors

In addition to ground-based observations, spacecraft and particularly CubeSats, are often equipped with on-board sensors to support autonomous navigation, attitude determination, and orbit determination. Common on-board sensors include Star Trackers, Magnetometers, Inertial Measurements Units. However this thesis does not consider the joint use of eventual on-board sensors with GNSS equipment.

1.5.3 Space-Based Observations

Space-based observation methods offer significant advantages for Orbit Determination, especially in the context of autonomous spacecraft operations. Two main categories of Space-Based Observations are commonly employed:

- **Inter-satellite links**: They allow spacecraft within a constellation or swarm to share navigation data and relative position measurements;
- **GNSS-Based Orbit Determination**: By integrating a GNSS receiver for space application on the satellite, it is possible to compute POD on-board. Within this method lies the interest of this work.

Nowadays, on-board OD is of increasingly interest even for small-satellite missions due to the availability of low-cost GNSS receivers. Indeed, GNSS-based positioning offers the potential to reduce platform design and operating costs, in contrast to traditional satellite positioning which relies on ground infrastructure [11].
When GNSS receivers are integrated into CubeSats, OD generation can occur on-board. GNSS measurements can be directly used on-board to reconstruct the orbital trajectory of a satellite by estimating its positions and velocities. Once a sufficiently accurate trajectory is reconstructed, satellite's position and velocity over time can be exported in the form of OEMs. Each OEM entry includes a timestamp (Epoch), the satellite's position (X, Y, Z), velocity $(\dot{X}, \dot{Y}, \dot{Z})$ and optionally acceleration terms $(\ddot{X}, \ddot{Y}, \ddot{Z})$. A covariance matrix may also be included following each ephemeris block. Unlike conventional TLEs, GNSS-based OEMs are derived directly from on-board measurements. This enables more autonomous and precise space operations, particularly for small satellites that operate with limited ground contact.
However, it is important to mention that implementing GNSS for space applications might face several challenges [11], such as:

- **Signal weakness and visibility**: GNSS signals are designed for terrestrial use, and in high-altitude space applications, signals are weaker and less frequently available;
- **Multipath effects and Interference**: Reflections from satellite surfaces or atmospheric disturbances can degrade positioning accuracy;
- **Time and frequency biases**: Space-grade GNSS receivers must compensate for relativistic effects.

1.6 Orbital Message Format

1.6.1 Two Line Elements

Each TLE is composed of two 69-character lines [8]. An example of TLE for the International Space Station is shown below:

```
ISS (ZARYA)
1 25544U 98067A 24199.52737269 .00001541 00000+0 37244-4 0 9993
2 25544 51.6411 38.3742 0005131 73.4092 37.5285 15.50056386436395
```

Line 1 format

Field	Description	Example
1	Line number (always 1)	1
3-7	Satellite catalog number (NORAD ID)	25544
8	Classification (U = Unclassified)	U
10-17	International designator (Launch yy, number, piece)	98067
19-32	Epoch time (YYDDD.DDDDDDDD)	24199.52737269
34-43	First derivative of mean motion (rev/day^2)	.00001541
45-52	Second derivative of mean motion (rev/day^3)	00000+0
54-61	BSTAR drag term (decimal assumed)	37244-4
63	Ephemeris type (always 0 for SGP4)	0
65-68	Element set number	999
69	Checksum	3

Table 1.1: TLE Line 1 format

Line 2 format

Field	Description	Example
1	Line number (always 2)	2
3–7	Satellite catalog number (NORAD ID)	25544
9–16	Inclination (degrees)	51.6411
18–25	Right ascension of ascending node (degrees)	38.3742
27–33	Eccentricity (decimal assumed)	0005131
35–42	Argument of perigee (degrees)	73.4092
44–51	Mean anomaly (degrees)	37.5285
53–63	Mean motion (revolutions per day)	15.50056386
64–68	Revolution number at epoch	43639
69	Checksum	5

Table 1.2: TLE Line 2 format

1.6.2 Orbital Ephemeris Message

An OEM specifies the position and velocity of a single object at multiple epochs contained within a specified time range. The OEM can also contain an optional covariance matrix that reflects the uncertainty of the orbit solution. The OEM is represented as a combination of header, metadata, data and optional comments. Each set of ephemeris data, including the time tag, must be provided on a single line [12].

```
CCSDS_OEM_VERS = 2.0
CREATION_DATE = 2019-01-08T12:00:00
ORIGINATOR    = ESOC

META_START
OBJECT_NAME   = ISS
OBJECT_ID     = 1998-067A
CENTER_NAME   = EARTH
REF_FRAME     = EME2000
TIME_SYSTEM   = UTC
META_STOP

DATA_START
2019-01-08T12:00:00  6778137.2   1234.5   345.6   -1.234   7.456   0.123
```

```
DATA_STOP

COVARIANCE_START
EPOCH = 2019-01-08T12:00:00
COV_REF_FRAME = EME2000
COV_TYPE = POSITION_VELOCITY

  (25e6)      0          0          0        0        0
   0       (25e6)        0          0        0        0
   0          0       (36e6)        0        0        0
   0          0          0       (4.0)      0        0
   0          0          0          0     (4.0)      0
   0          0          0          0        0     (4.0)
COVARIANCE_STOP
```

Field	**Section**	**Description**
CCSDS_OEM_VERS	Header	OEM format version
CREATION_DATE	Header	File creation time (UTC)
ORIGINATOR	Header	Producing organization
OBJECT_NAME	Metadata	Space object name
OBJECT_ID	Metadata	International designator
CENTER_NAME	Metadata	Reference body
REF_FRAME	Metadata	Reference frame
TIME_SYSTEM	Metadata	Time scale
Epoch + State Vector	Metadata	Time [UTC], Pos [m], Vel [m/s]
COV_REF_FRAME	Optional	Covariance reference frame
COV_TYPE	Optional	Covariance representation
Covariance matrix	Optional	6×6 covariance [m^2]

Table 1.3: CCSDS OEM message structure

1.7 Research Framework and Goals

Implementing accurate POD is fundamental to reduce the risk of collisions and preventing the generation of additional debris in LEO. This is particularly important and challenging for PQ, given the limitations imposed by their size, low cost and limited on-board resources. More specifically, the targeted PQ

are the Delfi-Twin satellites. As they lack of on-board propulsion system, they must rely solely on aerodynamic drag modulation for collision avoidance, which requires POD.
Among the various Orbit Determination methods, a promising technique is the use of low-cost, off-the-shelf GNSS receivers, which can be adapted to nanosatellite platform constraints. Unlike traditional methods, which are typically based on ground-tracked TLEs, this thesis explores an approach that uses simulated GNSS measurements to perform on-board orbit determination and prediction.
Both single-frequency and dual-frequency GNSS receiver configurations are tested to quantify the influence of measurement precision on overall orbit estimation and prediction performance.
Finally, the resulting orbital solutions are formatted into OEMs and compared with conventional TLEs. The aim is to show that GNSS-based OEMs can provide an accurate alternative to POD.

1.8 Workflow of the study

To achieve the outlined objectives, the following workflow was followed:

- A reference trajectory, referred to as True Orbit, is generated using the Technical University of Delft Astrodynamics Toolbox (TUDAT) astrodynamics software. This trajectory serves as the input for the Skydel GNSS simulator (Chapter 4.4).
- Skydel simulates GNSS signals corresponding to the True Orbit. These signals are then processed using both single-frequency and dual-frequency GNSS receiver configurations (Chapter 4.5).
- The simulated GNSS measurements are used to perform orbit determination in TUDAT, resulting in an Estimated Orbit (Chapter 4.6).
- The Estimated Orbit is then propagated forward in time, again using TUDAT, to produce a Predicted Orbit (Chapter 4.7).
- Both the Estimated and Predicted Orbits are compared to the original True Orbit to assess accuracy, error characteristics, and overall performance (Chapter 5.4, 6.3).

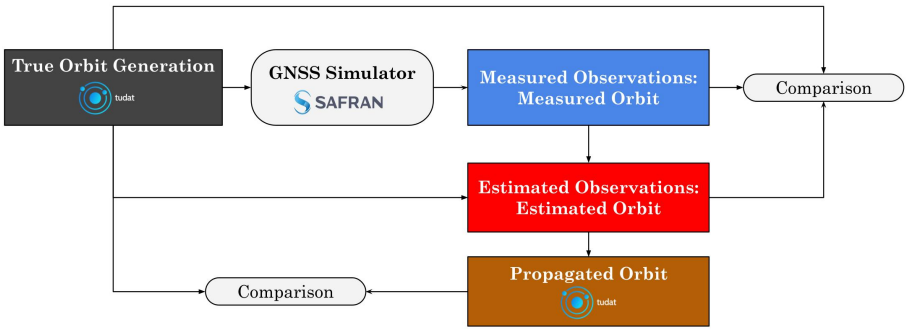

Figure 1.5: GNSS Simulator - Workflow

To further evaluate the quality of GNSS-based orbit determination, TLEs are also generated directly from the GNSS measurements. These TLEs are then propagated using the SGP4 model and compared against the other orbit solutions. This enables a direct comparison between GNSS-based OEMs and the widely used TLE format.

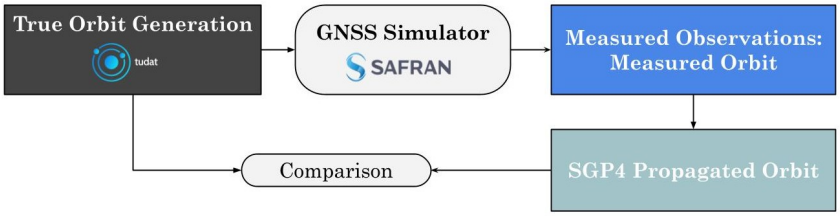

Figure 1.6: TLE Generation - Workflow

1.9 Thesis Outline

The development of this thesis followed a logical sequence, as shown in Figure A.1 - G.1, and is organised as follows:

- **Chapter 2** provides the theoretical background on satellite navigation, GNSS metrics and data formats;
- **Chapter 3** introduces the fundamentals of orbital mechanics and describes

the reference frames and coordinate systems used. It also offers an overview of the Earth's shape, applied coordinate conversions and orbital perturbations;

- **Chapter 4** details the generation of the True, Measured and Estimated and Propagated orbit;
- **Chapter 5** presents and discusses the GNSS-Based Orbit Determination, obtained for both single-frequency and dual-frequency GNSS receivers, considering perturbed and unperturbed orbits;
- **Chapter 6** presents and discusses the GNSS-Based Orbit Propagation, obtained for both single-frequency and dual-frequency GNSS receivers, considering perturbed and unperturbed orbits;
- **Chapter 7** focuses on generating TLEs and propagating them using the SGP-4 model;
- **Chapter 8** concludes the thesis by summarising the key findings of the study and proposing recommendations for future developments.

Chapter 2

Basics of Global Satellite Navigation System

2.1 Introduction to Navigation and GNSS

The human drive to explore is as old as humanity itself, an instinctive need that has shaped our evolution: our sense of orientation merges a set of abilities developed over time, including the skills of localization and navigation. The former refers to the ability to determine our position with respect to a reference system; the latter involves the description of how to proceed from a starting point to a chosen one.

For centuries, humankind has relied on the available instruments and references: from the starry sky, to paper maps, to lighthouses on the open sea. Over time, these methods have evolved radically: today, we no longer need to consult maps or look to the stars to find our way.

Modern navigation systems are yet another technological solution invented by humans to solve this instinctive problem. In recent years, indeed, few people have truly been lost, largely thanks to a powerful yet accessible technology that fits in our pockets. These systems are commonly referred to as Global Positioning System (GPS), but are more accurately known as GNSS, and they have deeply changed the interaction with the surrounding world.

The term GNSS refers to a satellite-based navigation system capable of providing global positioning services. It consists of three main components:

- **Space Segment** includes the constellation of satellites orbiting the Earth and transmitting navigation signals;
- **Control Segment** composed of a global network of monitoring and control stations that track satellite orbits, manage system integrity, and upload updated navigation data to the satellites;
- **User Segment** comprising GNSS receivers that identify the satellites in view, estimate the pseudorange, and compute the user's Position, Velocity, and Time (PVT) solution accordingly.

Currently, the Space Segment is composed by four global systems: the United States's GPS, Russia's GLONASS, China's Beidou, and the European Union's Galileo.
Each GNSS satellites broadcasts a signal that contains orbital data and the precise time the signal was transmitted. This ensures that the position of GNSS satellites is accurately known in both time and space. As a result, GNSS provides a powerful tool by offering an absolute reference frame for positioning and navigation. Modern localization is therefore based on artificial references in space, "new stars" that remain visible even under cloudy skies.
This work focuses on the use of GNSS to accurately determine the position of the satellites of interest.

2.2 Fundamentals of Satellite Navigation

The GNSS Space Segment is a space-based satellite navigation system able to provide location and time information in all weather conditions, wherever there is an unobstructed line of sight to four or more GPS satellites.
Each GNSS satellite broadcasts the navigation message and the ranging signals, used to measure the distance between the receiver and the satellite. The navigation message includes ephemeris data, precise information about the satellite's trajectory over time, and almanac data, set of ephemeris of the entire space constellation, which provide a broad overview of where each satellite should be at any given time. Therefore, the position of the GNSS satellites are well known.
The GNSS receiver gathers the signals and determines the signal propagation time by comparing the transmission time t_{TX}, encoded in the satellite's signal, with the reception time t_{RX}, measured by the receiver's internal clock. The

propagation delay is computed as:

$$\Delta t = t_{RX} - t_{TX} \tag{2.1}$$

This time delay is then used to estimate the pseudorange, a pseudo distance between the satellite and the GNSS receiver, given by:

$$\rho = c \cdot \Delta t = c \cdot (t_{RX} - t_{TX}) \tag{2.2}$$

where c is the speed of light. After computing the pseudoranges from at least four GNSS satellites, the next step is to solve the following nonlinear system of equations to estimate the receiver's position (x, y, z) and its clock bias δt.

$$\begin{cases} \rho_1 = \sqrt{(x - X_1)^2 + (y - Y_1)^2 + (z - Z_1)^2} + c \cdot \delta t \\ \rho_2 = \sqrt{(x - X_2)^2 + (y - Y_2)^2 + (z - Z_2)^2} + c \cdot \delta t \\ \rho_3 = \sqrt{(x - X_3)^2 + (y - Y_3)^2 + (z - Z_3)^2} + c \cdot \delta t \\ \rho_4 = \sqrt{(x - X_4)^2 + (y - Y_4)^2 + (z - Z_4)^2} + c \cdot \delta t \end{cases} \tag{2.3}$$

Here, (X_i, Y_i, Z_i) are the known positions of the i-th satellite at the time of transmission, and δt is the receiver clock offset with respect to GNSS system time.
Since δt is unknown, the user needs measurements from at least four satellites in line of sight to determine the four unknowns $(x, y, z, \delta t)$. The bias of the user clock, thus, is not an error but one dimension of the problem.
GNSS-based positioning is commonly given by the intersection of pseudospheres. The geometric solution to the user's position is the point where at least four of these pseudospheres intersect. To solve the overall system of equations, a linearization process of the spheres must be applied. The linearized system is expressed in matrix form as:

$$\Delta\rho = H \cdot \Delta x \tag{2.4}$$

$\Delta\rho$ is the vector of pseudorange residuals, the difference between the measured pseudoranges and those computed from the current position estimate;
H is the geometrical or Jacobian matrix, containing the partial derivatives of the pseudoranges with respect to the receiver position and clock bias;
Δx is the state vector, the correction vector to the current state estimate, typically expressed as $\Delta x = [\Delta x, \Delta y, \Delta z, c \cdot \Delta t]^T$.
This system is solved iteratively, updating the receiver state at each step until

the residuals $\Delta\rho$ fall below a defined convergence threshold.

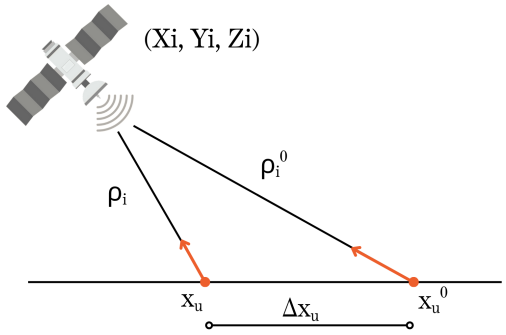

Figure 2.1: Visualization of the Linearization Process

2.3 Error Sources

The received GNSS signal and its power are attenuated by many factors along the signal's propagation path. An important aspect of satellite navigation involves understanding the sources of the errors, to quantify their contribution to the total error, and to estimate the effect on PVT accuracy. All of the following sources contribute to errors in pseudorange.

- **Ephemeris Errors**: The Space Segment contributes to errors by transmitting imperfect signals containing not accurate information. GNSS satellites do not continuously broadcast their instantaneous positions. Instead, users compute satellite positions based on the ephemerides, which are time-dependent. Any inaccuracies in these parameters lead directly to positioning errors;
- **Clock drifts**: GNSS satellites are equipped with high-precision atomic clocks, while user receivers typically employ less accurate clocks due to size, cost, and power constraints. A timing error as small as 1 μs can result in a position error of approximately 300 m, since GNSS signals travel at the speed of light.
- **Orbit drifts**: Similarly to the satellite clock, a slight change in the satellite's predicted orbit can lead to positional error. Usually, the ephemeris broadcast of each satellite is updated every 2 hours, to correct both the satellite clock error and the orbit parameters.
- **Multipath error**: Signal can be reflected by buildings, terrain, or water bodies before reaching the receiver.

- **Ionospheric Error**: The ionosphere, extending roughly from 50 to 1000 km above Earth, contains free electrons and ions produced by solar radiation. These charged particles cause dispersive delays in GNSS signals.
- **Tropospheric Delay**: The troposphere, the lowest layer of Earth's atmosphere, extending up to 50 km contains dry gases and water vapour. These refract signals, causing a delay in signal propagation. This delay is independent of frequency.

Ionospheric Error

Of particular interest for this work are the ionospheric errors and their mitigation methods. It is well known in the literature that the ionosphere introduces a significant and frequency-dependent delay in GNSS signals [13]. Ionospheric bias is, indeed, the only error source that depends on the carrier frequency. Two main approaches exist to mitigate this error, depending on the type of GNSS receiver employed, which could be single- or dual-frequency.

In the single-frequency approach, the user receives the GNSS signal at only one carrier frequency, and ionospheric delay corrections are applied using empirical models broadcasted by the GNSS constellation, such as the Klobuchar model or the NeQuick model. These models approximate the Total Electron Content (TEC) in the ionosphere and provide a correction term based on time, location, and satellite elevation.

On the other hand, dual-frequency receivers receive signals from the same satellite on two distinct carrier frequencies. Since the ionospheric bias is inversely proportional to the square of the frequency, the difference in delays observed at the two frequencies can be used to directly estimate and remove the ionospheric effect. The ionosphere-free pseudorange ρ^* is expressed as:

$$\rho^* = \frac{f_1^2}{f_1^2 - f_2^2}\rho_{f_1} - \frac{f_2^2}{f_1^2 - f_2^2}\rho_{f_2} \tag{2.5}$$

where ρ_{f_1} and ρ_{f_2} are the pseudoranges computed at respectively f_1 and f_2 frequencies.

The following chapters will better detail how the use of single- and dual-frequency receivers actually impact and improve the positioning accuracy in the thesis itself.

2.4 Signal Quality and Geometrical Performance Metrics

Both geometrical factors and signal quality metrics are widely used to define the accuracy of a user's estimated position with respect to its true position [14].

2.5 Carrier to Noise Ratio

The Carrier-to-Noise Density Ratio, usually referred to as $\frac{C}{N_0}$ is the ratio between the power of the received GNSS carrier signal C, and the power spectral density of the noise N_0. It is expressed in decibels-Hertz $\frac{dB}{Hz}$.
$\frac{C}{N_0}$ is widely used a performance metrics: an higher value if $\frac{C}{N_0}$ indicates a stronger and clearer signal, so better accuracy and reliability. On the other hand, a lower $\frac{C}{N_0}$, represents a weaker or noisier signal, where more errors or signal loss are likely to occur.

2.6 Geometrical Diluition of Precision

Considering the design matrix H, defined in the linearized navigation equation, the GDOP is computed as

$$GDOP = \sqrt{tr(H^T \cdot H)^{-1}} \tag{2.6}$$

where tr() denotes the trace of a matrix, and $(H^T \cdot H)^{-1}$ is the inverse of the normal matrix associated with the least-squares solution.

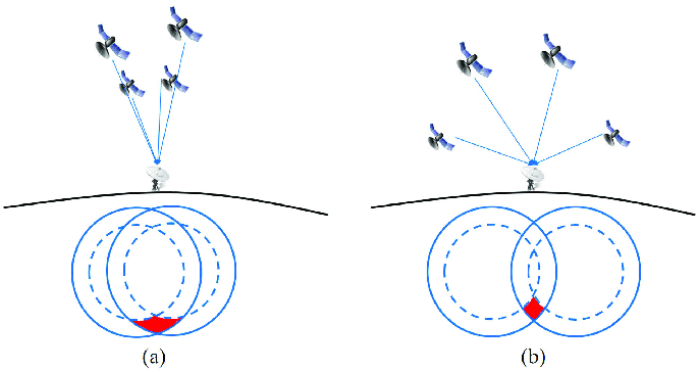

Figure 2.2: GDOP Visualization [15]

The Geometrical Diluition of Precision (GDOP) expresses how the geometry of the satellite constellation affects the quality of the position solution. The GDOP varies depending on several conditions, primarily relating to the geometry of the satellite constellation in relation to the receiver. The main factor affecting the GDOP, and the pseudorange error, is the spatial displacement of the satellites in relation to the receiver. When satellites are spread evenly across the sky, the geometry is more ideal, resulting in a lower GDOP and higher positional accuracy.

2.7 Root Mean Square Error

Root Mean Square Error (RMSE) of the position estimate is an important metric in satellite navigation, representing the standard deviation of the positioning error. It can be expressed as:

$$RMSE = \sigma_x = \sqrt{\sigma_{x_u}^2 + \sigma_{y_u}^2 + \sigma_{z_u}^2 + \sigma_{b_{ut}}^2} \tag{2.7}$$

where $\sigma_{x_u}^2, \sigma_{y_u}^2, \sigma_{z_u}^2$ are the variances of the estimated position components, and $\sigma_{b_{ut}}^2$ is the variance of the estimated receiver clock bias. Generally speaking, it represents the statistical spread of the estimated position around the true value. The RMSE is independent of the specific reference system used.

2.8 Covariance Matrix

Another important and useful concept in satellite navigation is the Covariance Matrix.
Covariance typically refers to a measure of how two variables change together. The Covariance Matrix is a square matrix containing the variances of the individual variables on the diagonal, and the covariances between them off-diagonal. Variances represent the uncertainty of a single variable, while covariances describe the relationships between them.

$$C_{\delta x} = \begin{bmatrix} \sigma_{x_u}^2 & \sigma_{x_u,y_u}^2 & \sigma_{x_u,z_u}^2 & \sigma_{x_u,b_{ut}}^2 \\ \sigma_{y_u,x_u}^2 & \sigma_{y_u}^2 & \sigma_{y_u,z_u}^2 & \sigma_{y_u,b_{ut}}^2 \\ \sigma_{z_u,x_u}^2 & \sigma_{z_u,y_u}^2 & \sigma_{z_u}^2 & \sigma_{z_u,b_{ut}}^2 \\ \sigma_{b_{ut},x_u}^2 & \sigma_{b_{ut},y_u}^2 & \sigma_{b_{ut},z_u}^2 & \sigma_{b_{ut}}^2 \end{bmatrix}$$

Starting from this definition, the concept of covariance is used in OD, representing a powerful tool to understand and manage the uncertainties. In particular, the Covariance Matrix defines a confidence region around the estimated position and velocity. Therefore, it is an important parameter for conducting collision analysis, as well as predictions analysis.

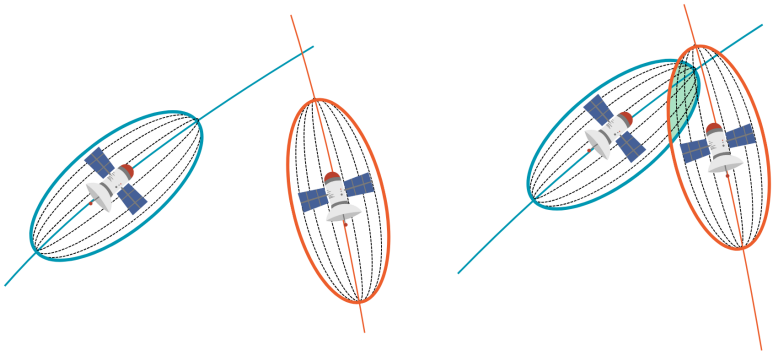

Figure 2.3: Visualization of Covariance

2.9 Formal Errors

Formal Errors are derived from the Covariance Matrix. Specifically, they are obtained by taking the square roots of the diagonal elements of the matrix itself. While the Covariance Matrix provides a comprehensive view of uncertainties, Formal Errors give a direct measure of uncertainty for each parameter separately.

2.10 Accuracy and Precision

Accuracy and Precision are key performance metrics in evaluating the quality of orbit determination solutions.
For a static user, accuracy is a measure of how close a point is to its true position; precision is the measure of how closely the estimated points are in relation to each other. Although these definitions originate from static positioning contexts, they can be extended to the case of an orbiting satellite. In this context, accuracy refers to how closely the Estimated Orbit matches the True (Reference) Orbit, while precision describes the consistency of the position estimates over time. Both metrics are essential to assess the quality of the orbit reconstruction processes.

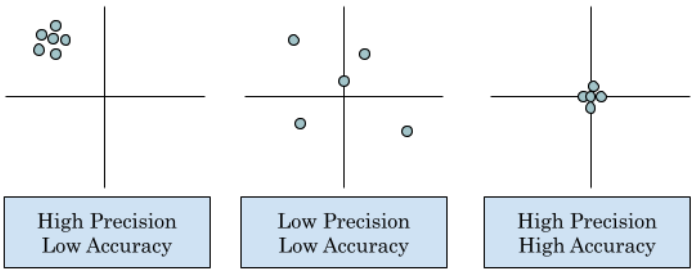

Figure 2.4: Precision and Accuracy Visualizations

2.11 Sky Plot

The SkyPlot provides a visual representation of the GNSS satellites above the local horizon of the user, giving a snapshot of the GNSS satellite geometry in the sky at a given time. This plot assumes an open-sky condition, although in real environments, obstacles may block signals from satellites at lower elevation angles. However, since the user in this work is represented by a LEO satellite, no obstacles are blocking the signal in the simulation.
It is important to distinguish between the satellites in view from those actually used in the position fix. Often, more satellites are visible than those selected for the PVT solution. Satellites may be excluded due to different factors, such as poor signal quality, low elevations or poor signal quality metrics like the $\frac{C}{N_0}$. For this reason, GDOP and $\frac{C}{N_0}$ represents important metrics, offering insight into the reliability of the measurements.

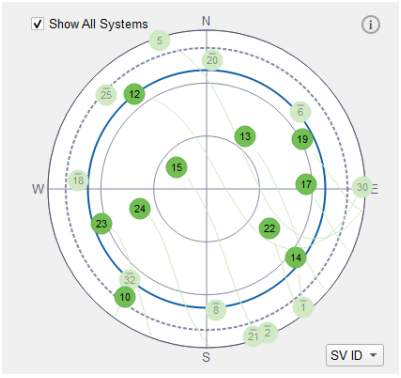

Figure 2.5: Skydel SkyPlot: the blue line represents the elevation cut-off

2.12 GNSS Data Formats

GNSS receivers output positioning, timing and navigation data in different formats. Each format is designed to transmit specific types of information and may be exclusive to a particular receiver manufacturer. These data messages form the basis of the work presented in this thesis: they are parsed and interpreted. The most commonly used GNSS data formats include:

- **NMEA (National Marine Electronics Association)**: An ASCII text-based format, widely used across GNSS receivers. It includes various standard sentence types, which are initialized with specific set of letters such as GGA, RMC.
- **SBF (Septentrio Binary Format)**: A binary format specific to Septentrio receivers. It offers an efficient and high-resolution access to raw GNSS data, including receiver clock biases, time system information and quality indicators.
- **RINEX (Receiver Independent Exchange Format)**: A standardized ASCII format for storing raw GNSS observations and navigation data from multiple constellations. It is widely used in scientific and geodetic applications.
- **UBX (u-blox Binary Protocol)**: A format used by u-blox receivers, enabling transfering of both raw and processed GNSS data.

In this work, the focus is on the NMEA and SBF formats, as these correspond to the data sources used in the experimental setup: the Skydel Single Frequency Receiver and the Septentrio Dual Frequency receiver.

2.13 NMEA Messages

GNSS receiver outputs are often provided in the form of National Marine Electronics Association (NMEA) messages, consisting of multiple ASCII sentence types. For this work, the relevant ones are `$GNGGA` and `$GNRMC`, which contain essential information for orbit determination and time-tagging.
In this work, only a subset of fields from the following messages is extracted:

GNGGA: Time, position, and fix-related data of the receiver.
Format:

`hhmmss.ss,llll.lll,a,yyyyy.yyy,a,x,uu,v.v,w.w,M,x.x,M„zzzz*hh<CR><LF>`

- **UTC Time (hhmmss.ss)**: Timestamp of position fix.
- **Latitude (ddmm.mmmm)**: Geographical coordinate with hemisphere indicators (N/S).
- **Longitude (dddmm.mmmm)**: Geographical coordinates with hemisphere indicators (E/W).
- **Altitude (m)**: Orthometric height above mean sea level.
- **Geoidal Separation (m)**: Difference between the geoid and the WGS84 ellipsoid.

GNRMC: Time, date, position, course, and speed data.
Format:
`hhmmss.sss,x,llll.lll,a,yyyyy.yyy,a,x.x,u.u,xxxxxx„,v*hh<CR><LF>`

- **UTC Time (hhmmss.sss)**: Timestamp of navigation message.
- **Latitude and Longitude**: Same as in GNGGA.
- **UTC Date (ddmmyy)**: Date of fix.

It is important to state that the altitude provided in the GNGGA message corresponds to the orthometric height, and differs from the ellipsoidal height. However, the geoidal separation field within the same message can be used to convert from orthometric to ellipsoidal height.

2.14 Septentrio Binary Format

The Septentrio Binary Format (Septentrio Binary Format (SBF)) is a binary format developed by Septentrio to store raw GNSS measurement data efficiently. Unlike NMEA, SBF is not human-readable and is intended for automated data processing. Parsing requires dedicated software, such as *RxTools*, which was used in this work to extract navigation data.
The output of SBF parsing contains a wide range of information. However, for the purposes of this thesis, only a subset of this data was used, specifically:

- **Week Number (WNc)**: The current GPS week, starting from the GPS time origin.

- **TOW (Time of Week)**: GNSS time expressed in milliseconds from the start of the current GPS week.
- **Latitude** and **Longitude** in *radians*, referenced to the WGS84 ellipsoid.
- **Height** in *meters* above the ellipsoid.
- **Undulation** in *meters*, representing the geoidal separation from the ellipsoid.
- **Receiver Clock Bias (clB)** in *milliseconds*, which is subtracted from the GNSS time to compute the actual UTC-based timestamp.

The complete GPS timestamp is reconstructed by combining the WNc, TOW and clB. Specifically, the UTC time is calculated as:

$$t_{UTC} = Epoch_{GPS} + (WNc \cdot 604800 + TOW - clB) \tag{2.8}$$

where the $Epoch_{GPS}$ starts on January 6, 1980 at 12:00:00.

Chapter 3

Basics of Orbital Mechanics

This chapter covers all the fundamental concepts of Orbital Mechanics necessary to understand the development of the work. The motion of a satellite orbiting a generic orbit can be described by several reference systems: frames and conversions used in the thesis will be explained.
The various perturbative accelerations included in the estimator and propagator used will be introduced as well, as they have fundamental importance in creating an environment as similar as possible to the real operative case.

3.1 Keplerian Orbital Elements

The position and motion of a satellite along its orbit are commonly described using the Keplerian orbital elements. The sixth parameter allows to specify the satellite's position along the orbit 3.1:

- **Semi-major axis (a):** a constant defining the size of the conic orbit;
- **Eccentricity (e):** a constant defining the shape of the conic orbit;
- **Inclination (i)**: the angle between the $\hat{k}$ unit vector and the angular momentum vector $\bar{h}$;
- **Longitude of the ascending node (Ω):** the angle, in the fundamental plane, between the $\hat{I}$ unit vector and the point where the spacecraft

crosses through the fundamental plane in a northerly direction (ascending node) measured counterclockwise when viewed from the north side of the fundamental plane. This angle is also known as Right Ascension of the Ascending Node (RAAN) angle;

- **Argument of periapsis (ω)**: the angle, in the plan of the satellite's orbit, between the ascending node and the periapsis point, measured in the direction of the satellite's motion;
- **True anomaly at epoch (ν_0):** the angle, in the plane of the spacecraft's orbit, between periapsis and the position of the satellite at a particular time, t, called the "epoch".

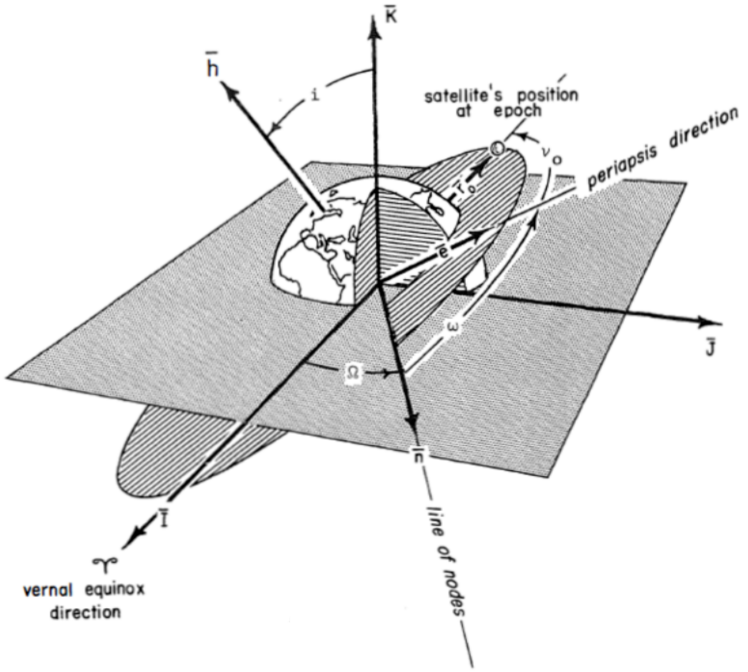

Figure 3.1: Keplerian Orbital Elements

3.2 Reference Frames and Coordinate Systems

All reference frames used are right-handed. Each reference frame is defined by an origin and a set of orthogonal axes.

3.2.1 Earth-Centered Inertial Reference Frame

In the ECI Frame, or Cartesian Frame, the origin is at the center of the Earth. Its axes are defined as:

- X_{ECI} is given by the intersection of the ecliptic with the equatorial plane during the Vernal equinox, thus the direction is such that, during the Vernal equinox the Earth sees the Sun in the Aries constellation;
- Z_{ECI} is perpendicular to the equatorial plane with the direction toward the hemisphere that contains Polaris;
- Y_{ECI} completes the right-handed triad

The term "inertial" refers to a coordinate system non-rotating with the Earth, but fixed with respect to the stars.

J2000 Reference Frame

J2000 is a specific realization of the ECI frame, defined by the position of the mean equator and equinox of the Earth on January 1st 2000 at 12:00:00.
In J2000 reference frame, therefore, the origin is at the center of the Earth, and its axes are:

- $X_{ECI_{J2000}}$ towards vernal equinox;
- $Z_{ECI_{J2000}}$ aligned with Earth's rotation axis as it was at the J2000 epoch. This frame is inertial, so its Z direction does not move with the Earth's rotation axis;
- $Y_{ECI_{J2000}}$ completes the right-handed triad

J2000 is used within the context of TUDAT, which performs its computation in this reference frame.

TEME Reference Frame

True Equator Mean Equinox (TEME) is a specific ECI frame most commonly used with TLEs and the SGP-4 propagator. Its axes are defined as:

- $X_{ECI_{TEME}}$ points toward the mean equinox (so averaged over time, no nutation)
- $z_{ECI_{TEME}}$ aligned with the true rotation axis of the Earth at the observation time

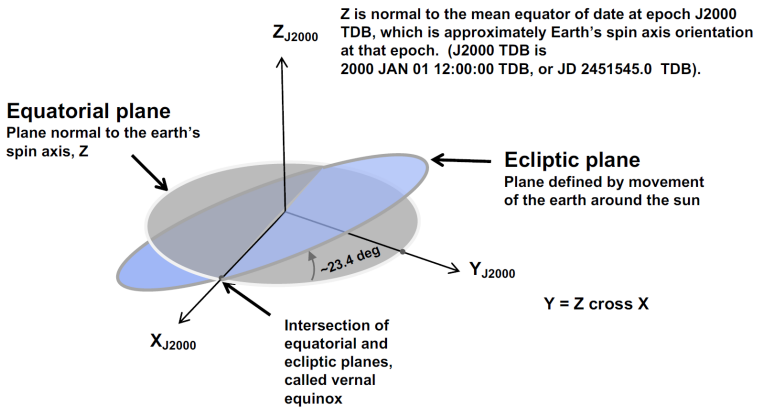

Figure 3.2: J2000 Reference Frame

- $Y_{ECI_{TEME}}$ Completes the right-handed triad

However, it is important to point out that TEME is not rigorously defined in the same way as modern celestial reference frames like J2000. Indeed, it includes some effects of Earth's motion (e.g. nutation in the equator), but not others (e.g. precession in the equinox), making it inconsistent in terms of frame transformations.

3.2.2 Earth-Centered Earth-Fixed Reference Frame

The Earth-Centered Earth-Fixed (ECEF) Frame rotates with the Earth with respect to the stars, which makes it a non-inertial reference frame, rotating at an angular velocity equal to $\omega = 7.29218e5\frac{rad}{s}$. The axes are defined as follows:

- X_{ECEF} points toward the Earth's prime meridian, lying in the equatorial plane;
- Z_{ECEF} points toward the North Pole, being normal to the equatorial plane, overlapping
- Y_{ECEF} completes the right-handed triad.

ECEF primary axis is always aligned with the Greenwich meridian as the principal direction, thus it is necessary to define an epoch: the J2000 will be the reference, as previously defined.

3.2.3 Radial Along-Track Cross-Track Coordinate System

When referring to a single satellite, it is useful to define a coordinate system where the satellite itself is the origin. The Radial, Along-Track, Cross-Track (RSW) Coordinate System is a local coordinate system used to describe the motion of one satellite with respect to the other, where:

- R points in the radial direction, pointing from its central body toward the center of the Earth (its central body);
- S points in the direction of the satellite's motion and perpendicular to the radial axis (the velocity usually is not aligned with the radial axis);
- W completes the right-handed triad.

The RSW frame is used, in the context of this thesis, to obtain a more objective measurement of the difference between the True, Measured, Estimated and Propagated orbits.

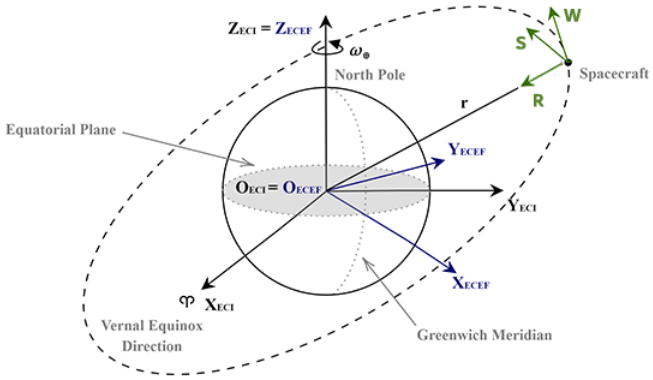

Figure 3.3: ECI and ECEF Reference Frames; RSW Coordinate System

3.2.4 Geographic Cordinate System: Latitude and Longitude

The position of a point on or near the Earth's surface is commonly expressed in **geographic coordinates**, consisting of:

- **Latitude** (ϕ): the angle between the equatorial plane and the line normal to the reference ellipsoid at a given point;

- **Longitude** (λ): the angle in the equatorial plane between the prime meridian (Greenwich) and the meridian passing through the point;
- **Altitude** or **Height** (h): the distance from the point to the reference ellipsoid surface, measured along the ellipsoid normal.

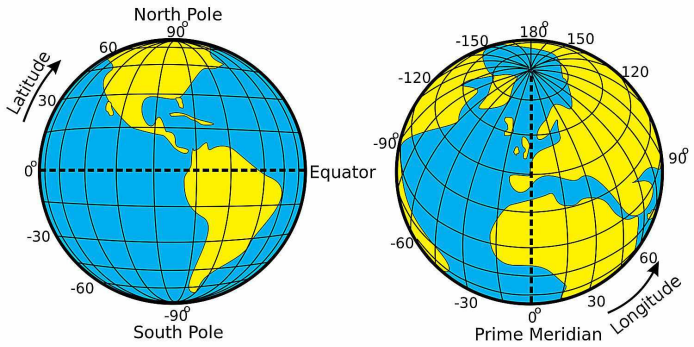

Figure 3.4: Latitude and Longitude Visualization

3.3 Earth Shape

Once the reference frames and coordinate systems used to describe satellite motion have been introduced, it is essential to consider the shape of the Earth itself. Although simple models approximate the Earth as a perfect sphere, its oblate, non-uniform shape must be taken into account to achieve high-accuracy performance. Earth affects both the gravity experienced by satellites and the interpretation of GNSS measurements.

3.4 Earth Ellipsoid

The Earth Ellipsoid, or Reference Ellipsoid, is a mathematically defined surface that approximates the shape of the Earth. It is an oblate spheroid, formed by rotating an ellipse about its minor axis, and is used as a simplified model of the Earth's geometry for geodetic and mapping purposes. It can also be referred to as Geodetic Ellipsoid.

WGS84

The WGS84 is a standard Geodetic Reference Frame. It represents a mathematical model of the Earth from a geometric, geodetic and gravitational perspective, based on the measurement, scientific knowledge and available technologies up to 1984. It is important to clearly define the concept of WGS84 because most GNSS receivers use this model as their default reference frame for position computation. It is defined as follows:

- Center in the center of mass of the Earth;
- Z_{WGS84} points toward the North Pole as defined from Bureau International de l'Heure (BIH) in 1984;
- X_{WGS84} points toward the Greenwich meridian;
- Y_{WGS84} completes the right-handed triad.

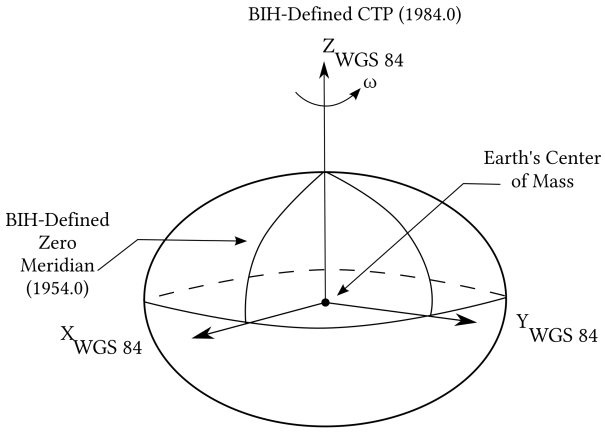

Figure 3.5: WGS84 Reference Frame: the oblateness of the ellipsoid is exaggerated in this image

3.5 Geoid Definition

The Geoid is the equipotential surface of the Earth's gravitational field that best fits, in a least-squares sense, the global mean sea level. Unlike the ellipsoid, it accounts for variations in Earth's gravity and provides a more physically meaningful reference for measuring elevations.

Geoidal Separation

Since the definition of Geodetic and Geoidal ellipsoid differ, it is important to properly define the relationship between these surfaces. The only difference is in the definition of the height:

$$h = H + N \tag{3.1}$$

where:

- h is the ellipsoidal or geodetic height (above the WGS84 ellipsoid),
- H is the orthometric or geoidal height (above the geoid, or MSL),
- N is the geoidal separation, the distance between the geoid and the ellipsoid.

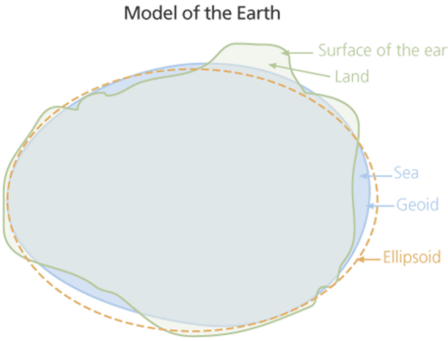

Figure 3.6: Model of the Earth [16]

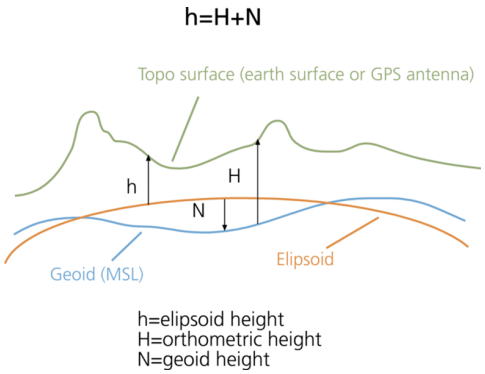

Figure 3.7: Difference between Geoid and Ellipsoid [16]

In the Orbit Determination and Propagation simulations developed in this thesis using TUDAT, the Earth is modelled as an oblate spheroid, consistent with the WGS84 ellipsoid parameters. This is done by specifying:

- An equatorial radius of $R = 6\,378\,137\,\text{m}$;
- A flattening factor of $f = \frac{1}{298.257}$.

In standard NMEA messages, the altitude field represents the orthometric height, which is the height above the geoid. To convert it to ellipsoidal height, the geoid undulation N must be added. In contrast, the altitude field in the SBF message directly provides the ellipsoidal height, so no correction for geoid separation is required.

3.6 Conversions

Given that GNSS positioning data is provided in ellipsoidal latitude, longitude, and altitude, it is necessary to convert this information into a Cartesian coordinate system for use in Orbit Determination and Propagation. This involves two key transformations: first, converting latitude and longitude from degrees and decimal minutes to decimal degrees; and second, converting from the Latitude, Longitude, Altitude (LLA) coordinate system to the ECEF reference frame. In order to assess Orbit Determination and Propagation errors more accurately, it is useful to represent position differences in the RSW reference frame. Therefore, additional conversions from the ECEF and ECI reference frames to the RSW reference frame must also be defined.

From Degrees and Decimal Minutes into Decimal Degrees
NMEA sentences encode latitude and longitude in the Degrees and Decimal Minutes (DDM) format, which must be converted into Decimal Degrees (DD) for further processing, as follows:

$$Latitude(DD) = degrees + \frac{minutes}{60} \tag{3.2}$$

$$Longitude(DD) = degrees + \frac{minutes}{60} \tag{3.3}$$

Sign corrections are applied based on hemisphere indicators:

- 'S' $\rightarrow$ negative latitude
- 'W' $\rightarrow$ negative longitude

This is not necessary for SBF Messages, where Longitude and Latitude are expressed in radians.

From LLA to ECEF
Once the latitude, longitude are in decimal degrees and meters, the next step is to convert LLA into the ECEF frame. This conversion assumes an oblate spheroid, specifically an WGS84 ellipsoid with the following parameters:

- An equatorial radius of $R = 6\,378\,137\,\text{m}$;
- A flattening factor of $f = \frac{1}{298.257}$.
- Eccentricity squared: $e^2 = 2f - f^2$

Defining ϕ as latitude, λ as longitude, h as the height above ellipsoid, and N as the radius of curvature in the prime vertical, the ECEF coordinates $(X_{ECEF}, Y_{ECEF}, Z_{ECEF})$ are computed as:

$$X_{ECEF} = (N + h)cos(\phi)cos(\lambda) \tag{3.4}$$

$$Y_{ECEF} = (N + h)cos(\phi)sin(\lambda) \tag{3.5}$$

$$Z_{ECEF} = [(1 - e^2)N + h]sin(\phi) \tag{3.6}$$

From ECEF or ECI to RSW

To analyse orbital errors in a satellite-centric frame, position differences originally expressed in the ECEF or ECI frame are transformed into the RSW frame [17], [18].

First, the satellite's position $\vec{r}_{SAT}$ and velocity $\vec{v}_{SAT}$ vectors are extracted from the True Orbit values expressed in the ECEF frame. Their magnitudes are computed as:

$$\vec{r}_{SAT} = \sqrt{X_{ECEF}^2 + Y_{ECEF}^2 + Z_{ECEF}^2} \tag{3.7}$$

$$\vec{v}_{SAT} = \sqrt{V_{X_{ECEF}}^2 + V_{Y_{ECEF}}^2 + V_{Z_{ECEF}}^2} \tag{3.8}$$

Then, the unit vectors defining the RSW frame are built:

$$\hat{R} = \frac{\vec{r}_{SAT}}{||\vec{r}_{SAT}||} \tag{3.9}$$

$$\hat{W} = \frac{\vec{r}_{SAT} \times \vec{v}_{SAT}}{||\vec{r}_{SAT} \times \vec{v}_{SAT}||} \tag{3.10}$$

$$\hat{S} = \hat{W} \times \hat{R} \tag{3.11}$$

Once the RSW frame is defined, the position difference vector in ECEF coordinates, $\Delta\vec{r}_{ECEF}$, is projected into the RSW frame using a rotation matrix constructed from the three unit vectors:

$$\Delta\vec{r}_{RSW} = \begin{bmatrix} \hat{R} \\ \hat{S} \\ \hat{W} \end{bmatrix} \cdot \Delta\vec{r}_{ECEF} \tag{3.12}$$

3.7 Orbital Perturbations

In a real space operational scenario, the satellite experiences perturbative forces that deviate its motion from the two-body Keplerian orbit. To accurately model the orbital evolution and simulate realistic conditions for LEO satellite, the following perturbations have been considered: Earth's gravitational field, Aerodynamic drag and Solar Radiation Pressure.

3.7.1 Earth's gravitational field

The Earth's gravitational field is modeled using spherical harmonics up to degree and order 5, accounting not only for the dominant J2 (equatorial bulge) effect, but also higher-order zonal and tesseral terms that introduce additional perturbations to the orbit.
The Earth's mass distribution, indeed, is not perfectly spherical, and its equatorial bulge introduces a perturbative effect in the gravitational field. This means that the oblateness of the Earth causes a regression of the line of nodes, a rotation of the line of apsides along with a change of the mean anomaly.

3.7.2 Athmospheric Drag

LEO satellites experience differential forces caused mainly by the aerodynamic differential drag. The effect of the atmosphere can be expressed as follows:

$$a_D = -\frac{1}{2}\rho\frac{SC_D}{m}V_r^2 \tag{3.13}$$

where:

- a_D is the acceleration due to drag $[m/s^2]$;
- ρ is the atmospheric density at the satellite's current altitude $[kg/m^3]$, which could be estimated using different models. This work uses the NRLMSISE-00 model, an empirical, global atmospheric reference model for the Earth from the ground to space. It is used to model the temperatures and densities of the atmosphere's components.
- S is the reference cross-sectional area of the satellite exposed $[m^2]$;
- C_D is the dimensionless drag coefficient, which depends on the shape and surface properties of the satellite;

- m is the mass of the satellite $[kg]$;
- V_r is the relative velocity of the satellite with respect to the atmosphere $[m/s]$.

The minus sign indicates that a_D acts in the opposite direction to the velocity.

3.7.3 Solar Radiation Pressure

For a LEO satellite, the Sun causes disturbances in the form of electromagnetic radiation, transferring momentum, with a resulting effect nearly equal to zero, result in variations not only in the eccentricity and semi-major axis. The resulting acceleration can be expressed as:

$$a_{SRP} = \frac{P_S \, C_R \, A}{m} \tag{3.14}$$

where:

- a_{SRP} is the acceleration due to SRP $[m/s^2]$.
- P_S is the solar radiation pressure at 1 AU, approximately 4.5×10^{-6} Pa.
- C_R is the radiation pressure coefficient (dimensionless), typically between 1.0 and 1.5.
- A is the effective cross-sectional area exposed to solar flux $[m^2]$.
- m is the mass of the satellite $[kg]$.

Chapter 4

Signal Generation, Determination and Propagation

4.1 Tudat

The TU Delft Astrodynamics Toolbox (TUDAT) is a powerful set of C++ libraries that support astrodynamics and space research. At the core of TUDAT is the numerical propagation of orbits. For the purposes of this thesis, the Tudatpy Python interface has been used. This toolbox enabled the generation of the reference orbit the Estimated Orbit, as well as the evaluation of covariance matrices and the propagation of the orbit itself.
All computations within the TUDAT environment are performed in the J2000 inertial reference frame. Therefore, the coordinate transformations described in Sections 3.6 were implemented consistently with this convention.

4.2 GNSS Signal Emulation

Skydel is a Software-Defined GNSS Simulator that uses GPU-accelerated computing to generate GNSS signals in real time. It simulates signals from constellations like GPS, Galileo, Global Navigation Satellite System (GLONASS), and BeiDou using detailed physics and environmental models. The main objective

of the simulator is to create a Radio Frequency (RF) signal identical to the "Live Sky" at the GNSS receiver's RF input connector. The figure depict the difference between the propagation of the real signal 4.1 and the simulated signal (using a Universal Software Radio Peripheral (USRP) as an example) 4.2.
Skydel, using a computer setup, generates real-time I/Q samples representing the baseband signals. These samples are transmitted over a transport link, such as Ethernet or USB, and queued in the Software Defined Radio (SDR) buffer. The SDR retrieves the samples from the buffer at a consistent rate and converts them to RF. If the SDR has multiple outputs, the signals are combined into a single RF cable. The RF signal is then attenuated before passing through a DC Block and reaching the GNSS receiver under test [19].

Figure 4.1: Propagation of the real GNSS signal from the satellite to the GNSS receiver

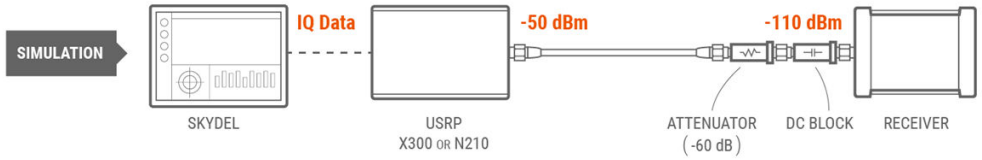

Figure 4.2: Propagation of the simulated GNSS signal from Skydel to the GNSS receiver

Hardware-In-The-Loop Simulation: Setup

The simulation was run on a TU Delft computer, on which the GPS-SDRSIM software is installed. The setup of the experiment consists of:

- **USRP SDR**: The radio used for the purpose is the Dektec DTA-2116;
- **Attenuator**: The RF signal power level output by the SDR is much stronger than the real live sky signal when it reaches the GNSS receiver's antenna. Consequently, attenuators were used between the SDR and the GNSS receiver to prevent the latter from being damaged. In particular, an

attenuation of 50 dB is advised for a receiver without Low Noise Amplifier (LNA), whereas 30 dB for non LNA receivers;

- **DC-Block**: It is a single component that prevents the DC voltage from travelling back from the GNSS receiver to the SDR. Typically, GNSS receivers will provide DC voltage (5V or 12V) to the antenna to power the antenna's amplifier. However, when using a simulator, this DC voltage is useless and could damage the SDR.
- **GNSS Receivers**: The SkyTraq S1216F8-GI3 Receiver is used as a single frequency receiver 4.3. It is a Real Time Kinematics (RTK) receiver designed to achieve centimeter-level accuracy for precision guidance and relative positioning applications[20]. For dual-frequency applications, the Septentrio AsteRx-m2 OEM Receiver is used 4.4.

Figure 4.3: SkyTraq PX1122C Single Frequency GNSS Receiver installed on its board

Figure 4.4: Septentrio AsteRx-m2 OEM Dual Frequency GNSS Receiver installed on its board

4.3 Orbits generation

Following the workflow illustrated in Figure A.1, an explanation of each step in the orbit generation pipeline is given. Each of these steps is presented in the following subsections, with attention given to the assumptions and configurations adopted in the Perturbed and Not Perturbed scenarios.
A more detailed description of the implemented codes, along with a simulation guide for reproducing the results, is provided in Appendix A.

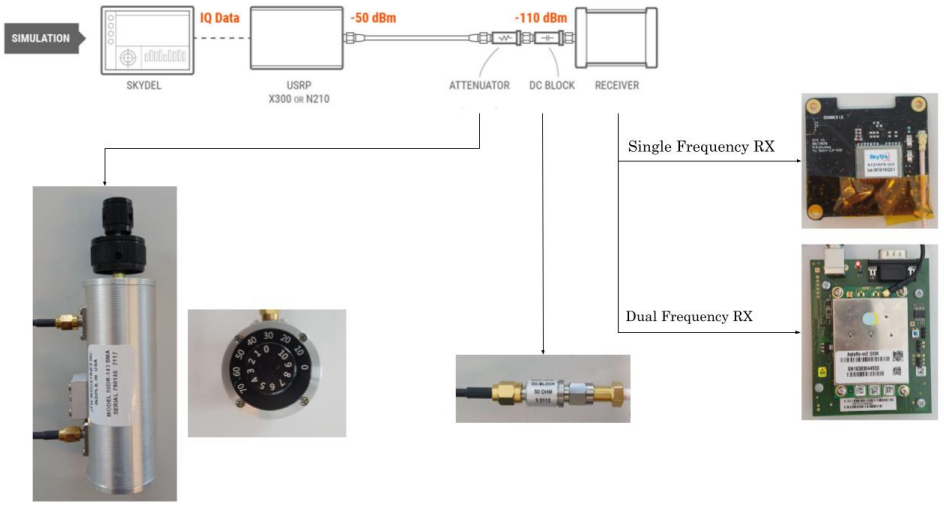

Figure 4.5: Setup Visualization

4.4 True Orbit generation

The simulation process begins with the generation of the Ground Truth Orbit. This orbit serves as a reference for subsequent estimation and propagation tasks.

The satellite's True Orbit is generated using the TUDAT simulation environment. The input includes the initial state, as defined by Keplerian elements, and a representation of the Earth's shape, along with the corresponding propagation setup.

The initial orbital state corresponds to a genericLEO orbit. This avoids special configurations, such as equatorial or polar orbits, and represents a range in which the TwinSat could potentially be placed. The initial orbital parameters selected are reported in Table 4.1.

To represent the Earth's figure accurately, an oblate spheroid is defined with

Keplerian Element	**Value**	**Unit**
Semi-major axis (a)	6878	km
Eccentricity (e)	0.00403	–
Inclination (i)	60.160	deg
Argument of periapsis (ω)	17.892	deg
Longitude of ascending node (Ω)	4.753	deg
True anomaly(ν)	61.317	deg

Table 4.1: Initial Keplerian Elements

a equatorial radius of 6 378 137 m and a flattening factor of $\frac{1}{298.257}$, accordingly to WGS84 model, as mentioned in Section 3.5.
The simulation is conducted in an ECI reference frame, with Earth as the central body and the J2000 frame as standard orientation. For the propagation setup, two scenarios are considered:

Not Perturbed Case In this configuration, only Earth's point-mass gravity is considered as the acting force. No atmospheric drag, solar radiation pressure, or higher-order gravitational effects are included. This yields a simplified, idealized orbit, useful for baseline comparisons. The orbit is propagated starting from January 14th, 2023 at 12:00:00 for the single-frequency receiver; the starting date is July 1st, 2025 at 00:00:00 for the dual-frequency receiver.

Perturbed Case In contrast, more realistic force models were added to the Perturbed Ground Truth. This involves the Earth's gravity field expanded to the fifth degree and order using spherical harmonics, atmospheric drag based on the NRLMSISE-00 model, and solar radiation pressure with Earth considered as an occulting body. The satellite is characterized with physical properties such as mass and surface area, defined to represent a TwinSat unit. These characteristics influence the perturbing forces acting on the spacecraft. The start date for this simulation is July 1st, 2025 at 00:00:00.

Effect	**Not Perturbed**	**Perturbed**
Earth Gravity	Point-mass model	Spherical harmonics (5,5)
Atmospheric Drag	Not included	NRLMSISE-00 model
Solar Radiation Pressure	Not included	Included with Earth shadowing
Satellite Mass	Not modeled	2.2 kg
Satellite Volume	Not modeled	$\frac{4 \cdot 0.3 \cdot 0.1 + 2 \cdot 0.1 \cdot 0.1}{4}$ m^2
Aerodynamic Coefficients	Not included	$C_D = 2.5$
Earth Rotation Model	IAU2000A	IAU2000A
Additional Bodies	None	Sun
Reference Frame	J2000	J2000

Table 4.2: Comparison of models used in Perturbed and Not Perturbed cases

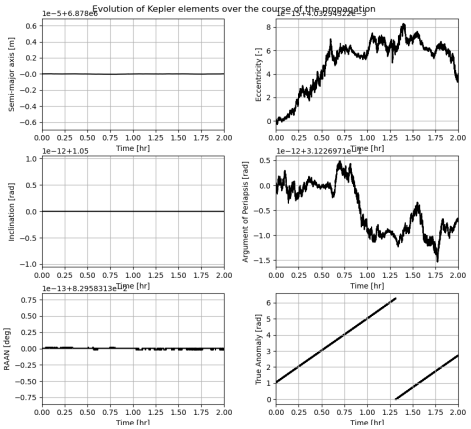

Figure 4.6: Keplerian Elements of Not Perturbed orbit

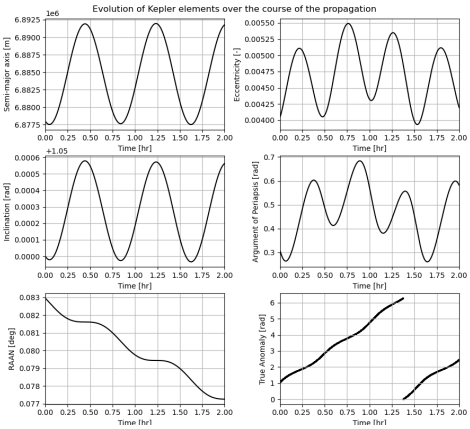

Figure 4.7: Keplerian Elements of Perturbed orbit

Figure 4.8: Keplerian Elements of True Orbit propagated for 2 hours

4.5 Measured Orbit generation

Once the Ground Truth is generated, it is imported into the Skydel GNSS simulation software, which emulates the satellite navigation signals corresponding to the specified simulation date. The GNSS receiver is configured in single- or dual-frequency mode and processes these signals to output the Measured Orbit. Throughout the playback duration, this measured trajectory closely follows the reference orbit, with deviations primarily due to measurement noise introduced by inherent limitations in the receiver. The resulting Measured Orbit represents a realistic approximation of what would be obtained during an actual on-board GNSS-based navigation scenario.

All ionospheric correction options were disabled in the Skydel environment. As ionospheric refraction at the altitude of LEO satellites can differ from ground-based GNSS observations, Skydel's built-in correction for this effect has been disabled.

In order to assess the impact of the simulation on GNSS signals effectively, the Measured Orbit interval was selected to last for at least one full orbital period.

4.6 Estimated Orbit Generation

The Orbit Estimation is performed using the TUDAT environment, which provides the necessary tools for the process. The orbit prediction within TUDAT

is performed using a Runge–Kutta–Fehlberg 7(8) integrator (RKF78), with a fixed time step of 1 second.
The key idea is to treat the Measured Orbit, obtained as described in Section 4.5, as a set of observations. These observations are then used to compute the orbit that best fits the ground truth over the playback period.
This method reflects what could potentially be implemented on-board the satellite itself: after gathering GNSS measurements, an on-board estimation code could be executed to define the satellite's orbit position.
The estimation setup can follow two different scenarios, depending on the configuration of the True Orbit used as reference. These configurations correspond to the force models defined in Table 4.2.

Not Perturbed Case In this configuration, the estimation is performed using the same simplified force model applied to the "Not Perturbed Orbit" in Table 4.2. The resulting Estimated Orbit reflects an idealized, unperturbed trajectory.

Perturbed Case In this configuration, estimation uses the full force model described in the "Perturbed Orbit" Column of Table 4.2. This model includes atmospheric drag, solar radiation pressure and higher-order gravitational terms. This provides a more realistic estimation scenario that is closer to actual orbital dynamics.

4.7 Propagated Orbit Generation

Once the Estimated Orbit has been computed, its final Keplerian state is taken as the initial condition for generating the Propagated Orbit. The aim is to assess how the quality of the estimation influences the subsequent orbit propagation. From an operational perspective, this reflects a realistic on-board scenario where, after orbit determination, the satellite predicts its future position based on the current state.
The propagation is again carried out using the TUDAT environment. Depending on the configuration of the True Orbit, either the "Not Perturbed" or "Perturbed" force models, defined in Table 4.2 are applied.

Chapter 5

GNSS-Based Orbit Determination

Once the process described in Chapter 4 is complete, the analysis on Measuremed and Estimated Orbits can be assessed.
This chapter evaluates the results derived from four simulation configurations: single- and dual-frequency GNSS receivers, each tested under both Perturbed and Not Perturbed conditions. Three orbits are involved in these comparisons: the True Orbit, the Measured Orbit and the Estimated Orbit. In the figures presented, a colour code is adopted for clarity: the black lines are referred to the Reference Orbit and its associated values, the blue lines to the Measured Orbit, and the red lines to the Estimated Orbit.
The duration of the Measured Orbit is set to one full orbital period; therefore, the Estimated Orbit is also defined over the same time interval.

5.1 Not Perturbed Case

5.1.1 Results from Single Frequency Measurements

Plotting the three orbits in either the ECEF or ECI frames does not provide enough details to assess the differences amongst them. Considering the accuracy that the involved receivers are able to provide, these differences were expected to be on the order of metres. Therefore, the differences were not clearly visible in the full orbit plots. For this reason, the ECEF and ECI orbit comparison

plots will not be reported for the following cases, but the differences between the three orbits are reported instead. Across all scenarios, the differences between

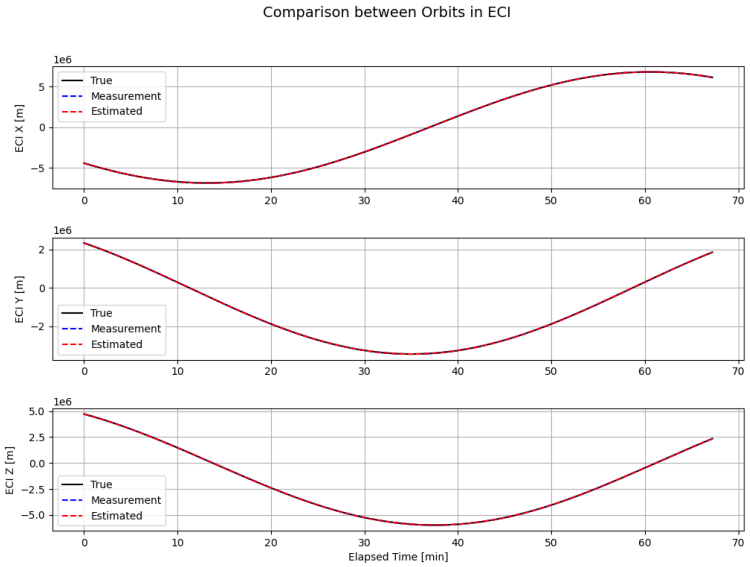

Figure 5.1: Comparison Orbits in ECI - Single Frequency Not Perturbed Case

the three orbits show consistent patterns in both the ECEF and ECI reference frames. For clarity and graphical representation, only the differences in the ECI frame will be reported from now on: the trend shown, indeed, is almost the same between the two reference frames. Latitude and longitude are displayed at the bottom of the graph to provide an indication of the satellite's position along its orbit.
The first noticeable feature in Figure 5.2 is the noise observed in the "True–Measured" difference. This noise is introduced by the GNSS receiver itself and reflects a limitation of the hardware, even under ideal Not Perturbed conditions.
The red line represents the "True-Estimated" Orbits difference, and it demonstrates how the estimation process, described in the previous chapter, is able to determine the position of the satellite, also from noisy measurements. This behaviour is consistently visible across all Cartesian components.

However, to better evaluate the quality of these measurements and their impact on OD, it is more straightforward to analyse these differences in the RSW frame. The RSW difference plots show how the measurement and estimation errors are projected along the Radial, Along-track, and Cross-track axes 5.5.
Among these, the Radial (R) component exhibits the largest errors. This is to be expected, as GNSS receivers are sensitive to radial position errors. GNSS sig-

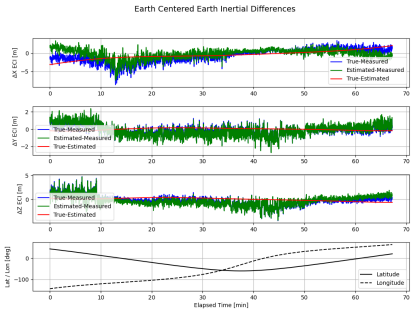

Figure 5.2: ECI Differences Plots

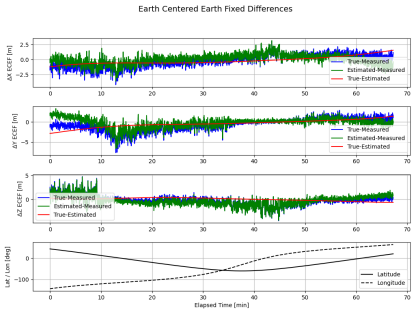

Figure 5.3: ECEF Differences Plots

Figure 5.4: ECI and ECEF Differences for Single Frequency Not Perturbed Case

nals, indeed, are mostly received from satellites near the zenith direction, which makes radial errors easily observable, but also more subject to atmospheric effects [13]. However, the maximum radial error remains below 8 metres in this Not Perturbed case, which is consistent with the expected nominal accuracy range of a low-cost, single-frequency GNSS receiver [21]. Of particular interest is the time interval around 10 minutes after the beginning of the simulation. This corresponds to the satellite's passage over the equator, as shown in the latitude and longitude subplot. The equatorial region is well known for its strong ionospheric activity, which has an impact on GNSS signals, particularly in the case of single-frequency.
The Along-track (S) component follows the trend of the True Orbit more closely. This indicates that the Measured and the Estimated Orbit orbital speed or timing do not deviate significantly from the Ground Truth, so the satellite maintains the expected trajectory without any significant delay or advance.
Finally, the Cross-Track (W) component shows the smallest variation, remaining consistently within the range of $\pm 1\ m$. This is because Cross-Track deviations correspond to out-of-plane motion, which is minimal since GNSS measurement geometry is generally less sensitive to errors in this direction.

To quantify the measurements and OD performance, the RMSE was computed starting from RSW frame differences. Both the instantaneous and overall RMSE values are reported in Figure 5.6: the former captures the evolution of the error over time and reflects the trends visible in Figures 5.4 and 5.5, while the latter provides a scalar metric over the entire orbit.
The instantaneous RMSE curves are characterised by the same noise described

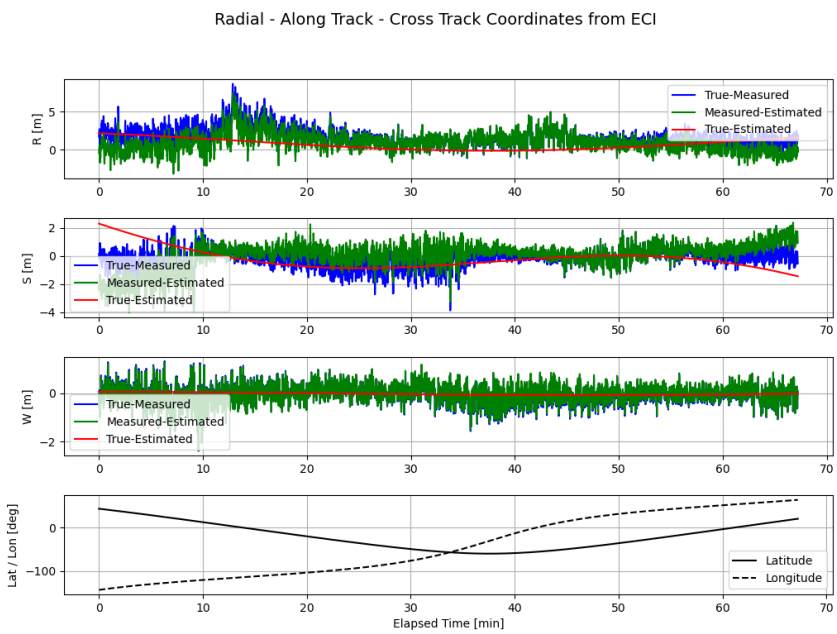

Figure 5.5: RSW Differences Plots for Single Frequency Not Perturbed Case

earlier for the "True–Measured" differences, caused by receiver limitations. In contrast, the "Estimated–True" RMSE shows a much smoother curve, as it reflects the result of the estimation process.

The total RMSE, in Figure 5.24a, for the RMSE "True–Measured" Overall is the largest, with a value of 2.225 m. This error, however, is compensated by the estimation algorithm, which reduces the RMSE "Estimated–True" Overall to 1.856 m. This confirms the capability of the estimation process to compensate for the measurement noise and accurately determine the orbit.

A more detailed analysis is provided by considering the projection of the RMSE along the RSW components 5.6b, 5.6c, 5.6d. The Radial (R) component exhibits the highest RMSE, confirming that this direction is the most affected by measurement errors. This is expected, as GNSS receivers are most sensitive to radial errors due to their signal geometry.

The Cross-Track (W) component shows the smallest RMSE values. The RMSE "Estimated–True" Overall is only 0.050 m, indicating that the estimation process is particularly effective at correcting out-of-plane deviations. The RMSE "True–Measured" Overall for the Cross Track (W) component reach a valued of 0.395 m, indicating that the GNSS measurements provide good accuracy even in the Cross-Track direction.

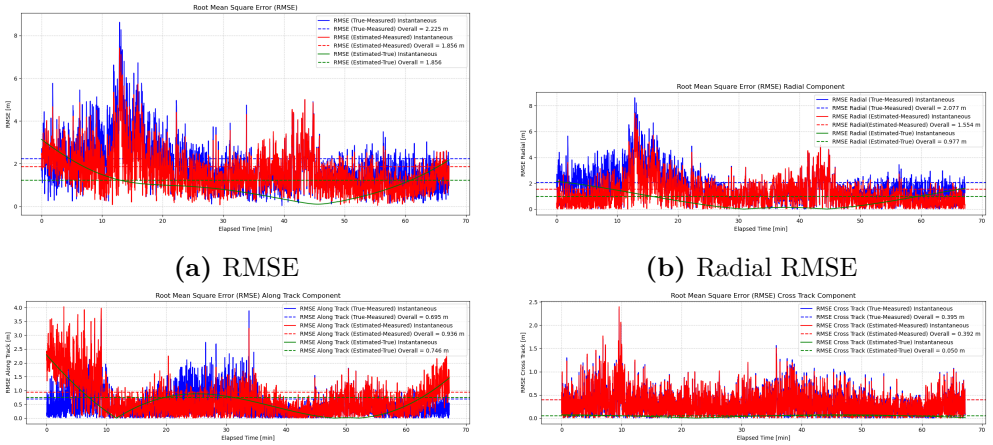

(a) RMSE **(b)** Radial RMSE

(c) Along-Track RMSE **(d)** Cross-Track RMSE

Figure 5.6: RMSE for the Single Frequency Not Perturbed Case

Particular focus must be given to the estimation process. One way to assess its reliability is to analyse specific plots. The first plot to consider is the Observation Residuals per Iteration 5.7. As shown in Table 5.1, initially the residuals are relatively large and show a systematic component, due to the initial guess of the model being far from the true solution.
However, after the first iteration, these residuals decrease significantly, indicating that the model is starting to converge and fit the measurements. From the third to the seventh iteration, the residuals remain stationary with only minor variations. The associated corrections become negligible. Overall, the estimation process is characterised by fast convergence, with the majority of adjustments occurring within the first iteration. From the third iteration onwards, corrections are minimal, suggesting that the model reached a satisfactory level of accuracy by the second iteration. The final residual is equal to 1.072 m.

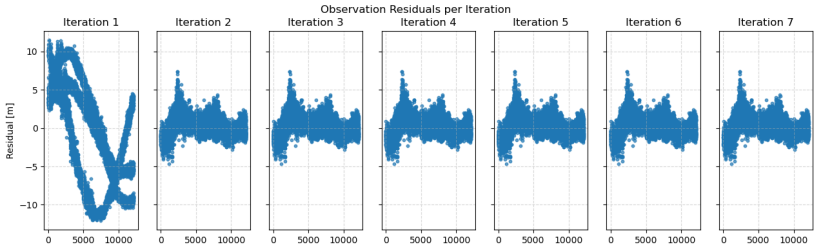

Figure 5.7: Observation Residuals per Iteration for Single Frequency Not Perturbed Case

Iteration	Residual	Parameter updates					
		a	e	i	Ω	ω	ν
1	6.447	1.166e+01	4.275e+00	5.601e+00	-1.142e-02	4.714e-03	9.855e-03
2	1.072	-4.263e-06	-4.897e-06	-7.881e-06	2.192e-08	5.649e-09	6.561e-09
3	1.072	-8.600e-09	7.494e-09	-1.086e-08	3.341e-12	5.959e-12	5.731e-12
4	1.072	1.153e-08	-6.396e-09	-9.595e-09	-1.777e-11	8.486e-12	1.685e-11
5	1.072	-6.107e-09	4.097e-09	6.079e-09	1.101e-11	-2.155e-12	-8.660e-12
6	1.072	-1.887e-09	-1.186e-10	-2.062e-09	3.438e-13	1.267e-12	-5.030e-13
7	1.072	-4.056e-09	-1.194e-09	3.628e-09	7.305e-12	-5.527e-13	-3.032e-12

Table 5.1: Residuals for Single Frequency Not Perturbed Case

This behaviour is further confirmed by the residuals histogram at the final iteration 5.8. The horizontal axis shows residual range errors in m, ranging from approximately -4 to 8 m, and the vertical axis shows the number of occurrences.
The histogram exhibits a Gaussian-like distribution centered around zero, indicating that most residual errors are small and well-distributed near the true values. However, some residuals extend towards 8 m, corresponding to the maximum deviations observed in the Radial direction.

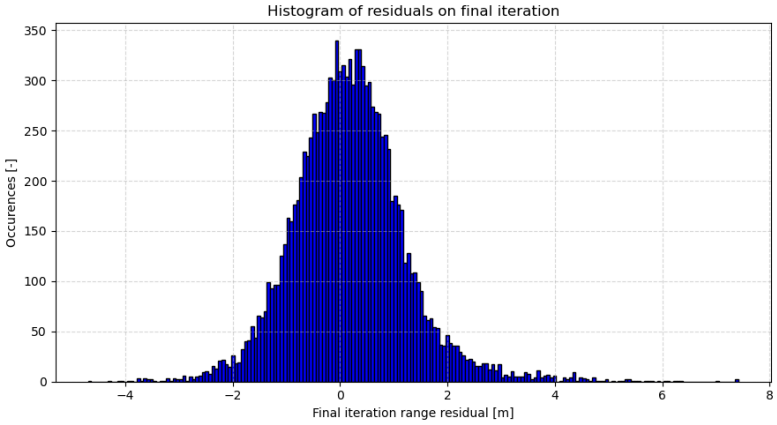

Figure 5.8: Histogram of Residuals on Final Iterations for Single Frequency Not Perturbed Case

A more intuitive way to assess the accuracy of the estimation process relative to the measurements is through the visualization of Covariance and Formal Error ellipsoids, derived from the residuals. The 3D ellipsoid represents the spatial confidence region where the actual orbit is. The projections on the planes show the 2D confidence ellipses, helping to visualize how errors distribute along each axis.
As the estimation process is carried out in the J2000 reference frame, these

ellipsoids reflect the residuals in the ECI components. The shape of the ellipsoids indicate that the estimation solution is more reliable in the Z-axis and Y-axis directions. Instead, the X-axis shows the greatest error, in both the empirical covariance and the formal error model. This aligns with the observations made in Figure 5.2, in which the X component exhibits the most significant differences. This behaviour along the X-axis can be attributed to the Radial direction, which reinforces the known limitations of GNSS accuracy along this component.
In addition, the nearly diagonal structure of the Covariance Matrix confirms the lack of coupling between different state components, reflecting a numerically stable estimation process. The visual confirmation of these aspects through the ellipsoid confirms the reliability of the process. In the 2D projections of the ellipsoid, the elongation along the X-direction remains evident.
The Formal Errors reported, instead, display values on the order of 4.5 *cm* in X, 2.2 *cm* in Y, and 2.0 *cm* in Z, confirming the reliability of the OD.

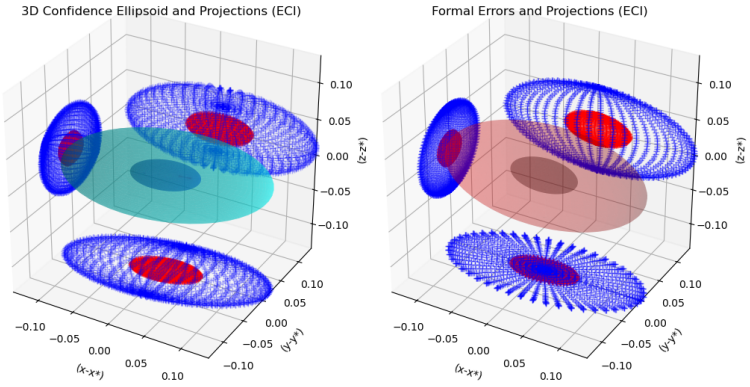

Figure 5.9: Confidence Ellipsoid for Single Frequency Not Perturbed Case

Component	Value [m^2]
Cov(X,X)	2.077e-03
Cov(X,Y)	2.119e-04
Cov(X,Z)	1.393e-04
Cov(Y,Y)	4.861e-04
Cov(Y,Z)	-4.292e-05
Cov(Z,Z)	3.985e-04

Table 5.2: Covariance Matrix

Component	Value [m]
X	4.557e-02
Y	2.205e-02
Z	1.996e-02

Table 5.3: Formal Errors

5.1.2 Results from Dual Frequency Measurements

By analyzing the dual-frequency results, it is immediate to notice that the differences in both the ECI (5.10) and RSW (5.11) reference frames are significantly reduced with respect to the single-frequency case, reaching values within the range of $\pm$ 1 m in the worst case. The improved accuracy is due to the dual-frequency receiver's ability to correct for ionospheric delays, better explained in Section 5.3. Nevertheless, the measurement noise is persistent.

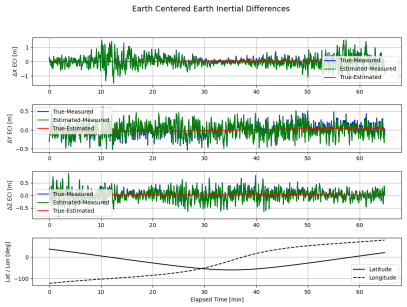

Figure 5.10: ECI Differences for Dual Frequency Not Perturbed Case

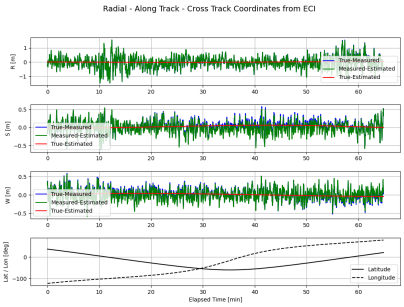

Figure 5.11: RSW Differences for Dual Frequency Not Perturbed Case

More accurate measurements lead to more accurate ODs, and this is reflected in the RMSE plots (5.12). The overall RMSE values are lower compared to the single-frequency case, but this improvement is more straightforward when considering the instantaneous RMSE trends. In particular, the "True-Measured" RMSE drops to 0.451 m against 2.225 m for the previous case, confirming the precision of the dual-frequency receiver. Notably, the "Estimated-True" RMSE is also 0.451 m, indicating that the estimation process is mantaining the measurement accuracy.
Focusing on the Radial component (R) 5.12b, the improvement is even more noticeable: the RMSE "True-Measured" Overall is 0.390 m, while the RMSE "Estimated-True" Overall is reduced to just 0.019 m. This demonstrates that the estimation process is preserving but also refining the measurements, also along the most error-prone direction.

The accuracy of the OD process is further confirmed by analyzing the residual plots 5.13 and convergence results 5.14. The observation residuals lie within $\pm$ 1 m, as well as the Gaussian error distribution, indicating a good fit between the measurements and the estimated trajectory. Notably, the residuals con-

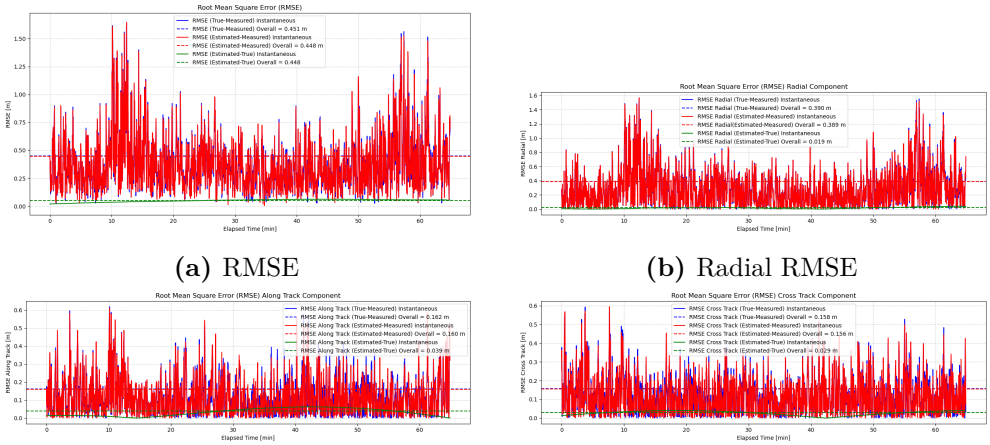

(a) RMSE **(b)** Radial RMSE

(c) Along-Track RMSE **(d)** Cross-Track RMSE

Figure 5.12: RMSE for the Dual Frequency Not Perturbed Case

verge rapidly, stabilizing after two iterations, with a final residual of 0.259 m, significantly lower than the 1.072 m obtained in the single-frequency case. This highlights the improvement in estimation accuracy enabled by dual-frequency GNSS observations.

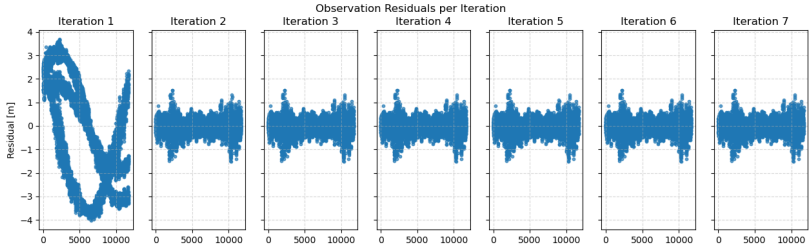

Figure 5.13: Observation Residuals per Iteration for the Dual Frequency Not Perturbed Case

Iteration	Residual	a	e	i	Ω	ω	ν
1	2.144	2.38695	1.52896	2.28452	-3.069e-03	1.165e-03	2.383e-03
2	0.259	-7.665e-07	-4.508e-07	-6.815e-07	2.534e-09	2.506e-10	6.792e-11
3	0.259	2.096e-08	-4.670e-10	-1.944e-08	-2.953e-11	4.218e-12	2.794e-11
4	0.259	-3.311e-09	3.427e-09	2.681e-10	4.051e-12	-1.671e-12	-2.975e-12
5	0.259	4.115e-09	-2.893e-09	-1.705e-09	-4.672e-12	5.288e-12	2.358e-12
6	0.259	-6.751e-09	3.813e-10	3.937e-09	1.092e-11	-2.215e-12	-4.580e-12
7	0.259	6.665e-10	1.497e-09	-9.969e-10	2.295e-13	-2.178e-12	9.197e-13

Table 5.4: Residuals for Dual Frequency Not Perturbed Case

In addition to the residual analysis, the Covariance Matrix and Formal Errors

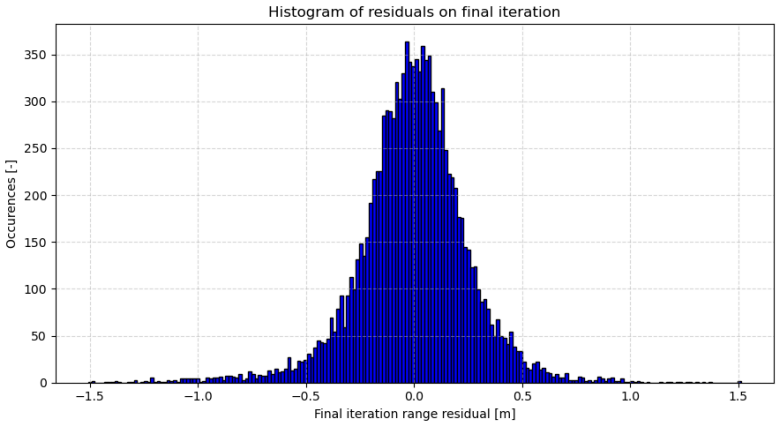

Figure 5.14: Histogram of Residuals on Final Iterations or the Dual Frequency Not Perturbed Case

are reported. Although the final residual is lower with respect to the previous case, the Formal Errors (4.53 *cm* in X, 2.31 *cm* in Y, and 2.19 *cm* in Z) are very similar to those obtained in the single-frequency case. The position Covariance Matrix confirms this trend, showing minimal changes in the X component and slightly increased variance in Y and Z. This suggests that while dual-frequency GNSS enhances the measurement quality and reduces residuals, it does not affect the estimation process.

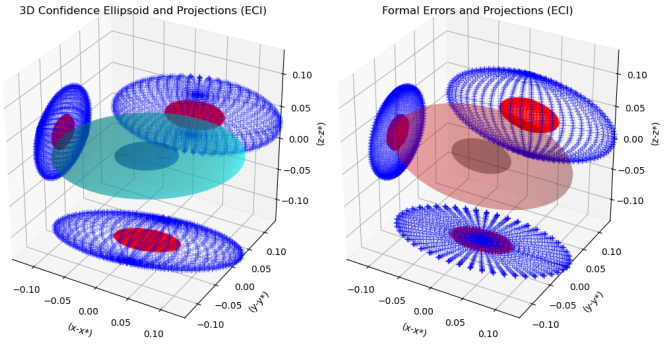

Figure 5.15: Confidence Ellipsoid for Dual Frequency Not Perturbed Case

Component	Value [m^2]
Cov(X,X)	2.051e-03
Cov(X,Y)	3.216e-04
Cov(X,Z)	3.339e-04
Cov(Y,Y)	5.328e-04
Cov(Y,Z)	1.950e-05
Cov(Z,Z)	4.805e-04

Table 5.5: Covariance Matrix

Component	Value [m]
X	4.529e-02
Y	2.308e-02
Z	2.192e-02

Table 5.6: Formal Errors

5.1.3 Not Perturbed Case Results

This first analysis of the Not Perturbed Case gives the basis for confirming that the dual-frequency receiver enhances the measurements quality and compensate for ionospheric biases. Consequently, the observations are less influenced by measurement errors in the dual-frequency scenario. This can be seen by comparing position errors with respect to the reference trajectory. In the case of the dual-frequency receiver, these errors amount to around 1 meter across all ECI and RSW components. This conclusion is further supported by the final residuals obtained after the OD process, which amount to 1.072 m in the single-frequency case compared to 0.259 m for the dual-frequency case.
By contrast, single-frequency receiver measurements exhibit larger position errors, particularly in the radial direction, reaching 7 m. Nevertheless, the estimation process can still provide reliable results, effectively compensating for ionospheric effects and achieving a total RMSE of 2.225 m.

5.2 Perturbed Case

The Not Perturbed analysis served as the basis for the OD process under Perturbed conditions. As previously mentioned, the same set of perturbations applied to the True Orbit is also applied in this case, ensuring consistency in the simulated environment 4.2. As in the previous scenario, the ionospheric correction is disabled in Skydel.

5.2.1 Results from Single Frequency Measurements

The Single Frequency measurements and the determined orbit for the Perturbed case exhibit a particular behavior. In the ECI frame (Figure 5.16),

measurement peaks appear in the X, Y and Z components approximately after 10 minutes from the beginning of the simulation. This effect is enhanced when considering the RSW components (Figure 5.17): the Radial component shows the most significant deviation, reaching a value of approximately 25 m. In comparison, measurement reached 8 m in the single-frequency Not Perturbed case (Figure 5.1), still occurring around 10 minutes after the beginning of the simulation. Around this time, indeed, in both scenarios, the satellite crosses the equator, where the latitude is zero, a region strongly influenced by the ionosphere, causing signal disturbances [13]. In the Perturbed case, this effect is even more pronounced. This behaviour is also clear when analysing the

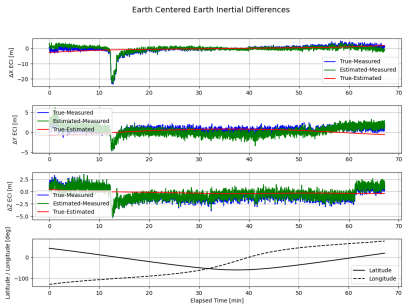

Figure 5.16: ECI Differences for Single Frequency Perturbed Case

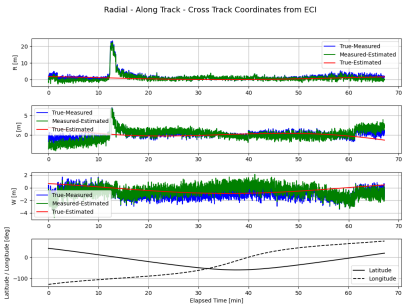

Figure 5.17: RSW Differences for Single Frequency Perturbed Case

RMSE components (Figure 5.18) and is related to the nature of the GNSS measurements obtained by the single-frequency receiver for the Perturbed case. When perturbations are added, the Measured Orbit is more subjected to the effect of the ionosphere, which creates greater deviations.
However, considering the "Estimated–True" differences shown in Figures 5.16 and 5.17, the Estimated Orbit effectively filters out these deviations, demonstrating the robustness of the estimation process.
When focusing on the measurements, the Radial RMSE remains the main contributor to the total RMSE.

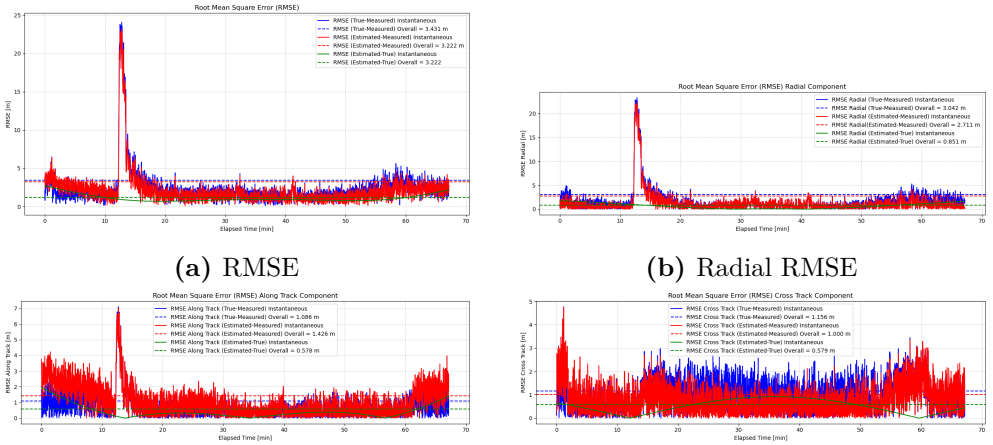

(a) RMSE **(b)** Radial RMSE

(c) Along-Track RMSE **(d)** Cross-Track RMSE

Figure 5.18: RMSE for the Single Frequency Perturbed Case

These peaks are also evident in the residuals (Figure 5.19): although the residuals decrease after the first iterations, a peak of nearly 25 m is observed. Similarly, the residuals histogram (Figure 5.20) maintains a Gaussian-like distribution centered around zero, with some residual values extending between 5 and 25 m. In both cases, this trend is to be attributed to the measurement spikes.

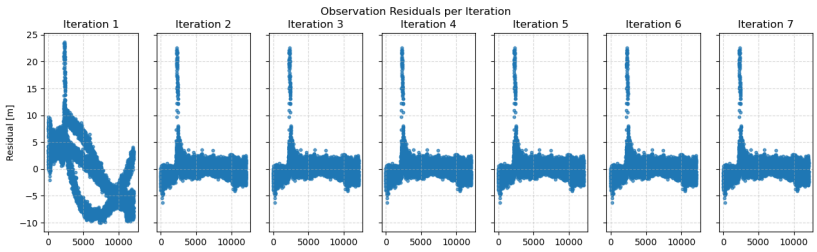

Figure 5.19: Observation Residuals per Iteration

Comparing the final residuals of the Perturbed and Not Perturbed cases shows that the Not Perturbed case has a residual of 1.072 m, compared to 1.860 m in the Perturbed case.

This suggests that the estimation process remains effective in the Perturbed scenario, despite the presence of peaks , although performing better in the Not Perturbed scenario. Even though the residual distribution is not uniform due to the presence of peaks, the final error ellipsoids (Figure 5.21) are more

Iteration	Residual	a	e	i	Ω	ω	ν
1	5.531	9.345e+00	3.941e+00	4.200e+00	-9.284e-03	3.239e-03	8.395e-03
2	1.860	-2.572e-06	-3.017e-06	-5.063e-06	1.420e-08	3.856e-09	4.582e-09
3	1.860	5.276e-09	-6.064e-11	-9.222e-09	5.110e-12	1.584e-12	2.687e-12
4	1.860	2.060e-08	-1.198e-08	-8.314e-09	-3.675e-11	7.916e-12	1.519e-11
5	1.860	-1.117e-08	3.424e-09	7.531e-09	1.882e-11	-1.580e-12	-7.179e-12
6	1.860	2.059e-09	-3.380e-11	-1.781e-09	-5.548e-13	-3.255e-13	-2.225e-12
7	1.860	-5.538e-10	3.334e-10	2.564e-09	3.310e-12	4.365e-13	-1.913e-12

Table 5.7: Residuals for Single Frequency Perturbed Case

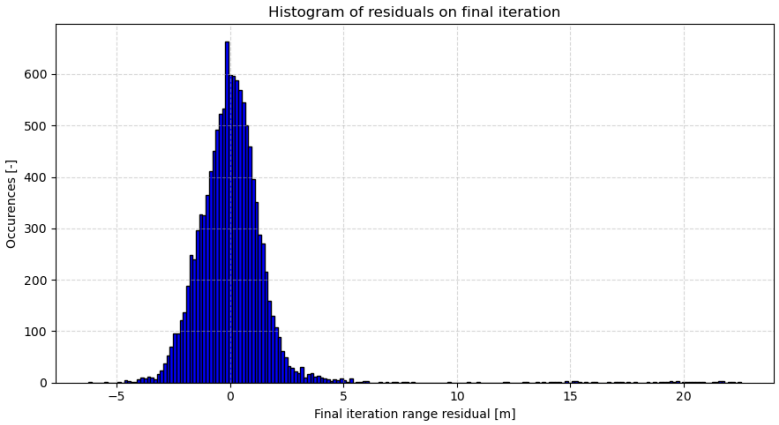

Figure 5.20: Histogram of Residuals on Final Iterations

elongated along the X component, as in previous cases. This is consistent with the Radial direction and suggests that, even in the Perturbed case, the axis that contributes the most to the error is the Radial component. The covariance values in the Perturbed case are very similar to those of the Not Perturbed cases, especially in the X component. This suggests that the internal estimation consistency remains high, despite perturbations addition.

Component	Value [m^2]
Cov(X,X)	2.079e-03
Cov(X,Y)	2.119e-04
Cov(X,Z)	1.418e-04
Cov(Y,Y)	4.843e-04
Cov(Y,Z)	-4.010e-05
Cov(Z,Z)	3.994e-04

Table 5.8: Covariance Matrix

Component	Value [m]
X	4.559e-02
Y	2.201e-02
Z	1.998e-02

Table 5.9: Formal Errors

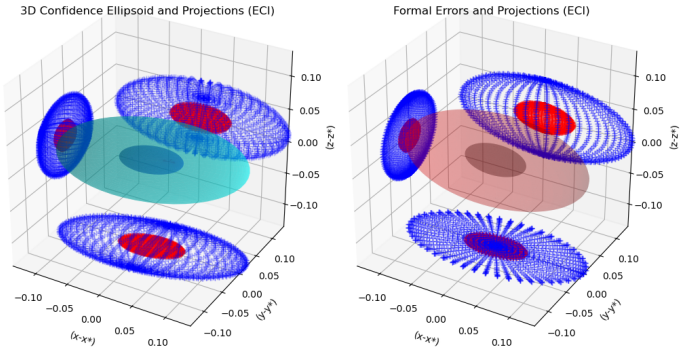

Figure 5.21: Confidence Ellipsoid for Single Frequency Perturbed Case

5.2.2 Results from Dual Frequency Measurements

As in the Dual Frequency Not Perturbed case, the differences between the three orbits in the ECI (5.22) and RSW (5.23) reference frames decrease significantly with respect to the single-frequency scenario, especially within the time interval in which peaks were previously observed. These deviations are no longer shown in the dual-frequency case due to the ionospheric error mitigation provided by dual-frequency measurements 5.3.

When comparing the dual-frequency Perturbed (5.11) and Not Perturbed (5.23) cases, the main differences are observed along the X-axis of the ECI reference frame and the Radial direction of the RSW frame. In these components, the range of measurement differences increases from approximately $\pm$ 1 m in the Not Perturbed case to $\pm$ 2 m in the Perturbed scenario.

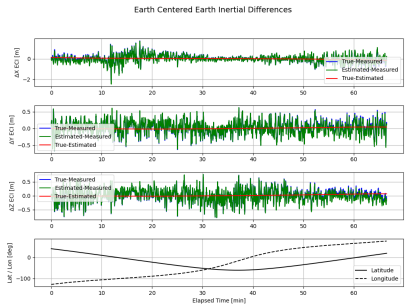

Figure 5.22: ECI Differences for Dual Frequency Perturbed Case

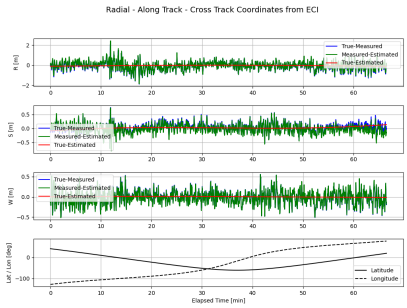

Figure 5.23: RSW Differences for Dual Frequency Perturbed Case

Despite this small difference, the Measured Orbit still closely follows the True Orbit, and the Estimated Orbit maintains high accuracy. As a result, the

Estimated Orbit is computed achieving an overall RMSE of 0.468 m. When compared to the Not Perturbed scenario (5.18a), where the RMSE was 0.451 m, the difference is minimal, highlighting the robustness of the estimation process. This small difference can be observed again by comparing the final residuals

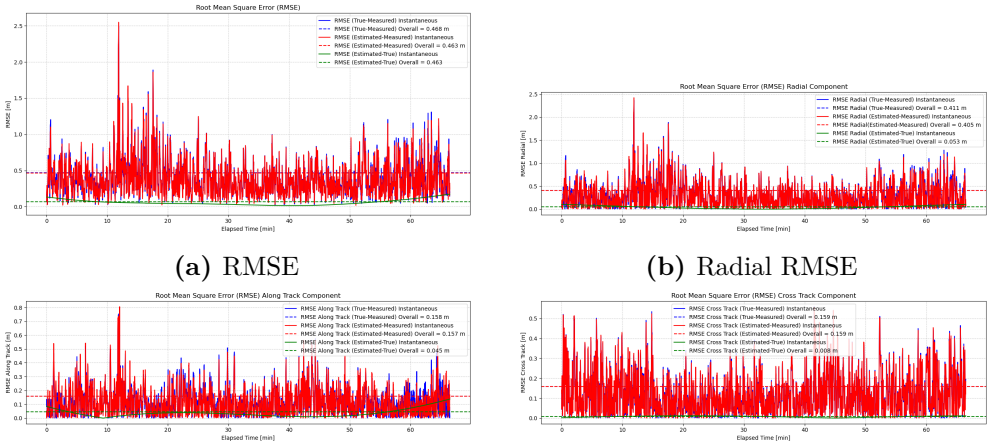

(a) RMSE **(b)** Radial RMSE

(c) Along-Track RMSE **(d)** Cross-Track RMSE

Figure 5.24: RMSE for Dual Frequency Perturbed Case

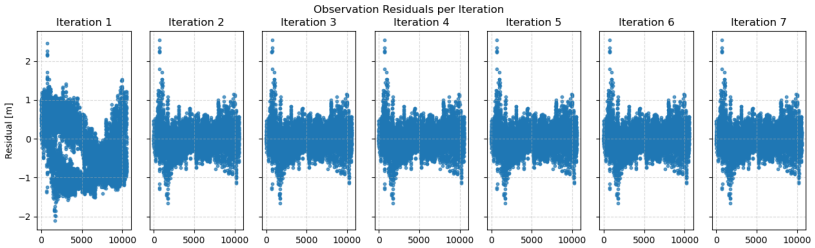

Figure 5.25: Observation Residuals per Iteration

in the double-frequency cases: 0.267 m for the Perturbed case (5.25) and 0.259 m for the Not Perturbed case (5.13).

However, it is even more interesting to compare the final residual 0.267 m of the Perturbed dual-frequency case with 1.860 m of the Perturbed single-frequency case. Although the two Perturbed cases have similar dynamic conditions, the difference in the residuals highlights how the use of dual-frequency, thanks to more accurate measurements, allows for a more precise orbital determination. This observation is consistent with what emerged in the Not Perturbed case as well.

Iteration	Residual	a	e	i	Ω	ω	ν
1	0.703	1.444e-01	5.259e-01	8.505e-01	-9.066e-04	1.422e-04	3.696e-04
2	0.268	-6.452e-08	-4.801e-08	-4.741e-08	2.629e-10	4.647e-11	3.092e-11
3	0.268	3.321e-09	5.107e-09	-1.328e-08	-2.539e-11	7.751e-13	1.377e-11
4	0.268	-6.356e-09	-4.049e-09	7.414e-09	6.141e-12	3.433e-12	-8.570e-12
5	0.268	-4.565e-09	1.351e-09	-5.231e-10	8.501e-12	-2.112e-12	4.169e-12
6	0.268	2.944e-09	-7.444e-10	3.818e-10	-2.469e-12	6.224e-13	-3.012e-12
7	0.268	-1.725e-09	3.274e-11	-1.355e-09	1.223e-12	7.280e-13	2.339e-12

Table 5.10: Residuals for Dual Frequency Perturbed Case

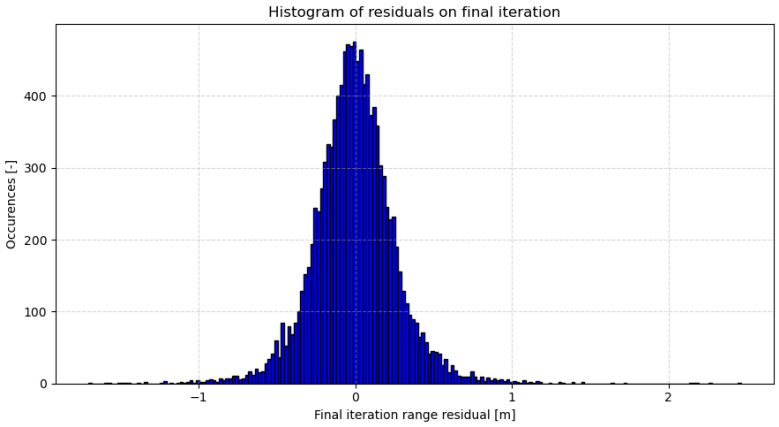

Figure 5.26: Histogram of Residuals on Final Iterations

Formal Errors are again very consistent across all cases, maintaining estimator's internal consistency.

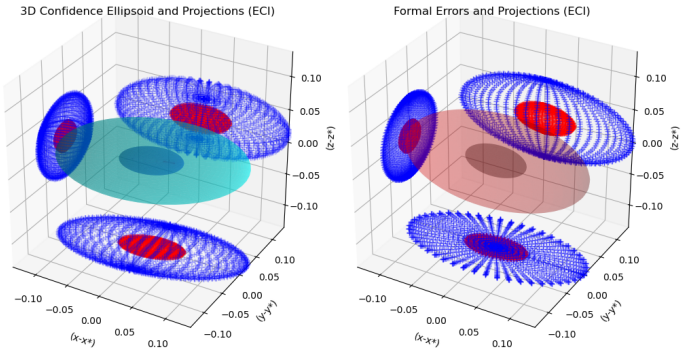

Figure 5.27: Confidence Ellipsoid for Dual Frequency Perturbed Case

Component	Value [m^2]
Cov(X,X)	2.078e-03
Cov(X,Y)	2.417e-04
Cov(X,Z)	1.941e-04
Cov(Y,Y)	4.951e-04
Cov(Y,Z)	-2.618e-05
Cov(Z,Z)	4.165e-04

Table 5.11: Covariance Matrix

Component	Value [m]
X	4.559e-02
Y	2.225e-02
Z	2.041e-02

Table 5.12: Formal Errors

5.2.3 Perturbed Case Results

The OD process demonstrates a dependence on the inclusion of perturbation models. In particular, when the Spherical Armonics for the Earth Gravity is not added, the OD algorithm fails to correctly estimate the orbital parameters. This provides specific insights into the role that this disturbance plays within the estimation process.

Consistent with the previous case, the dual-frequency receiver is able to mitigate the ionospheric bias, reducing the peak Radial error from approximately 25 m in the single-frequency solution to about 2 m. The final residuals further confirm this trend: the dual-frequency solution achieves a residual of 0.267 m, against the 1.86 m obtained with the single-frequency receiver.

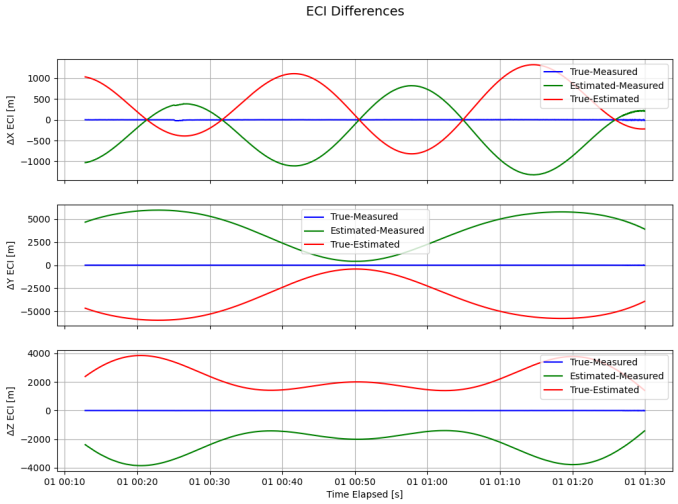

Figure 5.28: Perturbed Orbit Determination withouth Spherical Armonics

5.3 Ionospheric Correction

As discussed throughout the analysis, the peaks observed in the single-frequency scenario are caused by the ionosphere. This can be corroborated by referring to ionospheric maps, which provide information on the TEC.
Focusing specifically on the single-frequency measurements - Not Perturbed case, a zoomed-in view of the RSW plot allows for a more detailed analysis of the region of interest. This region corresponds to the satellite passing over the equator, around 10 minutes after the simulation begins. At the recorded

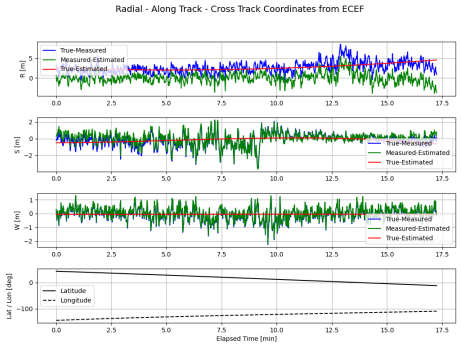

Figure 5.29: Zoom of the Single-Frequency Not Perturbed Case

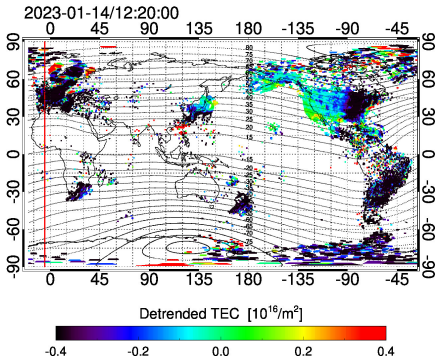

Figure 5.30: Ionosphere Map

peaks, the latitude is close to zero and the longitude is around -100 *deg*, in the equatorial Pacific Ocean, southwest of Mexico. On the map 5.30, this area actually shows a high concentration of Total Electron Content, confirming the influence of the ionosphere observed in the data.
Similar behaviour is observed in the Single-Frequency Measurements Perturbed Case. As can be seen in the zoomed-in plot, the peak error exceeds 20 m. Referring to the corresponding ionosphere map, it can be seen once again that there is a region of high Total Electron Content around latitude 0 *deg* and longitude -100 *deg*. Note that the two orbits were simulated on different dates. This confirms the significant ionospheric activity affecting the measurements in this area. However, this behavior is not observed in the dual-frequency measurements. Since the dual-frequency receiver operates on two frequencies, it can estimate and correct for ionospheric biases. In contrast, the single-frequency receiver lacks this capability, reason why significant error deviations appear in both the Not Perturbed and Perturbed cases.

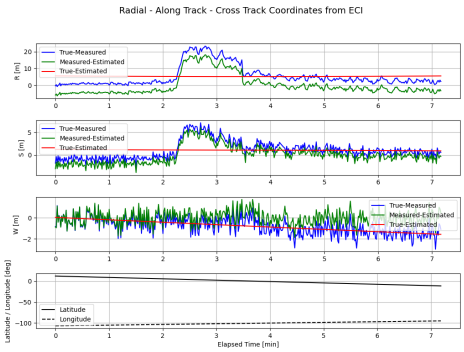

Figure 5.31: Zoom of the Single-Frequency Perturbed Case

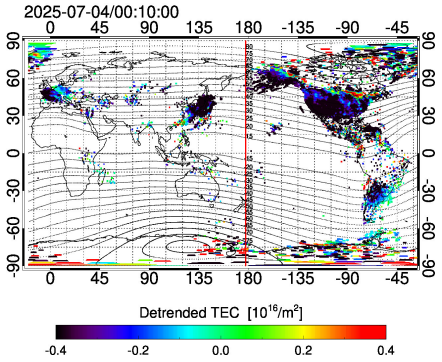

Figure 5.32: Ionosphere Map

5.4 Orbit Determination Results

The use of low-cost GNSS receivers has enabled the on-board orbit determination for small satellites to be achieved with accuracy (mean) and precision (standard deviation) of less than 1 m.

In the single-frequency case, these values are below 1 m, indicating robust performance, while the standard deviations remain below 2 m. There are no systematic errors observed, and the values are marginally higher in the Not Perturbed scenario.

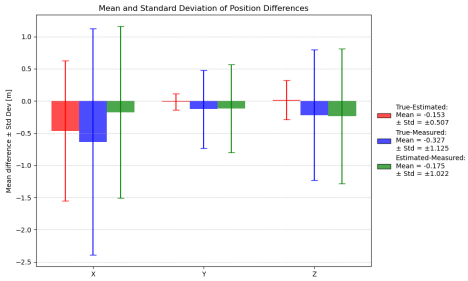

Figure 5.33: Not Perturbed Case

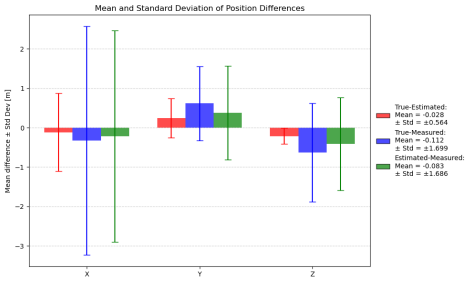

Figure 5.34: Perturbed Case

Figure 5.35: Mean and Std for the Single Frequency Case

When analysing the dual-frequency case, both the mean error and standard deviation are found to be lower in comparison to the single-frequency case, confirming its enhanced performance. The mean error remains within 23 cm, with a standard deviation of less than 0.257 m. In addition, there are no systematic errors, and the results are marginally superior in the 'Not Perturbed' condition, as predicted.

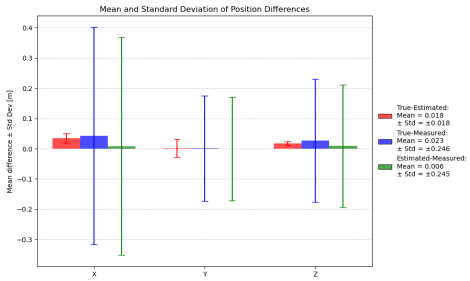

Figure 5.36: Not Perturbed Case

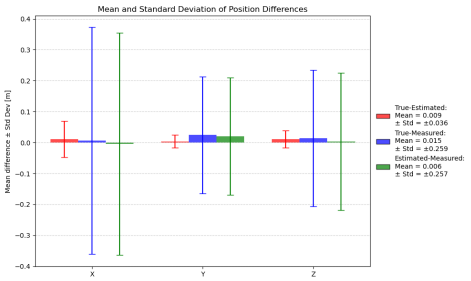

Figure 5.37: Perturbed Case

Figure 5.38: Mean and Std for the Dual Frequency Case

A further finding that emerged from the graphs is that, in all the scenarios considered, the Radial component has the greatest error. This result is consistent with the expected behaviour of the receiver, which shows greater sensitivity in this direction. However, it is important to emphasise that the error recorded remains in the order of a few metres.

Since no ionospheric correction is applied to the single-frequency receiver, a bias is registered in the radial component as a result of ionospheric refraction. This bias is caused by the ionospheric effect. The dual-frequency, instead, does not exhibit the same, as it effectively mitigates ionospheric biases.

Component	**Not Perturbed**		**Perturbed**	
	Single Frequency	Dual Frequency	Single Frequency	Dual Frequency
R [m]	1.613	0.038	1.616	-0.104
S [m]	-1.455	0.001	-1.405	0.138
W [m]	-0.011	-0.040	0.438	-0.011

Table 5.13: Final "True - Estimated" RSW Differences for Each Scenario

Chapter 6

GNSS-Based Orbit Propagation

Following the Orbit Determination phase, this chapter analyses the propagation of the Estimated Orbits over time.
The prediction process involves comparing the Propagated Orbits with the corresponding Ground Truth. This evaluation is conducted for all four simulation configurations.
The propagation is performed using the TUDAT environment and the initial state is the final Keplerian elements resulting from the Orbit Estimation. Therefore, the accuracy of the propagation is directly influenced by the accuracy of the OD. The chapter is divided in "Not Perturbed Case" and "Perturbed Case", and in each chapter a comparison between orbits propagated from single- and dual-frequency GNSS measurements is performed.
To enable a fair comparison across all scenarios, the propagation is carried out over a fixed duration of two days.

6.1 Not Perturbed Case

The analysis of the Not Perturbed Case is fundamental, as it provides a clear understanding of the OP process, without the influence of orbital perturbations. The procedure is carried out for both single- and dual-frequency receivers. The reference orbit is the Not Perturbed one, and the same conditions listed in the "Not Perturbed Orbit" case in Table 4.2 are applied during the propagation

process.

The first step involves plotting the difference between the Propagated Orbit and its corresponding Ground Truth in the ECI frame (6.1, 6.2). A key result is the significant contrast between the two configurations: in the dual-frequency case, the final position differences remain within the order of the meters (approximately ± 2 m for X, ± 1.5 m for Y, and ± 2.5 m for Z). In contrast, the single-frequency case exhibits a deviation in the Along Track deviation of up to 300 m. The initial discrepancy demonstrates the significance of utilising dual-frequency measurements in OD, as it ensures a more accurate final position, leading to more precise propagation results.

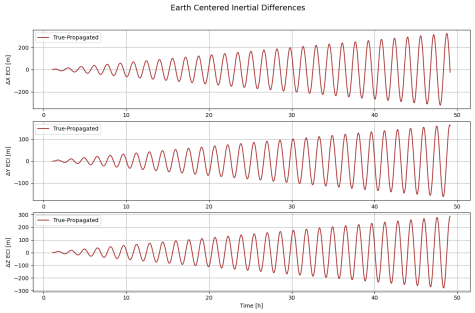

Figure 6.1: Single Frequency

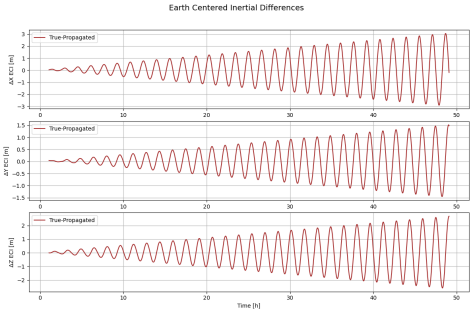

Figure 6.2: Dual Frequency

Figure 6.3: "True-Propagated" ECI Difference for Not Perturbed Case

More intuitive and operationally valuable results can be obtained by analysing the results in the RSW reference frame, in Figure 6.6. These plots represent the difference between where the satellite believes it is, based on the Propagated Orbit, and where it actually is, according to the True Orbit. From the RSW plots, it is straightforward to see that both the Radial and Cross-Track differences oscillate over time but remain relatively small in magnitude. Specifically, the ΔR difference for the single-frequency case (6.4) oscillates within ± 1.533 m after two days of propagation, compared to just ± 0.0371 m for the dual-frequency case (6.5). On the other hand, the ΔW difference shows a similar trend, with single-frequency deviations reaching ± 0.0715 m (6.19), while the dual-frequency case remains within ± 0.0401 m (6.20). However, the most important difference is seen in the ΔS difference: in the single-frequency case (6.16), ΔS reaches –325.8 m after two days, while in the dual-frequency case (6.17), it is limited to just –3.063 m.

Focusing on the Along-Track error, this behaviour can be attributed to inaccuracies in the estimation process, since the single-frequency case results in smaller

semi-major axis, as reported in Figure 6.7. As a result, the satellite moves faster along its orbit compared to the ground truth, causing it to gradually advance and accumulate Along-Track error.
In contrast, the improved estimation accuracy provided by the dual-frequency case, results in a more precise set of Keplerian elements, where the final classical elements of the OD are taken as initial state of the OP process. Indeed the semi-major axis differs from the reference one of 0.0100 m, as reported in Figure 6.8. Consequently, the resulting Along-Track deviation remains minimal, confirming the higher reliability of dual-frequency receiver measurements in OD and consequently in OP.

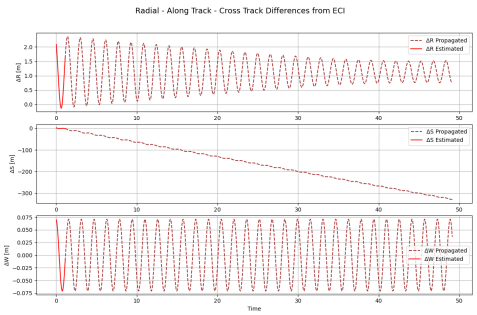

Figure 6.4: Single Frequency

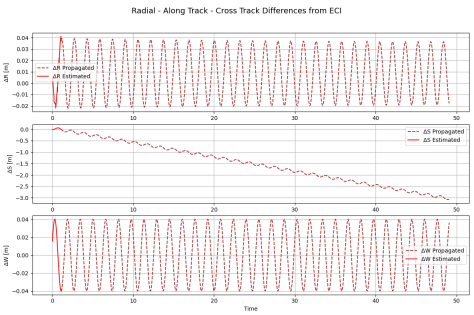

Figure 6.5: Dual Frequency

Figure 6.6: "True-Propagated" RSW Difference for Not Perturbed Case

Component	Value [m]
R	1.533
S	-325.830
W	0.0715

Table 6.1: Single Frequency

Component	Value [m]
R	0.0371
S	-3.063
W	0.0401

Table 6.2: Dual Frequency

Table 6.3: RSW Final Propagation Value for Not Perturbed Case

The RMSE serves as a way to quantify OP performance. As the propagation time increases, the instantaneous total RMSE naturally tends to grow.
The most interesting RMSE comparison lies in evaluating the overall results of the single- versus dual-frequency cases. In the single-frequency scenario (6.10), the total RMSE "True-Estimated" Overall is 1.182 m. After two days of propagation, the RMSE "True-Propagated" Overall increases significantly, reaching 190.820 m. On the other hand, in the dual-frequency case (6.11), RMSE "True-Estimated" Overall is much smaller at just 0.052 m. After two days of propagation, the RMSE "True-Propagated" Overall remains remarkably

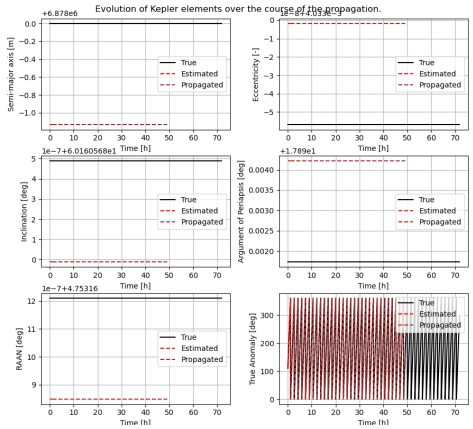

Figure 6.7: Single Frequency

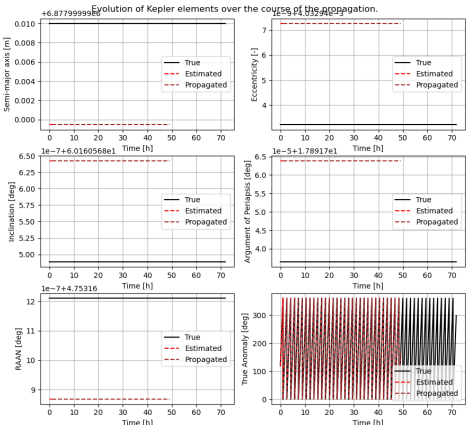

Figure 6.8: Dual Frequency

Figure 6.9: Kepler Elements for Not Perturbed Case: True Orbit, Estimated Orbit and Propagated Orbit

low at only 1.760 m.

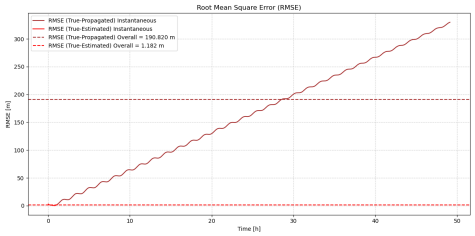

Figure 6.10: Single Frequency

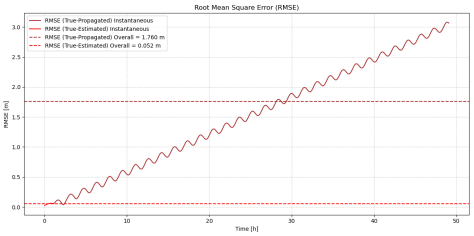

Figure 6.11: Dual Frequency

Figure 6.12: Total RMSE for Not Perturbed Case

Focusing on the individual components of the RSW reference frame, it becomes evident that the Along-Track component contributes most significantly to the total RMSE, coherently with the results from the RSW propagation analysis. In particular, for the single-frequency case, the Along-Track RMSE (6.16) increases from an initial "True–Estimated" value of 0.703 m to a final "True–Propagated" value of 190.816 m after two days. In contrast, the dual-frequency case (6.17) starts from a much lower initial value of 0.039 m and reaches only 1.760 m at the end of the propagation. A similar trend is observed in the Radial (6.13, 6.14) and Cross-Track components (6.19, 6.20).

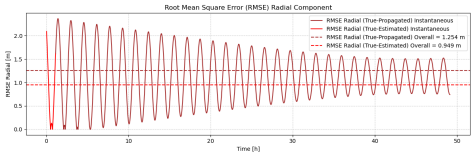

Figure 6.13: Single Frequency

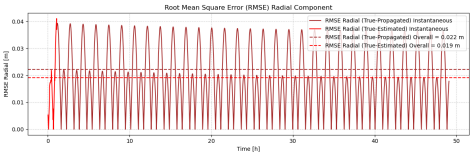

Figure 6.14: Dual Frequency

Figure 6.15: Radial RMSE for Not Perturbed Case

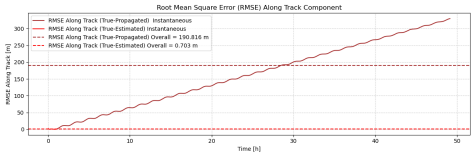

Figure 6.16: Single Frequency

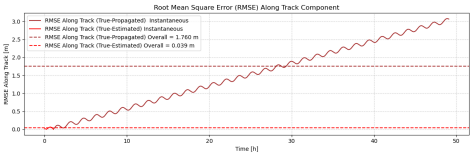

Figure 6.17: Dual Frequency

Figure 6.18: Along-Track RMSE for Not Perturbed Case

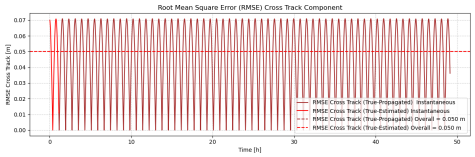

Figure 6.19: Single Frequency

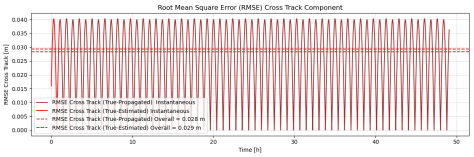

Figure 6.20: Dual Frequency

Figure 6.21: Cross-Track RMSE for Not Perturbed Case

Covariance Matrix and Formal Errors are computed during the propagation process to provide a more detailed understanding of the quality of solutions generated by TUDAT. It is important to note that these results assess the performance of the Propagated Orbit and should not be considered an alternative representation of the RSW results.

The Covariance Matrix used for propagation is derived from the final Covariance Matrix obtained during the estimation phase. From a space operations perspective, visualising these results as covariance ellipsoids is valuable, as offers a graphical representation of the satellite's positional uncertainty.

In the ECI reference frame, the Formal Errors (6.9) clearly demonstrate the greater accuracy of the dual-frequency configuration compared to the single-frequency one. The most notable improvement is seen in the X component, where the Formal Error decreases from around 15.93 m for single-frequency to 0.34 m for dual-frequency. However, the Y and Z components exhibit similar

levels of uncertainty in both configurations (∼21–39 m), suggesting that dual-frequency observations do not significantly improve estimation accuracy along these axes under Not-Perturbed conditions.

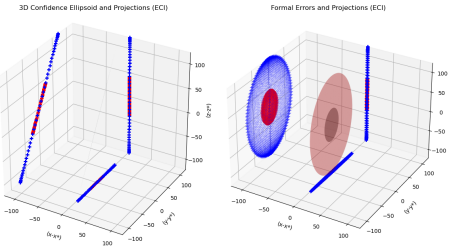

Figure 6.22: Single Frequency

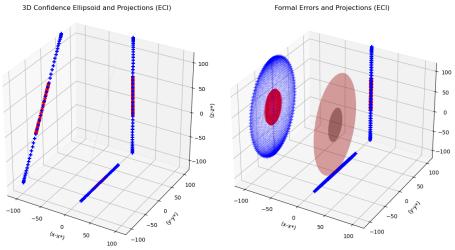

Figure 6.23: Dual Frequency

Figure 6.24: ECI Ellipsoids for Not Perturbed Case

Component	**Value [m^2]**
Cov(X,X)	2.538e+02
Cov(X,Y)	3.409e+02
Cov(X,Z)	6.185e+02
Cov(Y,Y)	4.577e+02
Cov(Y,Z)	8.305e+02
Cov(Z,Z)	1.507e+03

Table 6.4: Single Frequency

Component	**Value [m^2]**
Cov(X,X)	1.154e-01
Cov(X,Y)	-7.791e+00
Cov(X,Z)	-1.355e+01
Cov(Y,Y)	5.268e+02
Cov(Y,Z)	9.163e+02
Cov(Z,Z)	1.594e+03

Table 6.5: Dual Frequency

Table 6.6: Final ECI Covariance Matrix for the Not Perturbed Case

Component	Value [m]
X	15.93
Y	21.39
Z	38.82

Table 6.7: Single Frequency

Component	Value [m]
X	0.34
Y	22.95
Z	39.92

Table 6.8: Dual Frequency

Table 6.9: Final ECI Formal Errors for Not Perturbed Case

As expected, in the RSW frame, the Along-Track (S) component exhibits the highest uncertainty in both setups, with Formal Errors of approximately 47.10 m for the single-frequency solution and 46.05 m for the dual-frequency solution (6.15). This reinforces the idea that despite the improved initial state estimation provided by dual-frequency, the Along-Track direction is still more susceptible to errors.

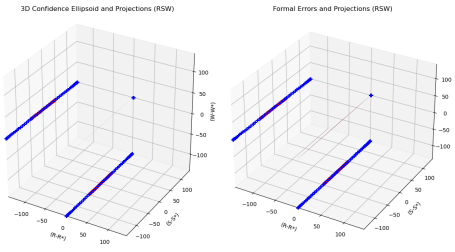

Figure 6.25: Single Frequency

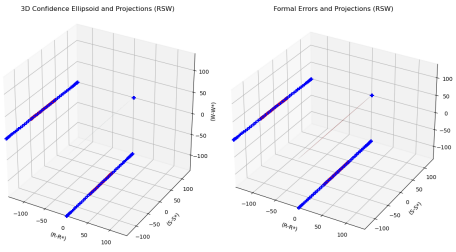

Figure 6.26: Dual Frequency

Figure 6.27: RSW Ellipsoids for Not Perturbed Case

Component	Value [m^2]
Cov(R,R)	3.191e-03
Cov(R,S)	-2.473
Cov(R,W)	1.902e-03
Cov(S,S)	2.218e+03
Cov(S,W)	-1.707
Cov(W,W)	2.038e-03

Table 6.10: Single Frequency

Component	Value [m^2]
Cov(R,R)	3.432e-02
Cov(R,S)	-8.505
Cov(R,W)	0.000
Cov(S,S)	2.121e+03
Cov(S,W)	-2.343
Cov(W,W)	5.968e-04

Table 6.11: Dual Frequency

Table 6.12: Final RSW Covariance Matrix for the Not Perturbed Case

Component	Value [m]
R	0.056
S	47.10
W	0.045

Table 6.13: Single Frequency

Component	Value [m]
R	0.185
S	46.05
W	0.024

Table 6.14: Dual Frequency

Table 6.15: Final Formal Errors for Not Perturbed Case

6.1.1 Not Perturbed Case Results

The analysis of the Not Perturbed case provides an initial insight into the behaviour of the propagation process. The results presented in this chapter demonstrate that achieving a more accurate final Keplerian state leads to reduced errors in the orbit propagation process, particularly in the dual-frequency case. This behaviour is observed in ECI and RSW reference frames.

It is clear from RSW and RMSE plots that the component showing the highest discrepancy is the Along-Track component. This error growth is directly linked to inaccuracies in the initial orbit estimation affecting the semi-major axis.
Propagated Covariance Matrices and Formal Errors further highlight the improved reliability of dual-frequency measurements. In the ECI frame the Formal Error in the X direction dropped from 15.93 m (single-frequency) to 0.34 m (dual-frequency), while the errors in the Y and Z directions remained comparable in both cases.
In the RSW frame, the Along-Track component continued to exhibit the highest uncertainty. This is also evident in the Covariance Ellipsoid, which provides visual confirmation of the quantitative results. These findings will serve as a baseline for comparison with the results from the Perturbed Case in the next section.

6.2 Perturbed Case

Considering the ECI differences, it is evident that these values increase for both Propagated orbits with respect to the Not Perturbed case, both for single-frequency or dual-frequency orbit. Specifically, the values change from approximately 200 m – 100 m – 300 m to 300 m – 150 m – 200 m in the single-frequency case and from 3 m – 1.5 m – 2.5 m to 20 m – 10 m – 15 m in the dual-frequency case. This behaviour is due to the introduction of perturbations.

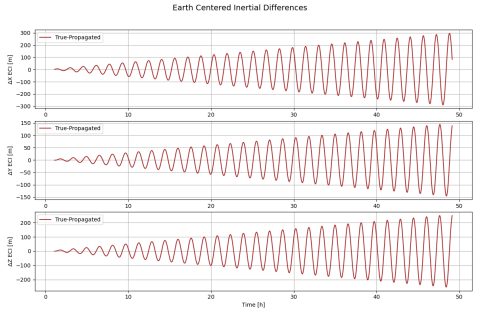

Figure 6.28: Single Frequency

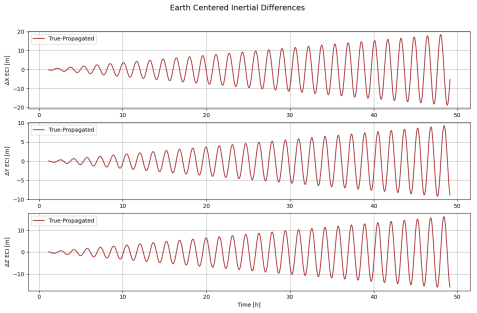

Figure 6.29: Dual Frequency

Figure 6.30: "True-Propagated" ECI Difference for Perturbed Case

As reported in Table 6.18 and Figure 6.33, the final values in the RSW frame are affected by changes as well.

Focusing on the single-frequency case and by comparing it with the correspondent Not Perturbed case, the Radial ΔR and Cross-Track ΔW components show a slight increase in their final values, whereas the Along-Track ΔS component exhibits a decrease. Referring to Table 5.13 for the single-frequency case, it is observed that the S component in the Not-Perturbed scenario is –1.455 m, compared to –1.405 m in the Perturbed case. This is a particular instance where the Determined Orbit derived from the Perturbed case performs better than the one from the Not-Perturbed case. Consequently, a more accurate OD with an error of 50 cm results in final propagated values differing by 27.9 m. This observation reinforces the idea that a more accurate OD leads to a more accurate OP.

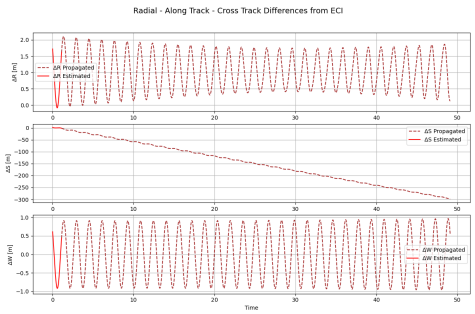

Figure 6.31: Single Frequency

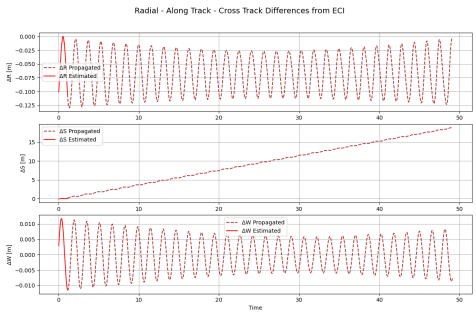

Figure 6.32: Dual Frequency

Figure 6.33: "True-Propagated" RSW Difference for Perturbed Case

Component	Value [m]
R	1.852
S	-297.930
W	0.971

Table 6.16: Single Frequency

Component	Value [m]
R	-0.123
S	19.034
W	0.083

Table 6.17: Dual Frequency

Table 6.18: RSW Final Propagation Value for Perturbed Case

Once again, the final RSW values obtained in the dual-frequency case are smaller than those in the corresponding single-frequency case, reflecting the greater accuracy of the OD process. However, when comparing the dual-frequency results for the Perturbed case in Table 6.18 with those of the Not-Perturbed case in Table 6.15, it becomes evident that all components increase due to the presence of perturbations. Nevertheless, the increase remains limited to under

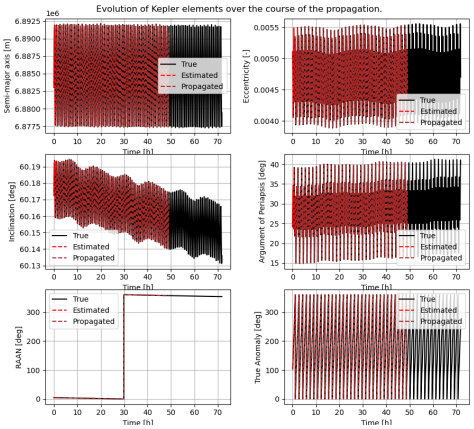

Figure 6.34: Single Frequency

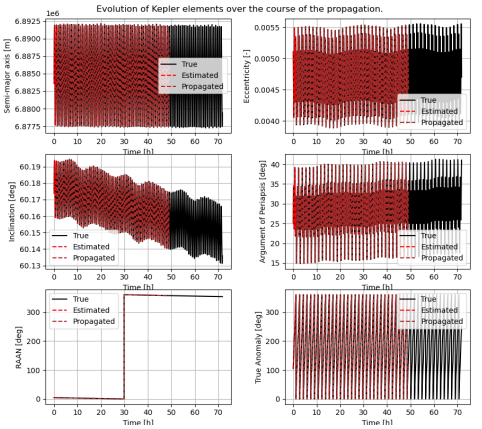

Figure 6.35: Dual Frequency

Figure 6.36: Kepler Elements for Perturbed Case: True Orbit, Estimated Orbit and Propagated Orbit

10 cm for the Radial ΔR and Cross-Track ΔW components.
By contrast, the Along-Track component exhibits a more significant change: the absolute value of ΔS increases from 3.063 m to 19.034 m. This growth is solely due to the introduction of perturbations in the propagation model.
In particular, the final Along-Track deviation for the dual-frequency Perturbed scenario is positive, unlike all other scenarios, where it is negative. This stems from the fact that the propagation process begins with the final estimated Keplerian elements derived from the OD. Specifically, the estimation suggests a larger semi-major axis than the reference orbit. Consequently, the propagated satellite appears to advance along its trajectory, resulting in an increase in the Along-Track difference over the two-day propagation period. Unlike the Not-Perturbed case, the differences in Keplerian elements between the Estimated Orbit and Propagated Orbit are not clearly visible in Figure 6.36. However, it can be seen that the propagated Keplerian elements closely follow the trend of the True classical elements.
The described behaviours are further highlighted by considering the RMSE plots and values. As mentioned preivously, the Along-Track component is clearly the most significant contributor to the total RMSE, in line with the results from the RSW propagation analysis.

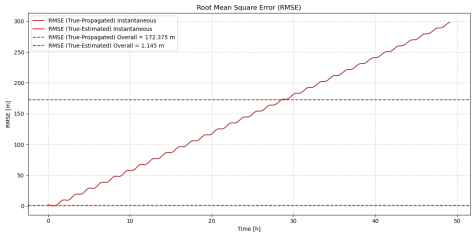

Figure 6.37: Single Frequency

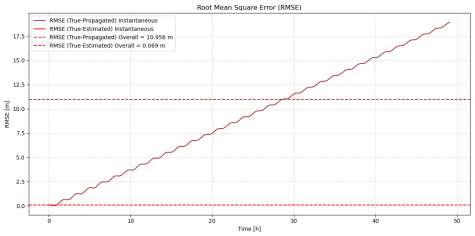

Figure 6.38: Dual Frequency

Figure 6.39: Total RMSE for Perturbed Case

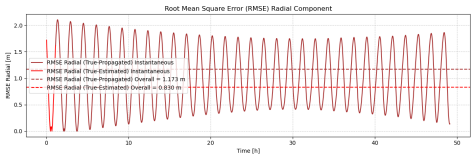

Figure 6.40: Single Frequency

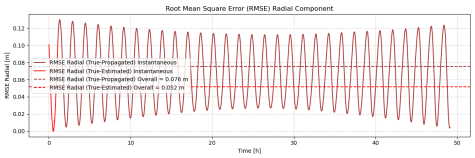

Figure 6.41: Dual Frequency

Figure 6.42: Radial RMSE for Perturbed Case

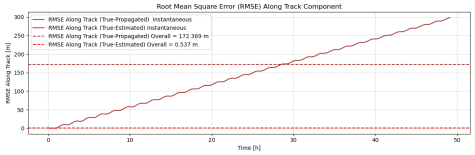

Figure 6.43: Single Frequency

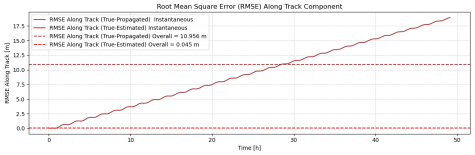

Figure 6.44: Dual Frequency

Figure 6.45: Along-Track RMSE for Perturbed Case

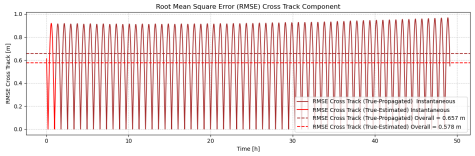

Figure 6.46: Single Frequency

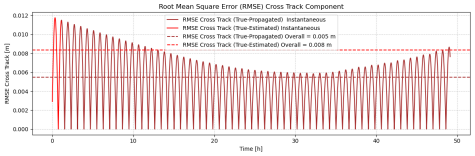

Figure 6.47: Dual Frequency

Figure 6.48: Cross-Track RMSE for Perturbed Case

In the ECI frame, both single- and dual-frequency cases exhibit similar covariance structures, with the largest uncertainties observed in the Z component. The covariance values are slightly lower in the dual-frequency case. This is consistent with the Formal Errors, where the dual-frequency solution shows

slightly reduced values across all components.
When comparing the Perturbed and Not-Perturbed cases, the Covariance Matrix and Formal Errors of the single-frequency are slightly larger in the Perturbed case, but negligible.
One interesting aspect to highlight is that the Covariance Matrix obtained in the dual-frequency Perturbed case shows significantly higher values from the Not-Perturbed case: for instance, Cov(X,X) increases from 1.154×10^{-1} m^2 to 2.574×10^{2} m^2. This leads to an increase in Formal Errors, from approximately $X = 0.34$ m, $Y = 22.95$ m, $Z = 39.92$ m to $X = 16.04$ m, $Y = 21.26$ m, $Z = 38.58$ m, bringing the results closer to those of the single-frequency scenario. This behavior can be explained by the addition of perturbations: the dual-frequency orbit determination (OD) is more accurate, which makes the model more sensitive to small changes. When perturbations are added, the Formal Errors increase during propagation.
This does not happen in the single-frequency case, because it begins with larger initial uncertainties, making the additional effect of perturbations negligible in the context of Covariance Matrices computation.

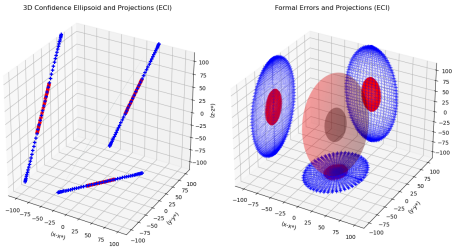

Figure 6.49: Single Frequency

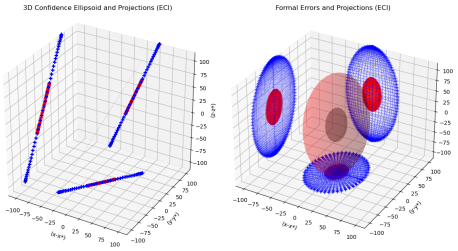

Figure 6.50: Dual Frequency

Figure 6.51: ECI Ellipsoids for Perturbed Case

Component	**Value [m^2]**
Cov(X,X)	2.581e+02
Cov(X,Y)	3.433e+02
Cov(X,Z)	6.230e+02
Cov(Y,Y)	4.565e+02
Cov(Y,Z)	8.285e+02
Cov(Z,Z)	1.504e+03

Table 6.19: Single Frequency

Component	**Value [m^2]**
Cov(X,X)	2.574e+02
Cov(X,Y)	3.411e+02
Cov(X,Z)	6.191e+02
Cov(Y,Y)	4.518e+02
Cov(Y,Z)	8.201e+02
Cov(Z,Z)	1.489e+03

Table 6.20: Dual Frequency

Table 6.21: Final ECI Covariance Matrix for the Perturbed Case

Component	Value [m]
X	16.07
Y	21.37
Z	38.78

Table 6.22: Single Frequency

Component	Value [m]
X	16.04
Y	21.26
Z	38.58

Table 6.23: Dual Frequency

Table 6.24: Final ECI Formal Errors for Perturbed Case

This behaviour is not registered in the RSW Reference Frame, since the RSW frame, which rotates with the satellite and aligns with its orbital motion, the effect of perturbations is absorbed more smoothly.
In the RSW frame, the Along-Track (S) component consistently accounts for the largest values of Covariance Matrix and Formal Error. Specifically, Cov(S,S) exceeds 2200 m^2 in both frequency cases, and the corresponding formal error remains high (47 m), while the Radial (R) and Cross-Track (W) components maintain values below 0.0540 m. The dual-frequency case shows slightly reduced Covariance and Formal Errors, highlighting the improved performance of OD.
In the Perturbed case, the Along-Track uncertainty remains the main contributor, suggesting that the Along-Track direction is more sensitive to propagation and determination errors.

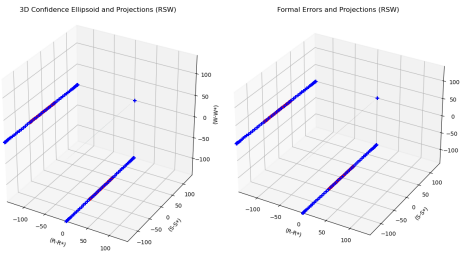

Figure 6.52: Single Frequency

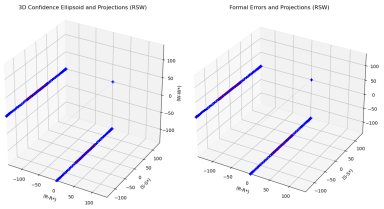

Figure 6.53: Dual Frequency

Figure 6.54: RSW Ellipsoids for Perturbed Case

Component	Value [m^2]
Cov(R,R)	3.031e-03
Cov(R,S)	-2.398
Cov(R,W)	1.844e-03
Cov(S,S)	2.218e+03
Cov(S,W)	-1.706
Cov(W,W)	2.038e-03

Table 6.25: Single Frequency

Component	Value [m^2]
Cov(R,R)	2.914e-03
Cov(R,S)	-2.320
Cov(R,W)	1.783e-03
Cov(S,S)	2.198e+03
Cov(S,W)	-1.690
Cov(W,W)	2.032e-03

Table 6.26: Dual Frequency

Table 6.27: Final RSW Covariance Matrix for the Perturbed Case

Component	Value [m]
R	0.0551
S	47.097
W	0.0451

Table 6.28: Single Frequency

Component	Value [m]
R	0.0540
S	46.882
W	0.0451

Table 6.29: Dual Frequency

Table 6.30: Final Formal Errors for Perturbed Case

6.2.1 Perturbed Case Results

In the Perturbed Case, the use of dual-frequency measurements still leads to a more accurate Orbit Determination and, consequently, a more accurate Orbit Propagation. When compared to the Not Perturbed Case, a slight degradation in the RSW components can be observed, which is solely due to the introduction of perturbations. Despite this, the dual-frequency results remain highly reliable,

with the final along-track error increasing to 19.034 m, compared to 3.063 m in the Not Perturbed scenario.

6.3 Orbit Propagation Results

In the absence of perturbations, propagation is primarily influenced by the initial state derived from the OD. As expected, the dual-frequency case, which benefits from more accurate GNSS measurements and OD, results in smaller deviations in the Propagated Orbit. Formal Errors and RSW differences confirm that the dual-frequency solution improves the accuracy of the Propagated Orbit.
When perturbations are introduced, their influence becomes more evident. Interestingly, the dual-frequency case shows a larger increase in propagated Formal Errors than the single-frequency case. Despite the increased formal errors, the dual-frequency results are more consistent and reliable. The RSW frame confirms this behaviour, with small variations mainly concentrated on the Along-Track component.

Overall, the dual-frequency approach is more effective in both the Not Perturbed and Perturbed scenarios, emphasising the importance of accurate initial conditions for orbit prediction.

Chapter 7

GNSS-Based TLEs and SGP-4 Propagation

TLE data are typically generated from observations collected via ground-based tracking stations, radar systems, or optical sensors. In this work it was considered valuable to generate TLEs directly from GNSS measurements previously generated through Skydel.
Once generated, the TLEs were propagated using SGP-4, a standard orbital propagator used to predict satellite positions from TLE data. It applies its own set of perturbations, accounts for Earth's gravitational field, atmospheric drag, and other relevant perturbations. The workflow followed is reported in Figure G.2.
These evaluations form the basis for comparing the Orbit Determination and Propagation process described earlier with a classical Orbital Data format like the TLE. It is important to note, however, that the TLEs generated in this section should not be misunderstood with operational radar-derived TLEs.
To enable a fair comparison, the propagation was carried out over a fixed duration of two days.

7.1 Not Perturbed Case

Initially, TLEs were generated using GNSS-based measurements from the Not Perturbed scenario. These were, then, propagated using the SGP-4 model, which produced results of limited accuracy. Notably, in the dual-frequency

case, the convergence process terminated after only two hours. This was due to the higher precision of the dual-frequency measurements, which could not be aligned with the constraints of the SGP-4 model.
In both the single- and dual-frequency cases, the GNSS-based TLEs generated in the Not Perturbed scenario were unreliable. This is primarily because the SGP-4 model applies its own internal perturbation models, which cannot and should not be modified. Consequently, GNSS-based Not Perturbed measurements are incompatible with the assumptions embedded in the SGP-4 framework. This is reflected in the ECEF differences: in Figure 7.3, the difference between the SGP-4 Propagated Orbit and the Ground Truth is reported. It can be noted that in all cases, the value reaches $10^7 m$, confirming this unrealibility. It is important to note that, in this case, the ECEF frame is used instead of ECI, since the SGP-4 model operates in the TEME reference frame. Using the Skyfield library, the conversion from TEME to ECEF is handled precisely.

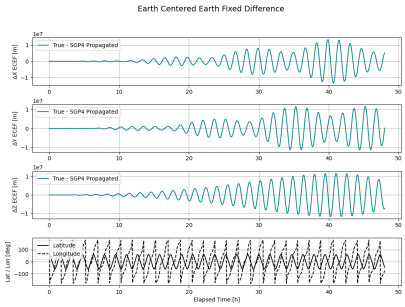

Figure 7.1: Single Frequency

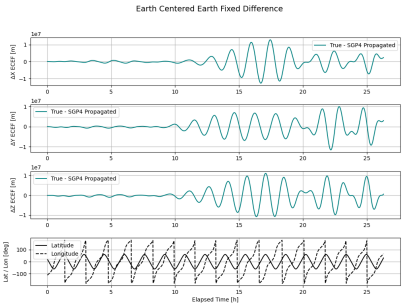

Figure 7.2: Dual Frequency

Figure 7.3: ECEF Differences for Not Perturbed Case

This limitation is clearly reflected in the comparison of Keplerian elements over time. The classical elements of the Reference Orbit, derived from the GNSS data, remain constant throughout the propagation period. In contrast, the SGP-4-based propagation exhibits significant oscillations and deviations, which are straightforward to see in the semi-major axis, indicating a decay of the orbit due to SGP-4's perturbations.
Consequently, the results obtained in the Not Perturbed case are not considered reliable for comparison or analysis.

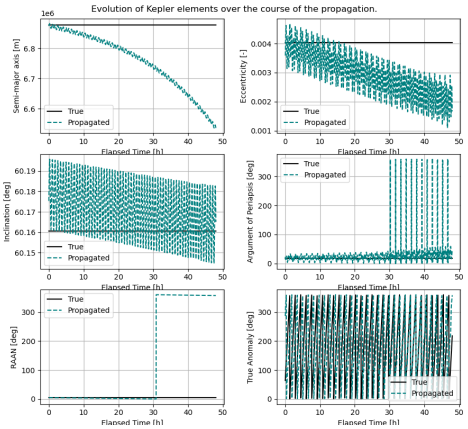

Figure 7.4: Single Frequency

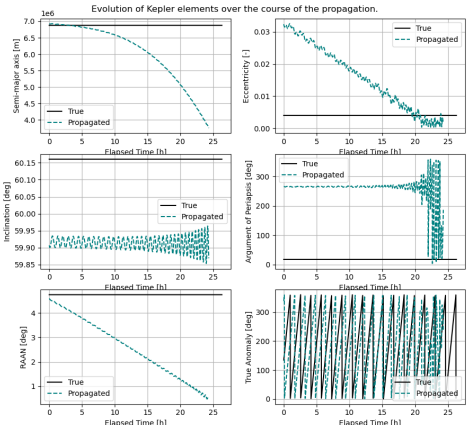

Figure 7.5: Dual Frequency

Figure 7.6: Keplerian Elements for Not Perturbed Case

7.2 Perturbed Case

During the two-day propagation period, GNSS-based measurements from the Perturbed scenario were found to be more accurate than those from the previous scenario. Indeed, the ECEF differences were found to span up to 5000 m for the single-frequency case and up to 2500 m for the dual-frequency case, compared to $10^7 m$ in the Not Perturbed case. This provides a firmer basis for comparisons and analyses of this kind of propagation with respect to the Ground Truth.

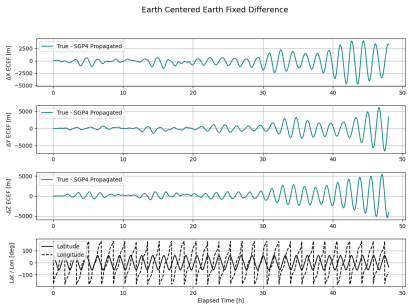

Figure 7.7: Single Frequency

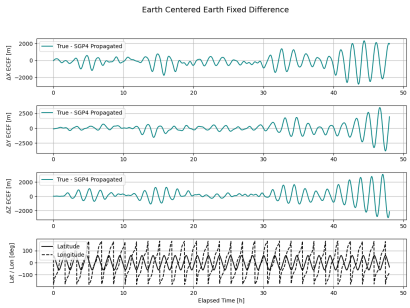

Figure 7.8: Dual Frequency

Figure 7.9: ECEF Differences for Perturbed Case

To better understand the behaviour of the SGP-4 propagator, it was tested over a time span equal to the total duration of the GNSS measurements, approximately 80 minutes. This short-term propagation allows for an evaluation of the SGP-4

model's ability to accurately reproduce the observed trajectory within the time window used for OD. Practically speaking, it provides a direct comparison between the propagated TLE-based solution and the actual measurements.

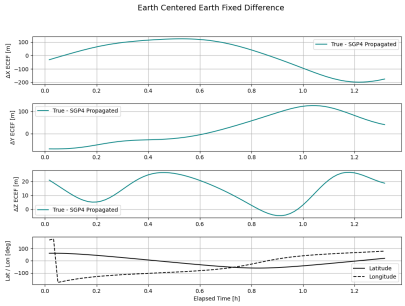

Figure 7.10: Single Frequency

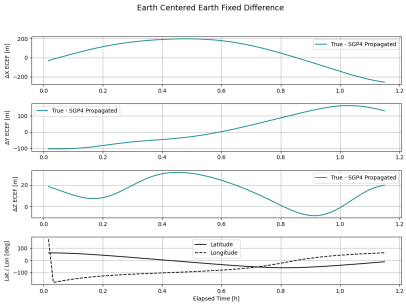

Figure 7.11: Dual Frequency

Figure 7.12: ECEF Differences for Perturbed Case - 80 minutes

For both single- and dual-frequency cases, the initial propagated state is significantly misaligned with respect to the true state, despite the expectation of a close match. This discrepancy arises from the intrinsic limitations of the TLE generation process. The differences between the TLE and the Ground Truth should not be surprising: TLEs consist of mean orbital elements obtained through a least-squares fit to tracking data and, more importantly, rely on a simplified dynamical model.
Once the TLE fitting algorithm converges, both the reference orbit (Original Solution) and the derived Keplerian elements (Final TLE Solution) are presented.

For the single-frequency case:

```
Final TLE Solution:  6885.564, 0.00434, 60.165, 5.148, 16.999, 8.938,
+1.099e-03
Original Solution:  6890.284, 0.00530, 60.181, 5.166, 36.461, 349.562,
+1.0000e-06
```

For the dual-frequency case:

```
Final TLE Solution:  6885.545, 0.00434, 60.165, 5.148, 17.018, 11.326,
+4.400e-03
Original Solution:  6888.557, 0.00504, 60.173, 5.166, 37.433, 351.001,
+1.0000e-06
```

These differences imply an initial mismatch in the classical orbital elements, which is particularly evident considering the first element which represent the semi-major axis. This difference reaches values of nearly 5 km for the single-frequency case and 3 km for the dual-frequency case. This misalignment directly impacts the propagated trajectory and is reflected in the final ECEF differences:

Single Frequency: ΔX = -31.3 m, ΔY = -68.168 m, ΔZ = 21.315 m

Dual Frequency: ΔX = -23.5 m, ΔY = -123.8 m, ΔZ = 28.85 m

These results confirm that inaccuracies in the TLE generation process, lead to significant errors when propagated using SGP-4.

The mismatch between the Original Solution and Final solution is further confirmed in the Keplerian elements plot over the 80 minutes period. With

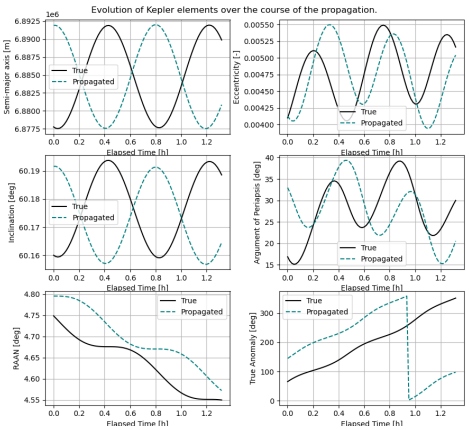

Figure 7.13: Single Frequency

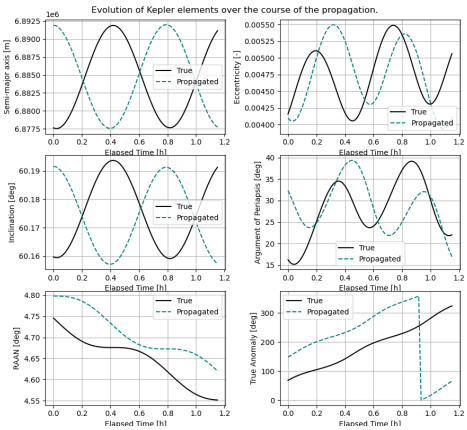

Figure 7.14: Dual Frequency

Figure 7.15: Keplerian Elements for Perturbed Case - 80 minutes

respect to the GNSS-based TLEs generated in the Not Perturbed scenario, the Keplerian elements obtained in the Perturbed case follow the Reference Orbit more closely. However, as shown in Figure 7.15, noticeable discrepancies still remain, and the two sets of classical elements are not identical.

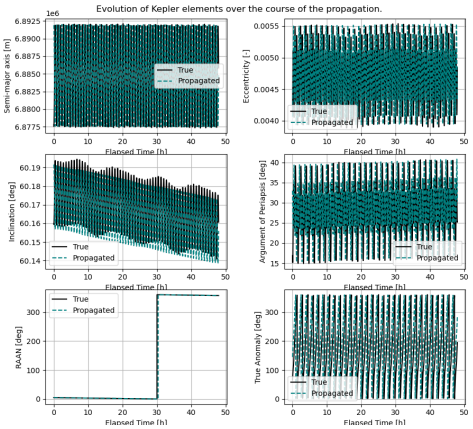

Figure 7.16: Single Frequency

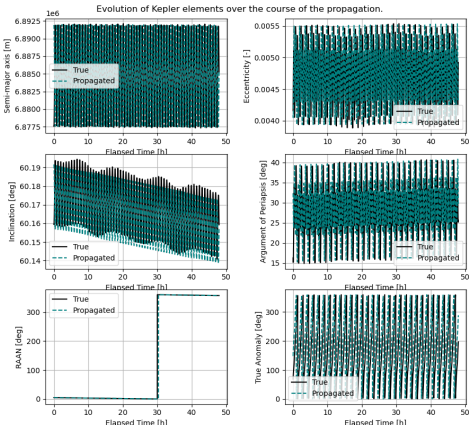

Figure 7.17: Dual Frequency

Figure 7.18: Keplerian Elements for Perturbed Case

To enable a fair comparison with the OP results obtained in Chapter 5, RSW and RMSE results are computed.

The final values of the propagation process are similar for single- and dual-frequency cases in the Radial ΔR and ΔW component, reaching $\pm$ 200 m and $\pm$ 500 m (7.21). For the Along-Track component ΔS, instead, the final value is 5500 m for the single frequency case and 4000 m for the dual frequency case. This suggests that even though the dual-frequency approach in the OD and OP analysis was more accurate than the single-frequency case, in this context yields almost to the same results in the ΔR and ΔW, while improving the accuracy of the ΔS component by 1.5 km.

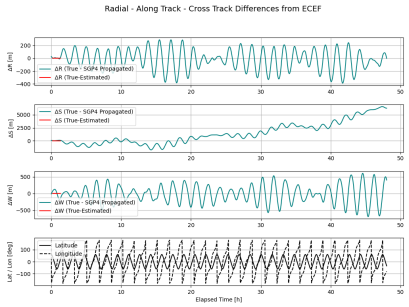

Figure 7.19: Single Frequency

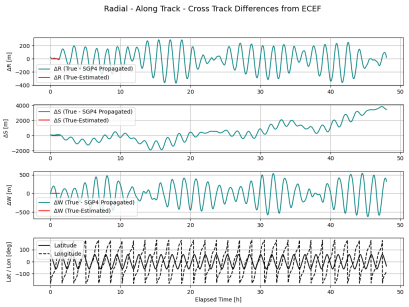

Figure 7.20: Dual Frequency

Figure 7.21: RSW for Perturbed Case

The final value of the RMSE "True - SGP4 Propagated" Instantaneous reaches approximately 6500 m for the single-frequency case, and about 4000 R for the

dual-frequency case (7.22, 7.23) .
When comparing the single- and dual-frequency results, both cases exhibit similar behavior in the Radial and Cross-Track components, as confirmed by their overall RMSE values. The most significant difference lies in the Along-Track component, which remains the main contributor to the total RMSE. In particular, the Along-Track RMSE reaches approximately 2.5 km in the single-frequency case and 1.4 km in the dual-frequency case.

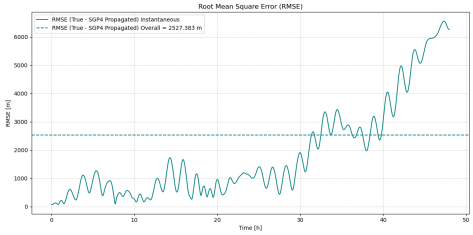

Figure 7.22: Single Frequency

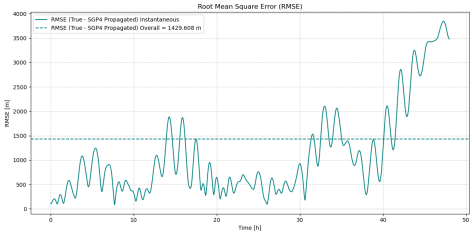

Figure 7.23: Dual Frequency

Figure 7.24: Total RMSE for Perturbed Case

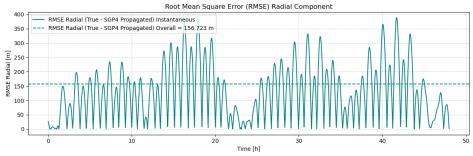

Figure 7.25: Single Frequency

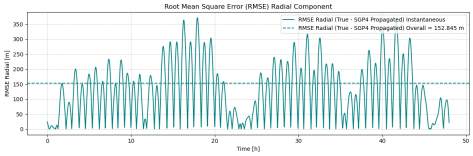

Figure 7.26: Dual Frequency

Figure 7.27: Radial RMSE for Perturbed Case

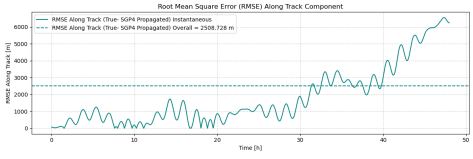

Figure 7.28: Single Frequency

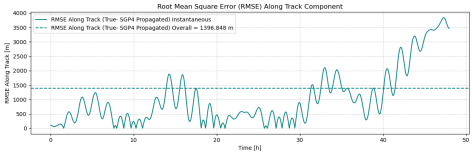

Figure 7.29: Dual Frequency

Figure 7.30: Along-Track RMSE for Perturbed Case

7.3 GNSS-Based TLEs and SGP-4 Propagation Results

The SGP-4 propagation based on GNSS Not Perturbed measurements proves to be unreliable. This is because SGP-4 introduces its own perturbations, which

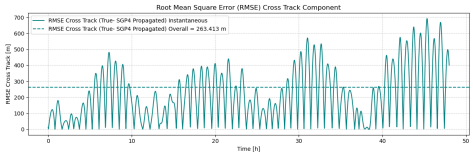

Figure 7.31: Single Frequency

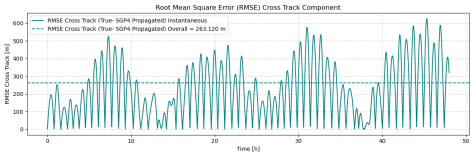

Figure 7.32: Dual Frequency

Figure 7.33: Cross-Track RMSE for Perturbed Case

were not present in the original trajectory and cannot be disabled or tuned. On the other hand, when GNSS perturbed measurements are used as input, the SGP-4 propagator yields more consistent results, in the same order of magnitude of conventional TLEs [10]. However, even in this improved scenario, after two days of propagation the final RMSE reaches approximately 6.5 km, a great contrast to the few meters of error obtained with the OD performed using TUDAT.

7.4 Overall Propagation Results

The results of the considered propagation methods, as reported by the RSW, are presented in Table 7.1. This allows for a straightforward and operationally efficient comparison.

Final Value	SingleF	TLE from SingleF	DualF	TLE from DualF
R [m]	1.852	±200	-0.123	±200
S [m]	-297.93	5500	19.034	4000
W [m]	0.971	±1000	0.0830	±500

Table 7.1: Final RSW Propagation Values Compared with TLE-Based Values for the Perturbed Case

It can be mentioned that the Orbit Propagation based on the Determination using TUDAT outperforms the standard TLE-based propagation. This advantage highlights the robustness and predictive capabilities of the developed OD/OP methodology compared to the traditional SGP-4 approach.

Chapter 8

Conclusions

8.1 Analysis of the Results

The availability of high-precision, low-latency orbital information is a fundamental requirement for many space missions. This requirement is particularly critical for CubeSats, which typically operate in LEO and are not equipped with propulsion systems. The increasing congestion of the LEO environment, due to both active satellites and orbital debris, makes accurate knowledge of the spacecraft state, essential for collision avoidance. In this context, it is necessary to determine the satellite position and velocity with accuracy, quantify the associated uncertainty through a covariance estimate, and transmit this information to the ground segment.
POD for LEO satellites can be performed on the ground after GNSS data are downlinked. However, this approach may introduce latency, as it is strictly dependent on the availability of ground contacts, and reduced operational responsiveness. This dependency can be mitigated, and the overall latency significantly reduced, by performing POD directly on-board the spacecraft.
This thesis has addressed the design, implementation, and assessment of an Orbit Determination and propagation algorithm based on GNSS measurements.

In **Chapter 4**, the generation of the ground-truth orbit and the corresponding measurements was discussed for both perturbed and unperturbed cases. A reference orbit was first generated, followed by the simulation and collection of GNSS measurements using Skydel. The analysis of these measurements

confirmed that GNSS receivers inherently introduce noise, which cannot be completely eliminated, even under ideal orbital conditions. Furthermore, the results showed that GNSS receivers are more sensitive to radial position errors.

In **Chapter 5**, Orbit Determination was subsequently performed using these measurements. The results demonstrate that the use of dual-frequency observations enhances the measurement quality and reduced residuals, leading to an Estimated Orbit closer to the Ground Truth. In the TwinSat case study, the satellites operate in LEO, where atmospheric drag plays a significant role. For this reason, the adoption of a dual-frequency receiver is particularly advantageous, as it reduces residuals through ionospheric mitigation.

In **Chapter 6**, accurate orbit prediction was identified as a necessary subsequent step to Orbit Determination. Given the estimated state, it is essential to determine the future position of the satellite, for example to predict upcoming ground station contacts or, in critical scenarios, to assess the risk of potential collisions. To this end, an accurate propagation model was developed starting from the final Keplerian state obtained from the Orbit Determination process. This analysis highlighted the strong dependence of orbit prediction accuracy on the quality of the initial state estimation.

In **Chapter 7**, orbit propagation using TLEs generated from on-board GNSS measurements was performed. The results confirmed that the prediction algorithm developed in the previous chapter provides a more reliable propagation model. Indeed, a comparison of the RMSE shows that the error associated with TLE-based propagation reaches approximately 6.5 km after two days, whereas the Orbit Determination and propagation performed using TUDAT results in errors of only a few meters.

Considering the orbit generation and propagation performed using TUDAT, the results of Orbit Determination and prediction must be distributed in a standardized and operationally usable format. Satellite operators typically access precise orbital information through orbital data messages, provided either as TLEs or as OEM files. As demonstrated in Chapter 7, TLEs derived from GNSS measurements approach is not sufficiently reliable for the considered case. Therefore, in the context of this thesis, position, velocity, and covariance information are combined into OEM files directly derived from the POD solution. These messages provide improved accuracy and are suitable for advanced

collision risk analysis and precise orbit prediction.
To ensure the reliability of the obtained on-board POD solution, an independent validation method is required. In the TwinSat case study, this validation will be performed through comparison with satellite laser ranging measurements, as the TwinSats will be equipped with this capability. The combined use of GNSS and laser ranging, however, lies beyond the scope of this thesis.

8.2 Future Work

The on-board algorithms and simulations developed in this thesis can serve as a foundation for further iterations of the TwinSat mission project. During the development of this work, several suggestions for future research emerged, which could contribute to the investigation of new concepts of remarkable interest.

With respect to the Skydel GNSS measurements, future work may include:

- **Long-term simulation analysis**: Extending the duration of the Skydel simulations to study long-term effects on determination and prediction algorithms, eventually analysing navigation solution degradations caused by periodicity effects;

With respect to the GNSS receivers:

- **Almanac-assisted acquisition**: Extracting the GNSS almanac and feeding it into the receiver to evaluate possible improvements in acquisition time and positioning accuracy;
- **Receiver testing**: Testing the on-board setup with alternative receivers to validate the overall configuration and compare results.

With respect to the on-board Orbit Determination algorithm, possible extensions include:

- **Ground Truth configuration**: Repeating the analyses for different orbital configurations, particularly at higher inclinations;
- **Dynamic model refinement**: Improving the estimation of perturbed orbits by adding and redefining force models, updating gravitational parameters, defining the spacecraft macromodel, and accounting for GNSS antenna placement;
- **Broadcast ephemeris navigation**: Determine the orbit directly from

broadcast ephemerides, to reduce computational complexity;

- **Ionospheric correction from RINEX**: Processing ionospheric errors directly from RINEX observation files and applying the corresponding corrections;
- **Laser ranging integration**: Integrating on-board Orbit Determination with laser ranging measurements to validate and verify the GNSS-based algorithm;
- **TwinSat separation analysis**: Study the relative separation between the TwinSats in orbit using GNSS measurements, Orbit Determination and Propagation.

Bibliography

[1] ESA Space Debris Mitigation Working Group. *ESA Space Debris Mitigation Requirements*. Standard (STD) ESSB-ST-U-007. Approved. European Space Agency, Oct. 2023 (cit. on p. III).

[2] *What are SmallSats and CubeSats*. URL: `https://www.nasa.gov/what-are-smallsats-and-cubesats/` (cit. on p. 1).

[3] "Cubesat design specification". In: *The CubeSat Program, Cal Poly San Luis Obispo, US* 1.2 (2014) (cit. on p. 2).

[4] Thyrso Villela, Cesar A Costa, Alessandra M Brandão, Fernando T Bueno, and Rodrigo Leonardi. "Towards the thousandth CubeSat: A statistical overview". In: *International Journal of Aerospace Engineering* 2019.1 (2019), p. 5063145 (cit. on p. 2).

[5] Gunter Dirk Krebs. *Gunter's Space Page: Nanosats Database*. 2024. URL: `https://www.nanosats.eu/` (cit. on p. 2).

[6] ESA Space Debris Office. *ESA's Annual Space Environment Report*. Tech. rep. European Space Agency, 2023 (cit. on p. 2).

[7] Sajjad Kazemi, Nasser L Azad, K Andrea Scott, Haroon B Oqab, and George B Dietrich. "Orbit determination for space situational awareness: A survey". In: *Acta Astronautica* (2024) (cit. on pp. 4, 5).

[8] *Space Track Website*. URL: `https://www.space-track.org/auth/login` (cit. on pp. 5, 7).

[9] Filippo Graziani and Simone Battistini. "Orbit determination and control system". In: *Cubesat Handbook*. Elsevier, 2021, pp. 251–261 (cit. on p. 5).

[10] Jacco Geul, Erwin Mooij, and Ron Noomen. "TLE uncertainty estimation using robust weighted differencing". In: *Advances in Space Research* 59.10 (2017), pp. 2522–2535 (cit. on pp. 5, 87).

[11] Arnaud Dion, Vincent Calmettes, Michel Bousquet, and Emmanuel Boutillon. “Performances of a GNSS receiver for space-based applications”. In: *arXiv preprint arXiv:1809.10086* (2018) (cit. on p. 6).

[12] PINK BOOK. “Orbit Data Messages”. In: (2009) (cit. on p. 8).

[13] Norbert Jakowski, Christoph Mayer, Volker Wilken, and Mohammed M Hoque. “Ionospheric impact on GNSS signals”. In: *Física de la Tierra* 20 (2008), p. 11 (cit. on pp. 17, 46, 55).

[14] *Error Sources and Error Characterization, Engineering Satellite-Based Navigation and Timing: Global Navigation Satellite Systems, Signals, and Receivers*. Dec. 2015. DOI: 10.1002/9781119141167.ch6. URL: http://dx.doi.org/10.1002/9781119141167.ch6 (cit. on p. 18).

[15] Huazheng Du, Yunqing Hong, Na Xia, Guofu Zhang, Yongtang Yu, and Jiwen Zhang. “A navigation satellites selection method based on ACO with polarized feedback”. In: *IEEE Access* 8 (2020), pp. 168246–168261 (cit. on p. 18).

[16] MA Amal. “Determination of the Geoid Height (Geoid Undulation) By Using Modern Surveying Technologies Applied Research Journal Vol. 2”. In: *Issue* 10 (2016), pp. 403–411 (cit. on p. 32).

[17] *How to calculate radial, along-track, cross-track (RAC) orbital errors*. https://www.researchgate.net/post/How-to-calculate-radial-along-track-cross-track-RAC-orbital-errors (cit. on p. 34).

[18] Emiliano Cordelli. “Improvement of Space Debris Orbits”. Advisors: Prof. Dr. Thomas Schildknecht and Dr. Alessandro Vananti. Ph.D. dissertation. Bern, Switzerland: University of Bern, 2020 (cit. on p. 34).

[19] Skydel Solutions. *Skydel Software-Defined GNSS Simulator: User Manual*. Revision: v24.12. Skydel Solutions. Dec. 2024 (cit. on p. 38).

[20] Marianna Centrella. “Mission and System Design of a Formation-Flying Picosatellites Cluster: A Technology Demonstration Mission for Space Situational Awareness Improvement”. PhD thesis. Politecnico di Torino, 2023 (cit. on p. 39).

[21] Lukas Müller, Kangkang Chen, Gregor Möller, Markus Rothacher, Benedikt Soja, and Lola Lopez. “Real-time navigation solutions of low-cost off-the-shelf GNSS receivers on board the Astrocast constellation satellites”. In: *Advances in Space Research* 73.1 (2024), pp. 2–19 (cit. on p. 46).

[22] *tle-tailor: Tools for tailoring TLEs to observed data.* `https://github.com/dcajacob/tle-tailor` (cit. on p. 107).

APPENDIX A

GNSS Simulator Guide

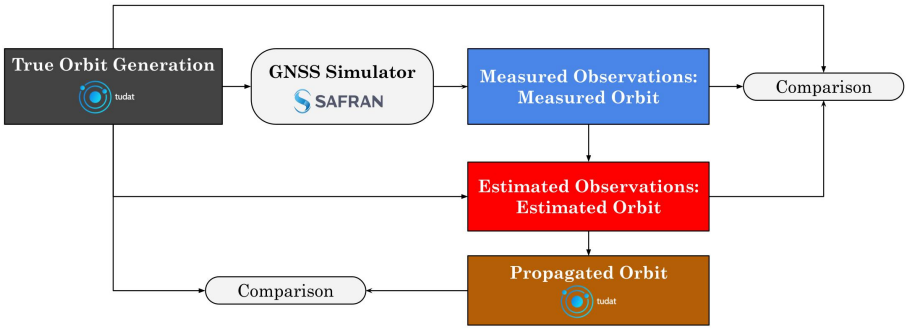

Figure A.1: GNSS Simulator Guide - Workflow

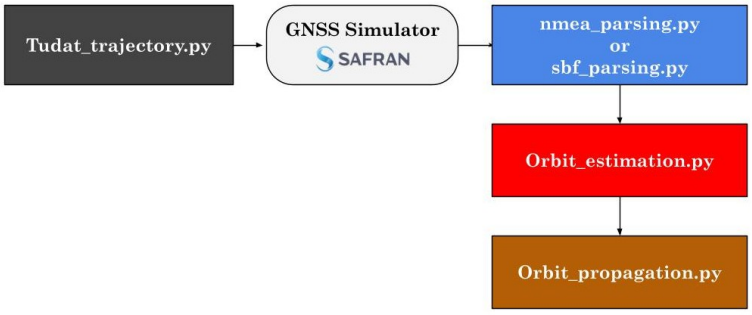

Figure A.2: GNSS Simulator Guide - Code Workflow

APPENDIX B

True Orbit Generation

The first step is to generate a reference orbit. This can be done using the script `Tudat_trajectory.py`. This script propagates an orbit based on settings that the user must adjust directly in the code:

1. Select the type of propagation to perform (perturbed or unperturbed orbit).
2. Set the simulation start and end epochs by specifying the year, month, day, hour, minute, and seconds.
3. Set the initial state in Keplerian elements according to the desired orbit.

The generated data are saved as TXT files, which should be renamed appropriately to match the generated orbit. These files are automatically stored in the `TXT_Files` folder.

Once this orbit is generated, it needs to be converted into a suitable format for Skydel. The chosen format is `.csv`.
To convert the `.txt` files to `.csv`, open `gnss_conversions.py` and use the `convert_txt_to_csv` function. By specifying the input `.txt` file correctly, the corresponding `.csv` file will be created with the same name and saved in the same folder as the input file.
For this thesis, the ECEF file was selected and converted.

APPENDIX C

GNSS Simulator

Once the reference ECEF orbit is generated, it needs to be loaded into Skydel. Before starting the simulation, properly adjust the attenuator: set it to 50 dB for the single-frequency receiver (Skydel S12168F8-GI3), 40 dB for the dual-frequency receiver Septentrio, and 30 dB for the other two dual-frequency receivers (ORION B16-C and SkyTrack PX1122C). Then, open Skydel and create a new configuration. The following settings must be applied to reproduce the results of this thesis:

1. **Settings > Output**: Select the output type. For this work, the DTA-2116 output was used.
   If the Status Log shows a "RunTime Error Dektec" try reducing the Sampling Rate.
   For single-frequency receivers, select one DTA-2116 and configure the following settings.

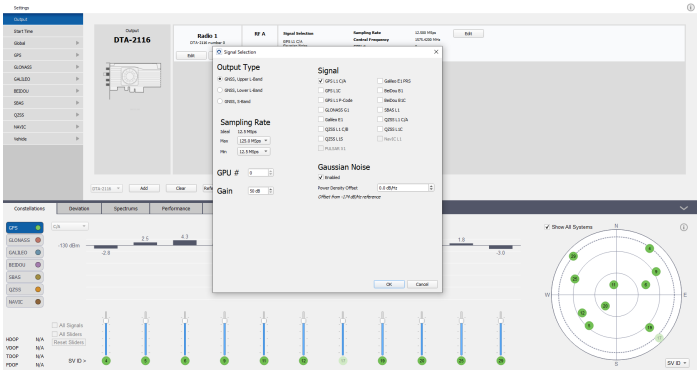

Figure C.1: Skydel Single Frequency Output

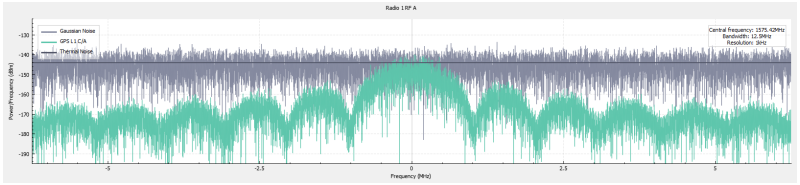

Figure C.2: Skydel Single Frequency Spectrum

For dual-frequency receivers, the same DTA-2116 must be added twice. In this latter case, select both **GNSS Upper and Lower Band**.

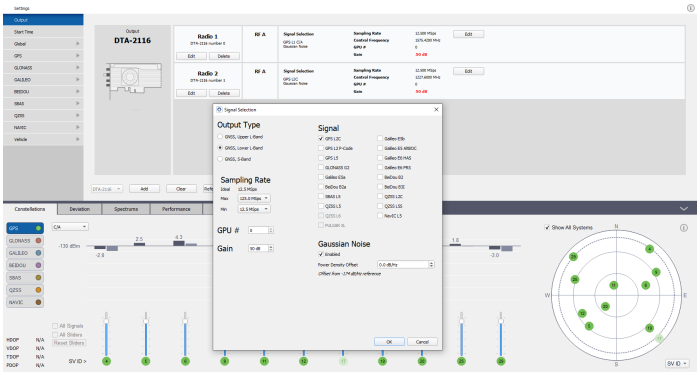

Figure C.3: Skydel Dual Frequency Output

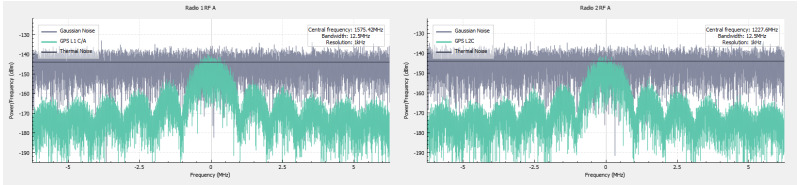

Figure C.4: Skydel Dual Frequency Spectrum

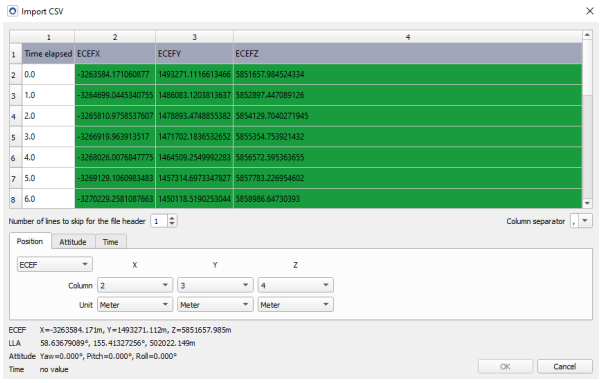

Figure C.5: Import CSV - Position

2. **Settings > Start Time > Custom Time**: Set the start time to match the reference orbit.

3. **Settings > Global > Atmosphere > Tropospheric Model**: Select `None`.

4. **Settings > Global > Atmosphere > Ionospheric Model**: Select `None`.

5. **Settings > Logging**: Enable NMEA, Raw Logging, RINEX Logging, and HIL Input Logging as needed to record data during the simulation.

6. **Settings > Vehicle > Body**: Select *Track Playback* as Trajectory and *Airborne/Spaceborne* as Vehicle Type, then press *Edit*. A new window will appear. Here, import the CSV file of the true orbit previously generated: select *Import CSV with timestamps* and choose the CSV file.
   The settings depend on how the ECEF file was written. To simplify the process, the first line of the file describes the content of the following rows, so this line needs to be skipped by setting *Number of lines to skip for the file header* to 1.
   Next, select the appropriate reference frame (ECEF in this case), specify the X-Y-Z columns and their units C.5.
   Then, import the time. In this work, the elapsed time was used C.6 Then press *Finish*. In this way, the Vehicle is fully configured, and the Skydel environment is ready to run the simulation.

7. Connect the receiver to the computer using the port.

8. Click Arm and then Start: in this way the simulation will start.

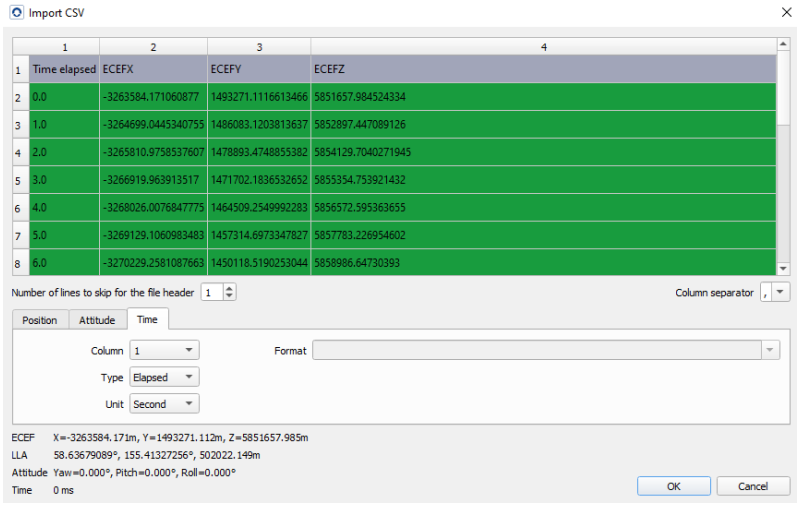

Figure C.6: Import CSV - Time

9. To log data, Skydel can be used as specified in step 5. It is recommended to use either GNSS Viewer (compatible with Skydel and other receivers) or Rx Control (specifically for Septentrio) to better visualize the data logging process.

Figure C.7: Track Playback Visualization on Skydel: the green line correspond to the Simulation Trajectory, the blue line to the Receiver Trajectory

APPENDIX D

Measured Orbit

For Skydel Receivers

The NMEA parsing can be stopped manually after the desired time range if GNSS Viewer is used.
This TXT file then needs to be processed by the `nmea_parsing.py` script. By adjusting the `input_file_path` and `ecef_output_file_name`, the NMEA file will be parsed and automatically saved in the `TXT_Files` folder.
Once `nmea_parsing.py` has run, the measured data are obtained.

For Septentrio Receivers

In Rx Control, after selecting the serial connection, go to Navigation > Receiver Operation > Position > Motion: set *Max* for acceleration and jerk level, and select *Unlimited* for the type of motion.
For logging, both NMEA and SBF data need to be recorded. Once the simulation ends, the SBF data should be converted using the SBF Converter. In "Convert to ASCII", select "Receiver Time, xPPS Offset, PVT Geodetic".
The generated SBF TXT file must then be processed using `sbf_parsing.py`. In this script, adjust the `input_file_name`, `output_path_lla`, and `output_path_ecef` by simply changing the output file names. Once this is set, the resulting TXT files will be saved in the `TXT_Files` folder. After running `sbf_parsing.py`, the measured data are obtained.

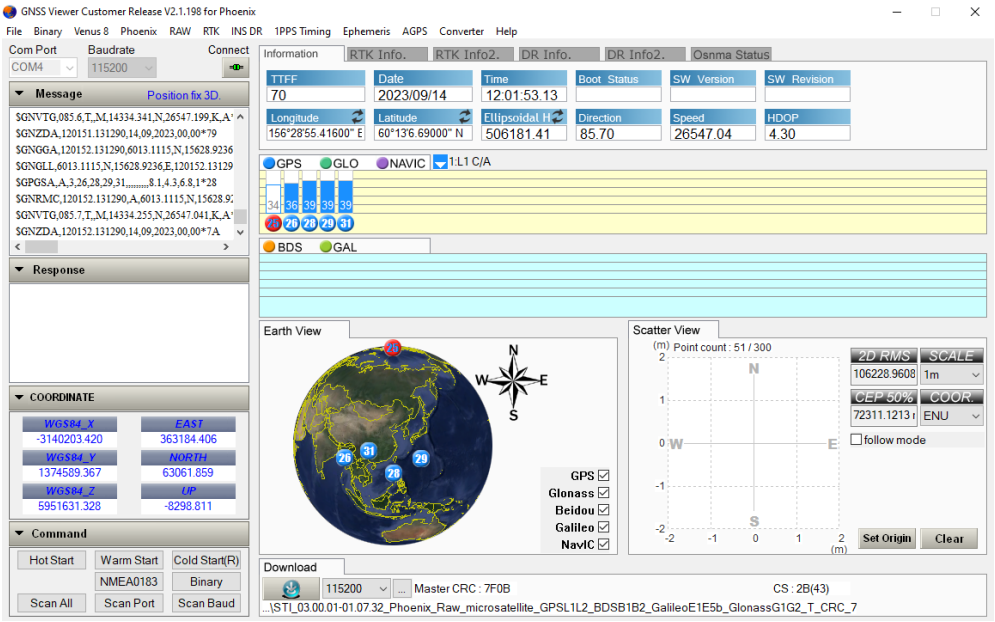

Figure D.1: GNSS Viewer after reaching the lock

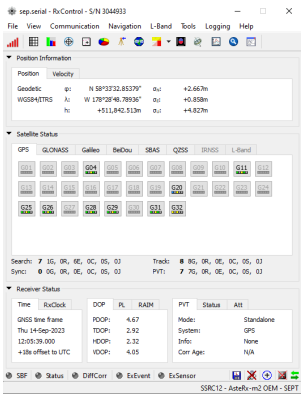

Figure D.2: RxControl Interface after the lock

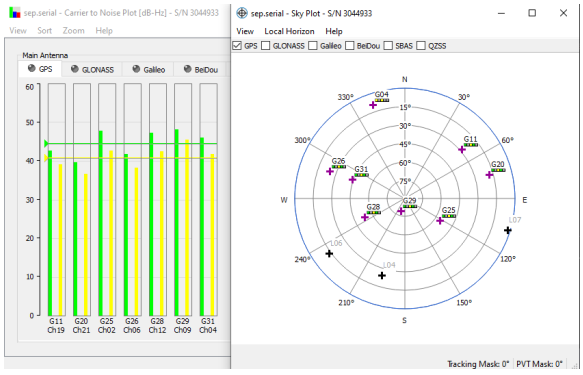

Figure D.3: RxControl: Carrier to Noise Plot and Sky Plot

APPENDIX E

Estimated Orbit

The generation of the Estimated Orbit and the comparison among the True, Measured, and Estimated Orbits is performed in the `Orbit_estimation.py` script.
This script estimates the orbit using the Tudat libraries, taking the True Orbit as initial state and using the Measured Orbit as Observations.
Before running the code, the user must:

1. Select the type of estimation to perform: Perturbed or Unperturbed orbit.
2. Set the initial and final times of the simulation (`t_min` and `t_max`). This means that the first `t_min` seconds will be cut once the receiver lock is reached, and the `t_max` seconds from the beginning will be considered for the estimation process. It is recommended to set `t_min` at least equal to 10 minutes.
3. Select the type of receiver: Septentrio or Skydel. Skydel receiver, indeed, requires offset seconds to be applied: ensure that the offset seconds are adjusted according to the simulated year.
   On the other hand, these offset seconds does not need to be added to Septentrio Measurements.
4. Load the correct input files by changing the name in "...", and also select the proper name for the ouput file.
5. Optional: also the maximum_iterations can be changed.

Once the setup is complete, the script can be executed. The script includes

a set of functions aimed at aligning the True Orbit with the Measured Orbit. This operation is necessary because the Measured Orbit, corresponding to the receiver, may have acquired signal lock only after a few seconds from the start of the simulation. Consequently, the initial data corresponding to this time interval must also be removed from the True Orbit, and the duration of the Measured Orbit may end before that of the True Orbit. Another fundamental aspect concerns the reference frame used for orbit estimation, which is the J2000 frame (ECI reference system). Therefore, the Measured Orbit must be converted into the ECI frame by applying the rotation matrix associated with the True Orbit, appropriately interpolated at the times corresponding to the measurements.
This rotation matrix was previously extracted from the `Tudat_trajectory` software and saved in the corresponding text file.

After completing the alignment between the true orbit and the measured orbit, the script proceeds with the simulation environment setup and the definition of the orbital propagation model. Depending on the set flag, the orbit estimation is performed according to either the perturbed or non-perturbed model. The integrator used is a fixed-step Runge-Kutta of order 7/8 with a step size of one second.
As dependent variables, the script requests the coordinates in ECEF, ECI, LLA and the Keplerian states.
With the propagation system configured, the script simulates the measured observations starting from the measured orbit positions converted into the ECI frame. The estimation algorithm is then executed iteratively, saving at each step the residuals, the estimated parameters, and the orbital state. The residuals at each iteration can be viewed in the terminal output.
Once the orbit estimation is complete, the dependent variables are extracted and the results can be plotted.

APPENDIX F

Propagated Orbit

This script propagates an orbit whose initial state is the final state of the previous estimation (computed in the `Orbit_estimation.py` script and imported accordingly). The user is required to:

1. Select the type of propagation to perform (perturbed or unperturbed orbit).
2. Specify the time interval to propagate forward, starting from the given `simulation_start`.
3. Load the correct input files by updating the `file_path` to the folder containing all `TXT_Files`.

After importing the estimated orbit, the script takes the last Keplerian state and propagates it forward over the specified time interval `delta_t_propagation`. The true orbit is then interpolated again to align its time instances with those of the propagated orbit. Finally, the results are plotted for comparison.

APPENDIX G

TLE Generation Guide

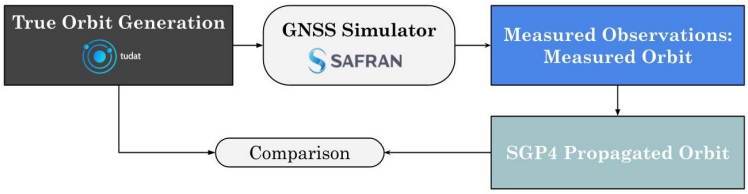

Figure G.1: TLE Generation - Workflow

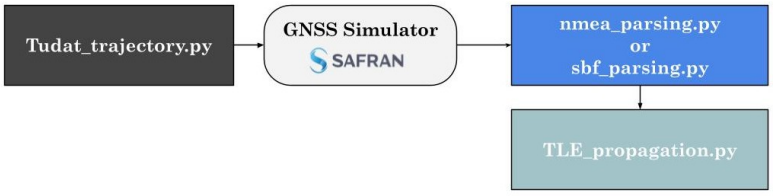

Figure G.2: TLE Generation - Code Workflow

Starting from the GNSS measurements previously processed, the code is able to propagate these observations using the SGP4 propagator.
First, it is necessary to load the measured observations in the ECEF reference frame. The code, through the function `coord_skyfield`, will convert them into the TEME frame.
From these coordinates, it is possible to obtain the TLE parameters by using

the function
`test_tle_fit_normalized_equinoctial`, which is imported from the script `tlefit_equinoctial_eph_fd` [22]. Once the TLE is obtained, the orbit can be propagated using Satrec.twoline2rv(TLE). This results in an orbit propagated via SGP4, which can then be compared with the True orbit, which must be properly loaded into the script. This allows for plotting the differences between the two trajectories.